Probing Multiferroic Orders and Cluster Orbitals by NMR in Lacunar Spinels

Dissertation

Zur Erlangung des akademischen Grades
Dr. rer. nat.

eingereicht an der
Mathematisch-Naturwissenschaftlich-Technischen Fakultät
der Universität Augsburg

von

Markus Prinz-Zwick

Augsburg, Juni 2022

1. Gutachter: Prof. Dr. István Kézsmárki
2. Gutachter: Prof. Dr. Sándor Bordács

Tag der mündlichen Prüfung: 29.9.2022

Contents

Chapter 1

Introduction

Electricity, magnetism and light, once thought to be independent phenomena, were unified by James Clerk Maxwell [1], where he combined previous work by Michael Faraday, André-Marie Ampère and Carl-Friedrich Gauß. The resulting electromagnetism is capable of describing electric phenomena induced by magnetism and vice versa as well as the prediction of electromagnetic waves. It is one of the most important sets of equations in physics and is the foundation of modern technology which is based on the interplay of magnetism with electricity. From using electromagnetic waves for telecommunication, to building up speakers and microphones, our modern technology heavily relies on the principles of electromagnetism. In some conventional material classes, such as ferroelectrics and ferromagnets, electricity and magnetism are seemingly decoupled. Such ferroelectric polar materials show a displacement of charged ions driven by ferroelectric transitions, causing a finite polarization. They therefore have different applications such as piezoelectrics, combining mechanical stress with polarization, ferroelectric capacitors and data storage devices. Similarly, in ferromagnetic materials, electron spins align and create a permanent magnetic moment below the Curie temperature. Countless applications involve magnetism, such as memory devices, electric motors, switches and even medical devices such as magnetoencephalography. In contrast to the former two cases, there is a class of materials where the coupling between electricity and magnetism shows up explicitly. These materials showing cross-coupling between electric as well as magnetic properties are called magnetoelectrics, and a special subgroup of them is called multiferroics. Multiferroics combine two ferroic orders, e.g. ferroelectricity and ferromagnetism. Multiferroics are an active and promising field of research in solid state physics and materials science due to their large potential in IT applications, due to their intertwined electric and magnetic properties. Great advances have been made in studying multiferroics via optical measurements, dielectric spectroscopy, pyroelectric current and magnetization measurements, as well as neutron scattering and atomic force microscopy [2–11]. A simultaneous measurement of polar and magnetic properties is crucial to reveal possible microscopic origins of multiferroicity and to optimize the material design for applications. One of the possible techniques capable of capturing

polar and magnetic properties on the microscopic (atomic) level is Nuclear Magnetic Resonance (NMR). Edward Mills Purcell [12] and Felix Bloch [13] discovered in 1946, that the nuclear magnetic moment can be excited by radiofrequency (rf) photons of a specific frequency, depending on the strength of the external magnetic field, and was awarded with the Nobel Prize in physics in 1952. Since then, NMR developed to be a very important research tool in solid-state physics, solid-state and high-resolution organic chemistry, biology and medicine. For a fixed rf-wave/pulse, the resonance condition is purely determined by the strength of the external magnetic field together with the internal fields in the material. With highly inhomogeneous magnetic fields, produced by a sequence of gradient coils [14], the resonance condition can be spatially restricted to either a two dimensional slice or a point-like sample volume. This concept revolutionized the field of medicine and led to the invention of one of the most powerful diagnostic approaches in 1973 by Paul Christian Lauterbur [15], the magnetic resonance tomography. It enables the creation of a three dimensional image of the NMR-nucleus density in the measured sample.

In solid state physics, however, this imaging method is not applicable due to various reasons. Due to the periodic crystal lattice, a 3D image would not be of great interest, and in order to resolve fine structures such as defects, the method is not sensitive enough as resonances from single nuclei would not be detectable above the noise level. Instead, hyperfine shifts and quadrupolar interactions as well as dynamic processes like the spin-lattice and spin-spin relaxations can be measured by collecting the signal from the whole sample. This approach is used to probe microscopic processes, ferroelectric transitions, magnetic order, domain populations, or dynamic processes changing the relaxation behaviour.

In this work, we expand the limits of solid-state NMR inspired by concepts of magnetic resonance tomography and liquid-phase NMR. These prove-of-concept studies have been carried out on multiferroic lacunar spinels GaV_4S_8 and GaV_4Se_8. Instead of slicing the sample into planes of equal resonance condition, in our case the sampling slices correspond to crystallographic planes with the magnetic field rotated therein, which can be used to map out the anisotropy of the quadrupolar and hyperfine interactions and, in turn, to reconstruct a 3D image of the local electronic distribution over the magnetic V_4S_4 clusters.
This thesis is organized in the following way, to ensure a comprehensive reading.
In Chapter 2, an introduction into the NMR technique is given, followed by a description about the interpretation of characteristic features of NMR spectra, such as line shifts and splittings. Chapter 3 provides an overview about multiferroicity and lacunar spinels, which is a prerequisite for the accessability of our studies on the target compounds GaV_4Se_8 and GaV_4S_8. Experimental details, which are specific to the used measurement setup, are described in Chapter 4. The results of the thesis are described in three chapters, starting with Chapter 5, where the polar properties of lacunar spinels are investigated on the microscopic scale using ^{71}Ga as quadrupolar

probe. Building on this, Chapter 6 describes the determination of multiferroic domain populations in lacunar spinels, further supported by NMR spectroscopy on the ^{51}V nuclei. Finally, Chapter 7 focuses on the charge distribution over V_4S_4 molecular cluster, first investigated via the electric field gradient tensor, and later via the hyperfine-coupling tensor, which reveals detailed information about the spatial spin distribution.

In summary, this thesis aimed at revealing fundamental material properties on the microscopic scale in multiferroic systems, which has been accomplished in the molecular crystal-like magnets GaV_4Se_8 and GaV_4S_8. These results highlight the potential of NMR spectroscopy in revealing the properties of magnetic crystals of complex orders.

Chapter 2

Principles of Magnetic Resonance

2.1 Nuclear Magnetic Resonance

In Nuclear Magnetic Resonance (NMR), the atomic nuclei are being investigated via excitations due to radiofrequency photon absorption. For a nucleus to be NMR active, it needs to possess a non-vanishing magnetic moment, since the interaction with the magnetic field causes the degenerate energy levels of the nucleus to split. Magnetic fields can either originate from an external magnet (NMR) or from the internal fields produced by magnetic materials (zero-field NMR). The magnetic moment of a nucleus is coupled to its angular momentum via the gyromagnetic ratio γ [16]:

$$\vec{\mu}_n = \gamma \vec{I} \tag{2.1}$$

The gyromagnetic ratio is given by:

$$\gamma = \frac{g\mu_\mathrm{N}}{\hbar} \tag{2.2}$$

Here, μ_N is the nuclear magneton $\frac{e\hbar}{2m_\mathrm{P}}$ and g is the g factor of the nucleus. In many NMR experiments, internal and external magnetic fields coexist, which allows an investigation of the local internal fields, since the nucleus is a local probe. For nuclei with spin grater than 1/2, a quadrupolar moment is present, in addition to the magnetic moment. The nuclear quadrupolar moment can couple to an electric field gradient (EFG), if present. This interaction, in analogy to the Zeeman process, splits the previously degenerate nuclear spin transition energies. This shift of the nuclear energy levels is even applicable without the presence of magnetic fields, by exciting these transition with rf photons, which is then called Nuclear Quadrupole Resonance (NQR). This effect can as well coexist with the magnetism of a compound. The study of multiferroic materials, which combines the necessity for a magnetic and electric study, is therefore well suited for a local probe method, capable of precise measurements of the magnetic and polar properties. In the following, the experimental technique will be discussed in more detail, mainly following references [16–18].

2.1.1 Nuclear Spin in a Magnetic Field

In order to describe the resonance phenomenon used in NMR, either a quantum mechanical or a classical approach are providing deeper insights into the matter. Both approaches will be shown shortly in the following.

Quantum Mechanical view

The interaction between the nuclear magnetic moment $\vec{\mu}_n$ and the external magnetic field $\vec{H}$ produces the following simple Hamiltonian, given by

$$\mathcal{H} = -\vec{\mu}_n \cdot \mu_0 \vec{H}. \tag{2.3}$$

Here, μ_0 is the magnetic permeability of the vacuum. With the magnetic field pointing in the z direction, the term simplifies further.

$$\mathcal{H} = -\gamma \hbar J_z \mu_0 H_z \tag{2.4}$$

The energies, or the eigenvalues of H, correspond to the eigenvalues of I_z, given by the magnetic quantum number m ranging between $-I$ and I with $\Delta m = 1$.

$$E = -\gamma \hbar \mu_0 H_z m \tag{2.5}$$

For an example nucleus with spin $I = 5/2$, the energy levels are shown in Fig. 2.1. Radiofrequency photons can overcome the difference between those energy levels and excite the nucleus into a higher energy state, absorbing the photon in the process. The photon energy is given by:

$$E_{\mathrm{ph}} = \hbar \omega_L = \Delta E = \gamma \hbar \mu_0 H_z \tag{2.6}$$

In the resonance condition, the photon frequency ω_L is then given by $\omega_L = \gamma \mu_0 H_z$, which is known as the Larmor frequency, and which is also obtained in the classical approach.

Classical view - Bloch Equations

In 1946, Felix Bloch introduced the equations of motion of the nuclear magnetization, which are often referred to as the Bloch equations [13]. The equations describe the time dependence of the nuclear magnetization, which includes a precession around the static field $\vec{H}$ with the larmor frequency $\omega_{\mathrm{L}} = \gamma \mu_0 H_z$, as well as two different relaxation processes, with their characteristic relaxation times T_1 and T_2. They are

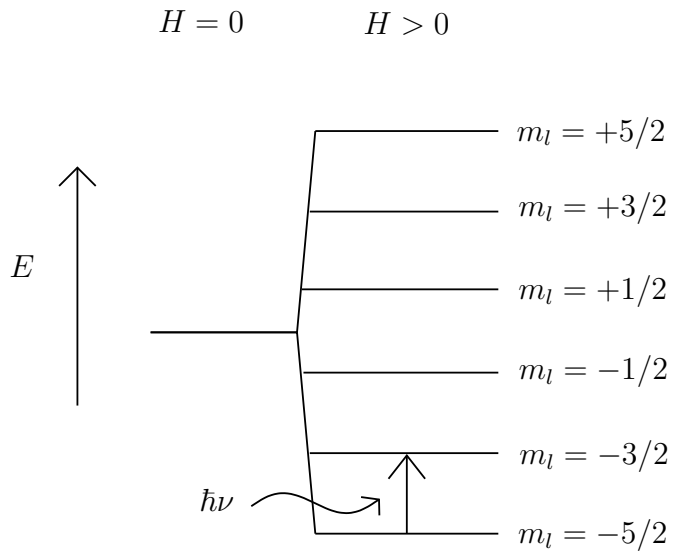

Figure 2.1: Nuclear Zeeman effect for a spin 5/2 nucleus. The energetic degeneracy is lifted by an external magnetic field. The energy levels are equidistant, while radiofrequency photons can excite the nucleus from one state to the next higher state.

given by:

$$\frac{dM_x(t)}{dt} = \gamma(\vec{M} \times \mu_0\vec{H})_x - \frac{M_x(t)}{T_2} \tag{2.7}$$

$$\frac{dM_y(t)}{dt} = \gamma(\vec{M} \times \mu_0\vec{H})_y - \frac{M_y(t)}{T_2} \tag{2.8}$$

$$\frac{dM_z(t)}{dt} = \gamma(\vec{M} \times \mu_0\vec{H})_z - \frac{M_z(t) - M_0}{T_1} \tag{2.9}$$

Since the energy of the system is determined by the z component of the total nuclear magnetization $\vec{M}$, only the T_1 relaxation process transfers energy to the lattice, hence its name spin-lattice relaxation. The processes which cause the nucleus to lose energy to the lattice are either dipole-dipole interactions with electronic magnetic moments, or quadrupolar interactions with the local electric field gradients. The solution to the third Bloch equation (z component), can be found rather straightforward, as the z component of $(\vec{M} \times \mu_0\vec{H})$ is zero, for the field pointing in the z direction, which eliminates the first term responsible for the precession. The resulting simplified differential equation can be solved with an exponential function:

$$M_z(t) = M_z(0)(1 - e^{-t/T_1}) \tag{2.10}$$

The T_2 relaxation, however, conserves energy, as the z component is unaffected by the relaxation process. The T_2 process is driven by the interaction between fluctuating nuclear spins, which produce an irreversible dephasing of the the in-plane

nuclear magnetization $\vec{M}_{\mathrm{xy}}$. When entering the rotating frame of reference, the first term, corresponding to the precession of the nuclear magnetization, vanishes, which simplifies the differential equation. The solution is given by an exponential decay of the in-plane nuclear magnetization:

$$M_{\mathrm{xy}}(t) = M_{\mathrm{xy}}(0)e^{-t/T_2} \tag{2.11}$$

The dynamics of the nuclear magnetization can be introduced via alternating magnetic fields (rf field) in addition to the static field. When neglecting the T_1 and T_2 relaxations, due to the short exposure time τ of the rf field($\tau << T_2, T_1$), the Bloch equations in the rotating frame then become [18]:

$$\frac{dM_x}{dt} = -\Delta\omega M_y \tag{2.12}$$

$$\frac{dM_y}{dt} = -\Delta\omega M_x - \gamma\mu_0 H_x M_z \tag{2.13}$$

$$\frac{dM_z}{dt} = \gamma M_y \mu_0 H_x \tag{2.14}$$

Here, $\Delta\omega = \omega - \omega_L$ is the frequency difference between the rf frequency and the larmor frequency. The time dependence of the z component of the nuclear magnetization is then given by [18]:

$$M_z(t) = M_{z,0}\frac{(\gamma\mu_0 H_x)^2 \cos\omega_{eff}t + \Delta\omega^2}{\omega_{eff}^2} \tag{2.15}$$

Where $\omega_{eff} = \gamma\mu_0 H_{eff} = \gamma\sqrt{\mu_0^2 H_x^2 + \Delta\omega^2/\gamma^2}$. If the frequency of the rf pulse is equal to the Larmor frequency, hence $\Delta\omega = 0$, the magnetization vector rotates into the x-y plane after a time of $t = \pi/(2\mu_0\gamma H_x)$.

2.1.2 Pulse Sequences

The classical picture involving the Bloch equations allow for a vivid picture of the measurement process in NMR spectroscopy. The z component of the nuclear magnetization can be measured by utilizing the fact that applying an oscillating magnetic field with $\omega = \omega_{\mathrm{L}}$ can tilt the nuclear magnetization vector. The total energy needed to tilt the magnetization by an angle α is given by:

$$\Delta E(\alpha) = \mu_0 H(\mu_{\mathrm{N},0} - \mu_{N,\alpha}) = \tau P_{\mathrm{pulse}} \tag{2.16}$$

Where P_{pulse} is the power of the rf pulse and τ is the exposure time. For $\alpha = 90°$, the nuclear magnetization is completely within the x-y plane and starts precessing around the static field. The nuclear x-y magnetization therefore starts decreasing due

to two independent processes. Due to T_2 relaxation, the x-y magnetization decreases exponentially as shown in Eq. 2.11, caused by the interaction between the fluctuating magnetic dipole moments of other nuclei. Additionally, inhomogeneities within the static field slightly alter the precession speeds of the individual nuclei in the sample, causing them to dephase over time. The decline in x-y magnetization is then given by:

$$M = M_0 e^{-t/T_2^*} \tag{2.17}$$

The exponential decay in the x-y magnetization is called the free induction decay (FID), and it is depending on the characteristic time T_2^*, which describes both decay processes. Therefore, $T_2^* < T_2$ for any finite inhomogeneity of the static field. The decay of the x-y magnetization caused by inhomogeneities, however, can be reversed via application of a 180° pulse. Due to $d\vec{M}/dt = \vec{M} \times \vec{B}_0$, an inversion of $\vec{M}$ also inverts the precession direction, which causes the spins to refocus after a 180° pulse. Any effects caused by inhomogeneities are therefore removed. The resulting refocused nuclear spins create a peak in the magnetization which is picked up as a spin echo, first detected by Erwin Hahn [19]. For a detailed depiction of the spin echo method, see Fig. 2.2. The intensity of the echo, based on the time τ between the pulses is given by:

$$I(2\tau_p) = I_0 e^{-2\tau/T_2} \tag{2.18}$$

The factor of 2 originates from the time τ having to pass twice for the spins to refocus. This formula allows a direct measurement of the T_2 relaxation time, when measuring subsequent spin-echos with different τ values. In more complex materials, many nuclei experiencing different T_2 relaxations might have overlapping spectra, causing the measured curve to be multiexponential.

The T_1 relaxation, discussed in the previous subsection, is measured via a different pulse sequence. In order to observe the T_1 relaxation process, the nuclear magnetization needs to be either tilted with respect to the static field, or destroyed entirely. Afterwards, the recovery of the z-component of the nuclear magnetization can be observed via the spin echo method. The tilting or destruction of the nuclear magnetization is realized by one or a sequence of pulses, respectively. Via the inversion recovery method, a 180° pulse is applied prior to the spin-echo sequence separated by the time τ_{sl}. The nuclear magnetization then relaxes back from $-\vec{M}$ to $\vec{M}$ and via subtraction of the two echo intensities, T_1 can be extracted via the following formula:

$$I(\tau) = 2I_0 e^{-\tau_{\mathrm{sl}}/T_1} \tag{2.19}$$

The factor of 2 results from the difference between the echo intensities corresponding to the $-\vec{M}$ and $\vec{M}$ directions, which have opposite signs due to the phase difference of 180°. This method is useful when the intensity of the NMR line is a limiting factor, and if the whole line can be excited with one pulse. For broad lines, this method is less efficient. Additionally, after one pulse sequence and before the next,

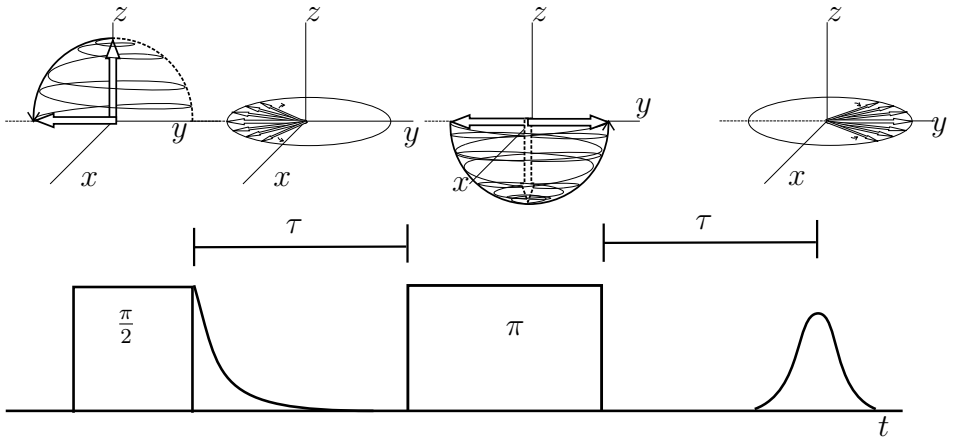

Figure 2.2: Display of a $\pi/2 - \pi$ spin-echo sequence:
During the duration of the $\pi/2$ pulse, the nuclear magnetization is being tilted by 90° from the z-direction into the x-y-plane, on a downward spiral. After the 90° pulse the precession of the nuclear spins around the external magnetic field causes the magnetization to dephase, due to small field inhomogeneities and the irreversible T_2 relaxation. This is the free induction decay (FID). After a time τ, a π-pulse is being applied, which tilts every nuclear spin by 180° on a spiral curve to -z direction and then back on the x-y-plane. The spins then refocus and produce a spin echo.

it is necessary to wait until all spins are relaxed back to the original position, which can increase the measurement time for slowly relaxing nuclear magnetization, for instance in spin liquids [20, 21].
Via the saturation recovery method, a series of pulses with random length are applied to the sample. The subsequent random tilting results in the nuclear spins to be oriented randomly after a sufficient amount of pulses. The magnetization then relaxes back to the original position, and during the process, the z-magnetization is measured via the spin echo sequence. The fitting formula is the following:

$$I(\tau) = I_0(1 - e^{-\tau/T_1}) \tag{2.20}$$

This process does not require the lines to be sharp, nor the T_1 process to be fast, but the sequence of pulses can introduce additional heat to the sample if the rf power is high, which can alter the temperature of the sample.

2.2 Hyperfine coupling

In addition to the already external applied magnetic field of the experimental setup, the interaction between the nuclei and electrons can cause local magnetic fields at

the nuclear site as well. A prominent example for this would be the chemical shift σ, which introduces an additional field ΔH component due to the chemical environment of the nucleus [16].

$$\Delta H = -\sigma H_0 \tag{2.21}$$

The induced magnetic field opposes the applied field due to the diamagnetic shielding, which causes the effect. Usually, the chemical shift is in the range of ppm, which is rather small compared to lineshifts in ferromagnets. The fields caused by the dipole fields of unpaired electrons, their orbital momentum or their contact interaction are called hyperfine fields. The hyperfine fields in ferromagnets, antiferromagnets or in more complex magnetic structures such as spin cycloids or skyrmion lattices, vastly outcompete the chemical shift. As one of the most important NMR parameters, hyperfine fields will be discussed in the next subsection, following reference [16].

2.2.1 Hyperfine Coupling and Internal Fields

The interactions between nuclei and electrons are crucial for the NMR measurement technique. Any magnetic fields induced due to the motion of the electron, its spin magnetic moment or its probability distribution can shift the NMR lines either to smaller or higher fields. When calculating the internal field at the position of a nucleus, each of the possibly competing contributions needs to be calculated separately and then summed up. In the following, each contribution will be discussed separately in order to arrive at the description of the hyperfine fields in magnetic materials [16].

Hyperfine field due to orbital momentum of electrons

From classical electromagnetism, the magnetic field at the position $\vec{r}$, produced by a current I flowing through an infinitesimal lenght $d\vec{l}$ at the position $\vec{r'}$ is given by the Biot-Savart law [22]:

$$\mu_0 d\vec{H}(\vec{r}) = \frac{\mu_0}{4\pi} I d\vec{l} \times \frac{\vec{r} - \vec{r'}}{|\vec{r} - \vec{r'}|^3} \tag{2.22}$$

With the current $I = \frac{dq}{dt}$, the differential changes to $Id\vec{l} = dq\frac{d\vec{l}}{dt} = \vec{v}dq$. Integration on both sides of the equation then leads to the magnetic field produced by a moving point charge:

$$\mu_0 \int d\vec{H}(\vec{r}) = \frac{\mu_0}{4\pi} \vec{v} \times \frac{\vec{r} - \vec{r'}}{|\vec{r} - \vec{r'}|^3} \int dq \tag{2.23}$$

$$\mu_0 \vec{H}(\vec{r}) = \frac{q}{4\pi} \vec{v} \times \frac{\vec{r} - \vec{r'}}{|\vec{r} - \vec{r'}|^3} \tag{2.24}$$

By extending the fraction with the mass of an electron, the angular momentum $\vec{L} = \vec{r} \times m\vec{v}$ can be introduced into the equation:

$$\mu_0 \int d\vec{H}(\vec{r}) = -\frac{q}{4\pi m} \frac{\vec{L}}{|\vec{r} - \vec{r'}|^3} \tag{2.25}$$

When transitioning from the classical to the quantum mechanical picture and placing the electron into an atomic orbit, the angular momentum $\vec{L}$ becomes the orbital momentum $\vec{L} = \hbar\vec{l}$. The length of $\vec{l}$ is its orbital quantum number $\mathbf{l}$. The resulting field then simplifies to:

$$\mu_0 \vec{H}(\vec{r}) = -\frac{1}{4\pi} 2\mu_\mathrm{B} \frac{\mathbf{l}}{|\vec{r} - \vec{r'}|^3} \tag{2.26}$$

With the orbiting electron having a distance of r_0 to the nucleus occupying the origin, the formula simplifies further.

$$\mu_0 \vec{H}(\vec{r}) = -\frac{1}{4\pi} 2\mu_\mathrm{B} \frac{\mathbf{l}}{r_0^3} \tag{2.27}$$

As depicted in Fig. 2.3, the magnetic field of the orbital and the dipole field of the electron coexist, and therefore have to be summed up. The dipole term of the hyperfine coupling is shown in the following.

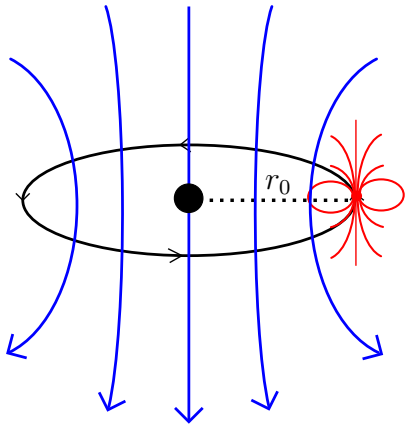

Figure 2.3: Depiction of the internal field contributions of the spin of an electron and its orbit. The dipole field is determined by the orientation of the electron, and its position, while the orbital contribution is determined by the magnetic moment of the orbit produced by the electron motion.

Dipole contribution of the electron spin

The magnetic dipole field at the position $\vec{r}$, produced by a pointlike magnetic moment

$\vec{\mu}$ at the position $\vec{r'}$, is given by:

$$\mu_0 \vec{H}(\vec{r}) = \frac{\mu_0}{4\pi}\left(-\frac{\vec{\mu}}{r^3} + 3\frac{(\vec{r}-\vec{r'})(\vec{\mu}\cdot(\vec{r}-\vec{r'}))}{r^5}\right) \tag{2.28}$$

For an electron, the magnetic moment is given by $\vec{\mu} = -2\mu_B \vec{s}$, where the spin of the electron $\vec{s}$ is $\frac{1}{2}$. The resulting field then becomes:

$$\mu_0 \vec{H}(\vec{r}) = \frac{-2\mu_B\mu_0}{4\pi}\left(-\frac{\vec{s}}{r^3} + \frac{3(\vec{r}-\vec{r'})(\vec{s}\cdot(\vec{r}-\vec{r'}))}{r^5}\right) \tag{2.29}$$

With the electron-nucleus interaction being treated as a simple interaction between two dipoles, the Hamiltonian therefore equals that of a pair of magnetic dipoles [16]

$$\mathcal{H} = \frac{\vec{\mu_e}\cdot\vec{\mu_n}}{r^3} - \frac{3(\vec{\mu_e}\cdot\vec{r})(\vec{\mu_n}\cdot\vec{r})}{r^5} \tag{2.30}$$

When considering orbitals with nonzero orbital momentum, the distance r between the nucleus and the electron is finite. For s orbitals however, this expression diverges, which necessitates a different approach for internal fields produced by s orbitals.

Spin polarization of core electrons and the contact field

In order to approach the calculation of the internal fields of a spherical electronic distribution, we approximate the nucleus as a charge q on a circular path, producing its own magnetic field. The z component of this field is H_z. Following reference [16], we weight this field with the electronic distribution and express $\bar{H}_z$, which can be considered the field difference induced by the electron distribution:

$$\bar{H}_z = \int dV H_z(\vec{r})|u(r)|^2 \tag{2.31}$$

When splitting the spherical integral into two terms, the volumes inside and outside a sphere with radius r_0, the integral over the outer part vanishes. Therefore, the field value $H_z(0) = H_c$ and the electron density $|u(0)|^2$ at the center of the nucleus determine $\bar{H}_z$ when approaching $r_0 \to 0$:

$$\bar{H}_z = H_c|u(0)|^2\frac{4\pi}{3}r_0^3 \tag{2.32}$$

The field H_c at the center of the nucleus can be described via the flowing current $\frac{q}{T}$, where T is the period of the circular motion of the nucleus.

$$\vec{H_c} = \frac{q}{4\pi T}\frac{\vec{r_0}\times\vec{v}}{r_0^3} = \frac{q}{4\pi T}\frac{v}{r_0^2}\vec{k} \tag{2.33}$$

Where $\vec{k}$ is the unitary direction vector of the magnetic field H_c given by $\vec{k} = \frac{r_0^2}{v}\frac{\vec{r_0}\times\vec{v}}{r_0^3}$. Similarly, the magnetic moment is given by the product of the area of the loop and the current:

$$\vec{\mu_n} = \frac{q}{T}\pi r_0^2\vec{k} = \frac{qr_0v}{2}\vec{k} \tag{2.34}$$

Therefore, H_c can be written in terms of magnetic moment:

$$\vec{H_c} = \frac{2\vec{\mu_n}}{4\pi r_0^3} \tag{2.35}$$

Eq. 2.32 then transforms into the following after introducing the field direction $\vec{k}$:

$$\vec{k}\bar{H_z} = \frac{8\pi}{12\pi}\mu_n|u(0)|^2 \tag{2.36}$$

Coupling with the electron magnetic moment μ_e yields the interaction energy of the nucleus:

$$E = -\frac{8\pi}{12\pi}\vec{\mu_e}\cdot\vec{\mu_n}|u(0)|^2 \tag{2.37}$$

The Hamiltonian corresponding to this interaction is then given by:

$$H = -\frac{8\pi}{12\pi}\vec{\mu_e}\cdot\vec{\mu_n}\delta(r) \tag{2.38}$$

Where $\delta(r)$ is the Dirac delta function, and the electron magnetization is given by $\mu_e = -2\mu_B\vec{s}$. The energy of the interaction can be interpreted as the magnetic moment of the nucleus interacting with a magnetic field produced by the spherical electronic distribution. The resulting field is then given by:

$$\mu_0\vec{H} = -2\mu_B\frac{8\pi}{12\pi}\vec{s}|u(0)|^2 \tag{2.39}$$

This is the Fermi contact field, and it vanishes for fully occupied unpolarized s orbitals, since $|u(0)|^2$ is identical for spin up and down electrons. Provided with a mechanism for an outer shell orbital to polarize the inner shells, this term can provide an isotropic hyperfine shift. In a vivid example, an unpaired spin up electron in a p shell would have a nonzero overlap with the s orbital. Due to the Pauli exclusion principle, the up electron in the s orbital cannot overlap with the up electron of the p orbital. The down electron in the s orbital, however is unperturbed. Since the probabilities for both up and down electrons to be in the s orbital are each equal to 1, the probability of the up electron must be higher in the non overlapping regions of the s orbital, including the location of the nucleus. This results in a overdensity of the up electron at $r = 0$, which gives rise to a nonzero contact term. See Fig. 2.4 for a visual representation of the proposed mechanism. For different orbitals, this interaction can be positive or negative, meaning that the polarized s electrons

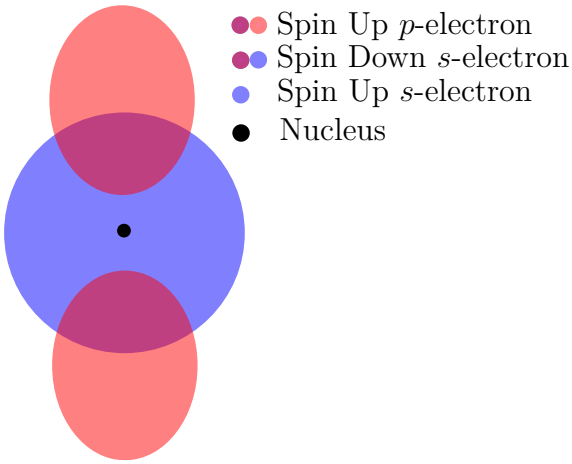

Figure 2.4: Depiction of the core polarization effect. The overlapping regions between the p and s orbital restrict the occupation of electrons with identical spin. Therefore, the s-electron with the same spin as the p electron (here: Up) has a higher probability density at the nucleus.

can either point parallel or antiparallel to the unpaired electron. In $3d$ orbitals, for example, the s orbital polarizes negatively.

The total hyperfine field can therefore be described as the sum of the aforementioned contributions:

$$\mu_0 \vec{H} = \frac{-2\mu_0\mu_\mathrm{B}}{4\pi}\left(\frac{\vec{l}}{r_0^3} - \frac{\vec{s}}{r^3} + \frac{3\vec{r}(\vec{s}\cdot\vec{r})}{r^5} + \frac{8\pi}{3}\vec{s}|u(0)|^2\right) \tag{2.40}$$

2.2.2 Characteristic Lineshifts and Representation of the Hyperfine Tensor

The hyperfine coupling and the complex NMR lineshapes that arise from it can be used to conclude the unterlying magnetic structure. In order to illustrate this in the following, examplary lineshifts are investigated for two nuclei, either being magnetic or non-magnetic. When investigating the magnetic nucleus, e.g. the nucleus of the magnetic ion, the on-site fields are dominant, which originate from the unpaired electron and its orbital, dipole and contact contribution. Non-magnetic nuclei in the same compound, however, interact via transferred fields (dipole fields) originating from the magnetic ion. The observed lineshapes and lineshifts can be very different for the different nuclei, hence a solid understanding of the nuclei and their coordinates

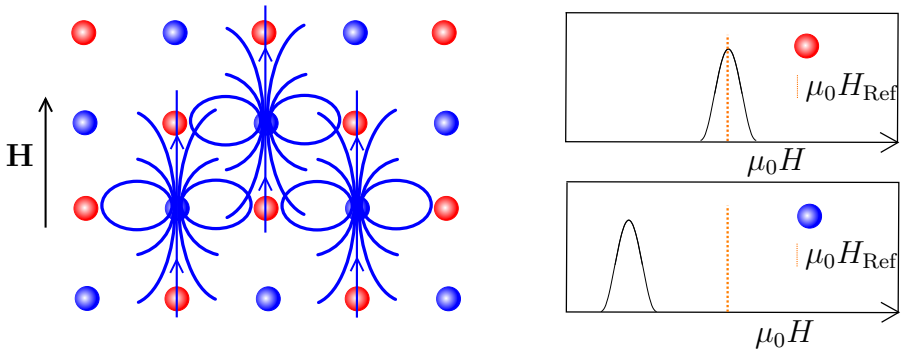

Figure 2.5: Ferromagnetic ordering in a simple cubic lattice with two atoms. The hyperfine fields for the non magnetic sites (red bullets) cancel out while the magnetic sites (blue bullets) show a strong hyperfine shift.

is important. In order to show how the lineshape and lineshift can be used to better understand the magnetic structure, a few examples are shown in the following.

Characteristic NMR lines in ferromagnets

In ferromagnets, the electron spins align, creating a bulk magnetization, which linearly corresponds with the lineshift. The on-site fields in some ferromagnets can be very high, reaching up to 19 T in Cr based spinels such as $CdCr_2S_4$ or $HgCr_2S_4$ [23]. Depending on the crystal structure, however, the transferred fields can be rather small or even cancel out. In Fig. 2.5, a simple cubic lattice with two atoms is shown as an example, where the ferromagnetic order would produce a cancellation of the transferred fields on the non magnetic sites. When calculating the transferred fields, the dipole fields from the magnetic ions in the first octahedral shell are summed up:

$$\begin{aligned}\vec{H}_{\mathrm{NM}} &= -\frac{2\mu_0\mu_{\mathrm{B}}}{4\pi}\sum_i^8 -\frac{\vec{s}}{r_i^3} + \frac{3\vec{r_i}(\vec{s}\cdot\vec{r_i})}{r_i^5} \\ &= -\frac{2\mu_0\mu_{\mathrm{B}}}{4\pi}\left(\sum_{\mathrm{Top,Bottom}}^2 \frac{2\vec{s}}{r_i^3} - \sum_{\mathrm{Rest}}^4 \frac{\vec{s}}{r^3}\right) \\ &= -\frac{2\mu_0\mu_{\mathrm{B}}}{4\pi}\left(4\frac{\vec{s}}{r^3} - 4\frac{\vec{s}}{r^3}\right) = 0 \end{aligned} \tag{2.41}$$

The magnetic sites, however would show canceled out internal fields, since the dipole fields of the neighbouring atoms usually are not strong enough to overcome the on-site fields(irrespective of the crystal structure). Therefore a strong hyperfine shift is observed. Depending on the orbitals occupied, this shift can be either positive (internal and external field are parallel) or negative (internal and external field are antiparallel), although only a positive shift is shown in Fig. 2.5, exemplary.

Characteristic NMR lines in antiferromagnets

In an antiferromagnet, the bulk magnetization, as well as the susceptibility vanishes, due to the opposing spin directions and their cancellation on larger scales. Locally, however there are internal fields present, which can be detected by NMR [24]. In Fig. 2.6, a simple cubic lattice with antiferromagnetic order is shown, together with the expected lineshapes and shifts. Again, the non magnetic sites do not experience a shift due to the cubic structure cancelling the dipole fields of the neighbouring sites. For the magnetic sites, however, two inequivalent positions are established, as the external field is either parallel or antiparallel with the internal fields of the different magnetic sites. An opposite spin direction reverses the dipole and contact

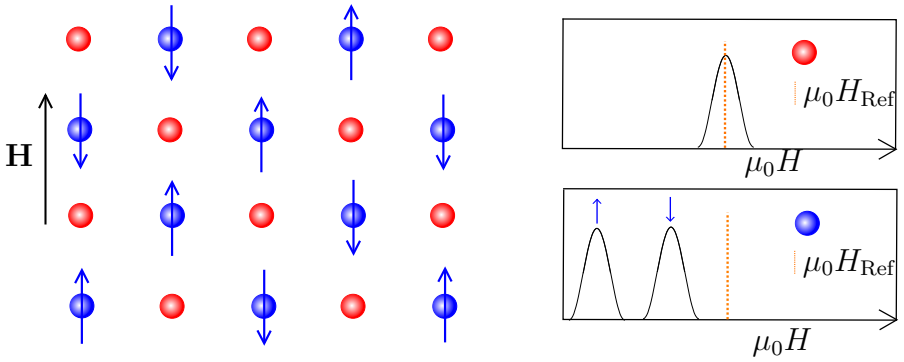

Figure 2.6: Antiferromagnetic ordering in a simple cubic lattice with two atoms. The hyperfine fields for the non magnetic sites cancel out while the magnetic sites show a strong hyperfine shift, splitting symmetrically due to the opposing spin directions.

fields, but keeps the orbital field unchanged, which is the reason for the two lines of the magnetic site not being symmetrically split around the diamagnetic reference position. In spin only systems, this may not necessarily be the case. Also, in more complex crystal structures the transferred fields may not cancel out [25].

Characteristic NMR lines in spin cycloid/helix systems

In the simple ferro- or antiferromagnets shown above, the lineshapes are simple sharp gaussians, as the parallel or antiparallel spins produce one fixed internal field value for all nuclei of the same type. In more complex magnets without inversion centers, the Dzyaloshinskii-Moriya interaction competes with the ferromagnetic exchange, and produces spin cycloids or helices along a certain propagation vector $\vec{q}$ in the process. A simple example of a one dimensional spin cycloid and the resulting NMR lines are shown in Fig. 2.7. The spins follow a sinusoidal curve, as we follow the propagation vector $\vec{q}$. Near the extrema of the sinewave (derivative vanishes) the spin directions of neighbouring spins are similar, only changing very slowly, whereas

the differences between neighbouring spin directions increase near the perpendicular positions (derivative maximal). This alters the lineshape in a way, that the intensity near the extremal internal fields (close to spin up or down, leftmost and rightmost part of the NMR line) is higher than for the spin direction perpendicular to the external field (middle of the line). The distribution of the internal fields originates from the dipole fields of the spin cycloid/helix, hence is independent of the orbital component. Lineshifts due to orbital fields are therefore still present for the magnetic nuclei, while the non-magnetic nuclei can still be shifted via isotropic transferred fields. The lineshape in this simplified model can be roughly estimated using the arguments above, but in more complex materials, the process of line fitting and the determination of the spin structure can be very challenging [26, 27].

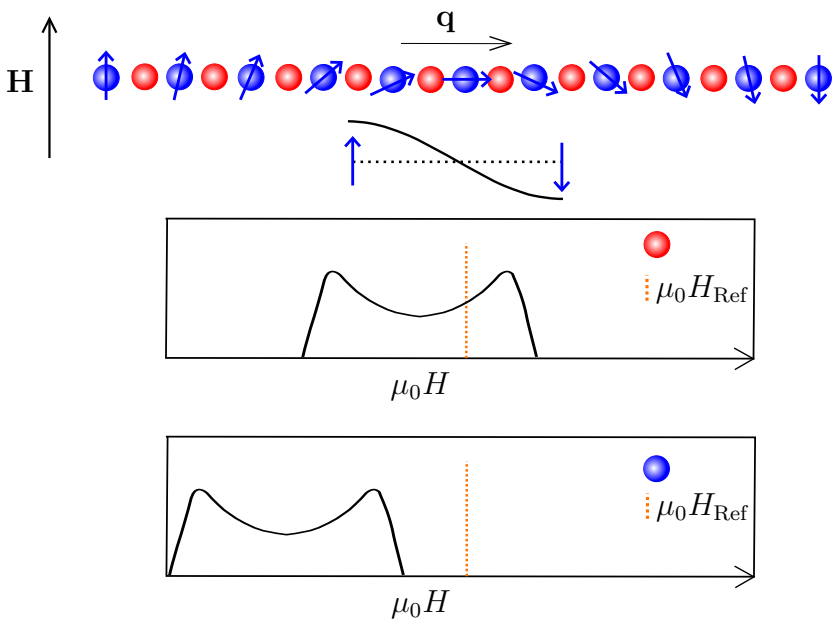

Figure 2.7: Simplistic 1D spin cycloid, and the estimated NMR lineshape. The intensities near the extremal internal fields are higher, due to the sinusoidal distribution of spins.

Matrix Representation of the hyperfine field

The hyperfine coupling Hamiltonian, capturing the interaction between the nuclear spin (**I**)and the electron spin (**s**), is given by:

$$\mathcal{H} = \mathbf{I} \cdot \mathcal{A}_{\mathrm{Hf}} \cdot \mathbf{s} \tag{2.42}$$

Where $\mathcal{A}_{\mathrm{Hf}}$ is the 3×3 hyperfine interaction matrix. Equivalently, the hyperfine field is given by the product $\mathcal{A}_{\mathrm{Hf}} \cdot \mathbf{s}$, and can be written as a product of the direction of

the electron spin with a tensor describing the resulting internal fields.

$$\mathcal{A}_{\mathrm{Hf}} \cdot \mathbf{s} = \begin{pmatrix} H_{\perp,1} & 0 & 0 \\ 0 & H_{\perp,2} & 0 \\ 0 & 0 & H_{\parallel} \end{pmatrix} \mathbf{s} \tag{2.43}$$

Here, the hyperfine tensor is in its eigenbase, but in general, it is a symmetric matrix with 6 independent matrix elements, which need to be evaluated individually, either via theoretical approaches [28–30], or via measurement [31]. Symmetry operations that apply to the local site symmetry of the investigated nucleus have to be obeyed by the hyperfine tensor as well, which can be used to reduce the number of independent parameters. The hyperfine coupling is a main contribution to the characteristics of NMR lines and allows conclusions about the magnetic properties of the investigated material.

2.2.3 Electron Orbitals in a Crystal Field

The electron distribution is crucial for NMR experiments, as the hyperfine fields are determined by the electron- nucleus interaction. In ions of transition metals, such as Fe^{2+} or V^{4+}, one electron in the d shell is responsible for its magnetic moment, and can be described by the solution to the Schrödinger equation of the hydrogen atom, under consideration of the effective nuclear charge Z of the transition metal. The solutions to the Schrödinger equation are given by the following wavefunctions described by the spherical harmonics, distinguishable by their different magnetic quantum numbers $-2 \leq m_l \leq 2$ [32]:

$$\Psi_{m_l=0}(r,\theta) = \frac{1}{81\sqrt{6\pi}} \left(\frac{Z}{a_0}\right)^{3/2} \frac{Z^2(r-r_0)^2}{a_0^2} e^{-\frac{Z(r-r_0)}{3a_0}} (3\cos^2\theta - 1) \tag{2.44}$$

$$\Psi_{m_l=-1}(r,\theta,\phi) = \frac{1}{81\sqrt{\pi}} \left(\frac{Z}{a_0}\right)^{3/2} \frac{Z^2(r-r_0)^2}{a_0^2} e^{-\frac{Z(r-r_0)}{3a_0}} \sin\theta\cos\theta e^{-i\phi} \tag{2.45}$$

$$\Psi_{m_l=+1}(r,\theta,\phi) = \frac{1}{81\sqrt{\pi}} \left(\frac{Z}{a_0}\right)^{3/2} \frac{Z^2(r-r_0)^2}{a_0^2} e^{-\frac{Z(r-r_0)}{3a_0}} \sin\theta\cos\theta e^{i\phi} \tag{2.46}$$

$$\Psi_{m_l=-2}(r,\theta,\phi) = \frac{1}{162\sqrt{\pi}} \left(\frac{Z}{a_0}\right)^{3/2} \frac{Z^2(r-r_0)^2}{a_0^2} e^{-\frac{Z(r-r_0)}{3a_0}} \sin^2\theta e^{-2i\phi} \tag{2.47}$$

$$\Psi_{m_l=+2}(r,\theta,\phi) = \frac{1}{162\sqrt{\pi}} \left(\frac{Z}{a_0}\right)^{3/2} \frac{Z^2(r-r_0)^2}{a_0^2} e^{-\frac{Z(r-r_0)}{3a_0}} \sin^2\theta e^{2i\phi} \tag{2.48}$$

The probability distribution $|\Psi|^2$ of the electron is phase independent, hence the charge distribution produced by two wavefunctions with same magnitude magnetic

quantum numbers will be identical, and therefore degenerate. Since the wavefunctions above are solutions to the Schrödinger equation, linear combinations are solutions as well. By eliminating the phase factor via linear combination, one obtains the real harmonics, which are used to describe the atomic orbitals in an octahedral crystal field [33, 34]:

$$\Psi_{z^2} = \Psi_{m_l=0} \tag{2.49}$$

$$\Psi_{yz} = \frac{i}{\sqrt{2}}\left(\Psi_{m_l=-1} - \Psi_{m_l=+1}\right) \tag{2.50}$$

$$\Psi_{xz} = \frac{1}{\sqrt{2}}\left(\Psi_{m_l=-1} + \Psi_{m_l=+1}\right) \tag{2.51}$$

$$\Psi_{xy} = \frac{i}{\sqrt{2}}\left(\Psi_{m_l=-2} - \Psi_{m_l=+2}\right) \tag{2.52}$$

$$\Psi_{x^2-y^2} = \frac{1}{\sqrt{2}}\left(\Psi_{m_l=-2} + \Psi_{m_l=+2}\right) \tag{2.53}$$

The shapes of these real harmonics are the well known five atomic d orbitals, shown schematically in Fig. 2.8. In this figure, an octahedral crystal field was assumed, which lifts the degeneracy of the orbitals and splits them into the T_{2g} and e_g levels, due to the electric repulsion between the orbital lobes and the octahedral ligands positioned on the cartesian axes. An electron in a $3d^1$ transition metal ion in an octahedral crystal field would be occupying one of these orbitals. In order to understand the magnetism of such a configuration, which will be relevant for the hyperfine coupling, the expectation value of the z component of the orbital momentum $\langle L_z \rangle$ is calculated according to [33]. The z-component of the orbital momentum operator is given by:

$$L_z = \frac{\hbar}{i}\frac{\delta}{\delta\phi} \tag{2.54}$$

Using the d wavefunctions above, the expectation value $\langle L_z \rangle$ can be calculated straightforwardly:

$$\langle L_z \rangle = \int_0^{2\pi} \Psi_{yz} L_z \Psi_{yz} d\phi \propto \int_0^{2\pi} \sin\phi \frac{\hbar}{i}\frac{\delta}{\delta\phi}\sin\phi d\phi = -\frac{\hbar}{2i}\left[\cos^2\phi\right]_0^{2\pi} = 0 \tag{2.55}$$

This can be repeated analogously for the other orbitals. This phenomenon is called "quenching of orbital momentum", and it describes the vanishing of the orbital moment under the influence of crystal fields. A classical picture would describe it as the orbitals having a finite magnitude of the orbital momentum given by $\sqrt{2(2+1)}\hbar$, but the orbital moment is constantly changing direction due to the influence of the electric field gradient (EFG) of the crystal field. The average therefore vanishes, since all directions are reached equally often. This effect, however, can be partially negated by the spin orbit coupling, and recover orbital momentum [33].

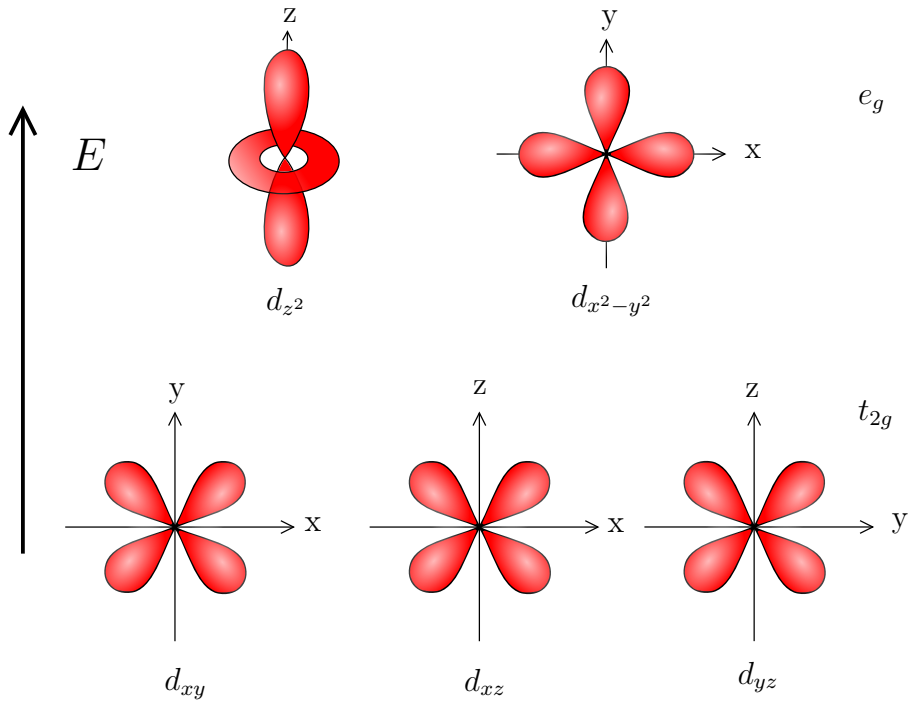

Figure 2.8: Schematic depiction of the three t_{2g} and two e_g orbitals, split by an octahedral crystal field. The lower t_{2g} orbitals form a degenerate triplett, and the higher energy e_g orbitals form a degenerate doublet.

2.3 Quadrupolar Interaction

Nuclei with a spin larger than 1/2 have a non-vanishing electric quadrupolar moment, and can therefore interact with an electric field gradient (EFG). This EFG is provided via the crystal field, and can change or even emerge when structural transitions occur, opening the possibility to observe phase transitions, charge order, so called "charge density waves" (CDW) in high T_c superconductors and emergent polarizations as well as identifying the position of the investigated nucleus in a set of possible sites within a crystal structure.

2.3.1 Quadrupolar Energy of a Nucleus

The atomic nucleus, other than electrons, are not point like, and therefore have a finite charge density. Hereby the energy of the nucleus can be written via the interaction of its charge density $\rho_{\mathrm{N}}(\vec{r})$ with an electric potential $V(\vec{r})$, produced by an electronic distribution. The following closely follows reference [16].

$$E = \int dr^3 \; \rho_{\mathrm{N}}(\vec{r}) V(\vec{r}) \tag{2.56}$$

The electric potential can be expanded, using a Taylor series about the origin:

$$V(\vec{r}) = V(0) + x_\mathrm{i}\delta_\mathrm{i}V(\vec{r}=0) + \frac{1}{2}x_\mathrm{i}x_\mathrm{j}\delta_\mathrm{i}\delta_\mathrm{j}V(\vec{r}=0) + ... \tag{2.57}$$

Here, the Einstein notation has been used, while x_i corresponds to either x,y or z depending on the value of i, and δ_i is the respective derivative. The first and the second derivative of the potential $V(\vec{r})$, namely $\delta_\mathrm{i}V$ and $\delta_\mathrm{i}\delta_\mathrm{j}V$, are the electric field V_i and the electric field gradient (EFG) V_ij, respectively. The energy of the nucleus can therefore be written as

$$E = V(0)\int dr^3\ \rho_\mathrm{N}(\vec{r}) + V_\mathrm{i}\int dr^3\ x_\mathrm{i}\rho_\mathrm{N}(\vec{r}) + \frac{1}{2}V_\mathrm{ij}\int dr^3\ x_\mathrm{i}x_\mathrm{j}\rho_\mathrm{N}(\vec{r}). \tag{2.58}$$

The first term describes the charge of the nucleus within the potential, which has a constant contribution to its energy. The second term is the interaction between the electric field $V_\mathrm{i} = \vec{E}$ and the nuclear electric dipole moment, which can be neglected. The first relevant term with respect to the series expansion is the second order term, which describes the coupling between the electric field gradient V_ij and the nuclear electric quadrupolar moment Q. Evaluating the second order term, with $Q_\mathrm{ij} = \int dr^3\ (3x_\mathrm{i}x_\mathrm{j} - \delta_\mathrm{ij}r^2)\rho$, results in the shorter expression for the integral over the charge density

$$\int dr^3\ \rho_\mathrm{N}(\vec{r})V(\vec{r}) = \frac{1}{3}\left(Q_\mathrm{ij} + \int dr^3\ \delta_\mathrm{ij}\rho_\mathrm{N}\right), \tag{2.59}$$

while δ_ij is the Kronecker delta. The resulting second order term of the nuclear electric energy becomes:

$$\begin{aligned} E^{(2)} &= \frac{1}{2}V_\mathrm{ij}\int dr^3\ x_\mathrm{i}x_\mathrm{j}\rho_\mathrm{N}(\vec{r}) \\ &= \frac{1}{6}\left(V_\mathrm{ij}Q_\mathrm{ij} + \int dr^3\ V_\mathrm{ij}\delta_\mathrm{ij}\rho_\mathrm{N}\right) \\ &\overset{V_\mathrm{ii}=0}{=} \frac{1}{6}V_\mathrm{ij}Q_\mathrm{ij} \end{aligned} \tag{2.60}$$

Moving from a classical picture into a quantum mechanical one eventually leads to the energy of the nucleus (including the Zeeman-term) [16]:

$$E_\mathrm{m} = -\gamma_\mathrm{n}\hbar H_0 m + \frac{e\tilde{V}_\mathrm{zz}Q}{4I(2I-1)}\left(\frac{3\cos^2(\Theta)-1}{2}\right)(3m^2 - I(I+1)) \tag{2.61}$$

Here, Θ is the angle between the major principle axis of the EFG and the applied magnetic field and $\tilde{V}_\mathrm{zz}$ is the largest eigenvalue of the EFG.
Transitions between those energy levels E_m define the resonance condition. For vanishing electric field gradients or quadrupolar moments, the energy difference between two nuclear states becomes $E_\mathrm{m} - E_\mathrm{m-1} = \Delta E = \gamma_\mathrm{n}\hbar H_0$, which is independent of m,

which means that all nuclear transitions are degenerate and occur under the same resonance condition with the selection rule of $\Delta m \stackrel{!}{=} 1$. For a non vanishing EFG and Q, the degeneracy of the transitions is being lifted. The quadrupolar term will vanish for the transition from $m = 1/2 \rightarrow m = -1/2$ because of the square dependence in m. Other transitions like $m = 3/2 \rightarrow m = 1/2$ will occur under unique energies and can be observed as satellite lines.

$$\Delta E = \gamma_{\mathrm{n}} \hbar H_0 + \frac{e\tilde{V}_{\mathrm{zz}} Q}{4I(2I-1)} \left(\frac{3\cos^2(\Theta) - 1}{2} \right) (3(2m-1)) \tag{2.62}$$

The form of the energy levels and the transition energies, respectively described in equations 2.61 and 2.62, is only valid in crystals with axial symmetry, where the z crystallographic axis denotes an axis with three-, four- or six-fold rotation. In lower symmetry cases, these assumptions are not valid, which is why this result has to be modified to more arbitrary field gradients:

$$V_{\mathrm{ij}} = \begin{pmatrix} V'_{\mathrm{xx}} & V'_{\mathrm{xy}} & V'_{\mathrm{xz}} \\ V'_{\mathrm{xy}} & V'_{\mathrm{yy}} & V'_{\mathrm{yz}} \\ V'_{\mathrm{xz}} & V'_{\mathrm{yz}} & V'_{\mathrm{zz}} \end{pmatrix} \tag{2.63}$$

Due to the Schwarz-Theorem $\delta_{\mathrm{i}}\delta_{\mathrm{j}} = \delta_{\mathrm{j}}\delta_{\mathrm{i}}$, the EFG is symmetric and due to the Laplace equation $\Delta V = 0$, it is traceless, reducing its maximum amount of free parameters to five. In its eigenbase, the tensor is therefore described by it largest eigenvalue $\tilde{V}_{\mathrm{zz}}$ and the asymmetry parameter $\eta = (\tilde{V}_{\mathrm{xx}} - \tilde{V}_{\mathrm{yy}})/\tilde{V}_{\mathrm{zz}}$. The primes at the matrix elements indicate that these are matrix elements in an arbitrary basis, not to be confused with the earlier used $\tilde{V}_{\mathrm{zz}}$ for an actual eigenvalue, which is independent of the base.
Using the entire EFG instead of its largest eigenvalue is rather important for non axial symmetric cases, which is why the nuclear energy, or more specific,the NMR transition Energy $\Delta E = E_{\mathrm{m}} - E_{\mathrm{m-1}}$, is written, using the actual matrix element V'_{zz} [35, 36]:

$$\Delta E = \gamma_{\mathrm{n}} \hbar H_0 + \frac{3(2m-1)}{4I(2I-1)} eQV'_{\mathrm{zz}} \tag{2.64}$$

This value is the NMR transition energy for a line depending on its magnetic quantum number m. The $m = 1/2$ line will not be shifted with respect to the Zeeman-only value, while higher lines are equidistantly shifted.
The angular dependence of this energy is compressed into the matrix element V'_{zz}. The variation of V'_{zz} under rotation yields the angular dependence of the quadrupolar interaction energy, or the NMR line splitting. The changing of V'_{zz} during rotation means, that the EFG is transformed into different bases during each individual rotation process, so that the magnetic field stays in z-direction, while the matrix itself changes.
A different, but also valid, method is keeping the EFG in the same base while rotating

the magnetic field and allowing more complex magnetic field vectors than $(0, 0, 1)$.

$$\begin{pmatrix}0\\0\\1\end{pmatrix}\begin{pmatrix}V'_{\mathrm{xx}} & V_{\mathrm{xy}} & V'_{\mathrm{xz}}\\ V'_{\mathrm{xy}} & V'_{\mathrm{yy}} & V'_{\mathrm{yz}}\\ V'_{\mathrm{xz}} & V'_{\mathrm{yz}} & V'_{\mathrm{zz}}\end{pmatrix}\begin{pmatrix}0\\0\\1\end{pmatrix} = \begin{pmatrix}x_1\\x_2\\x_3\end{pmatrix}\begin{pmatrix}V_{\mathrm{xx}} & V_{\mathrm{xy}} & V_{\mathrm{xz}}\\ V_{\mathrm{xy}} & V_{\mathrm{yy}} & V_{\mathrm{yz}}\\ V_{\mathrm{xz}} & V_{\mathrm{yz}} & V_{\mathrm{zz}}\end{pmatrix}\begin{pmatrix}x_1\\x_2\\x_3\end{pmatrix} \tag{2.65}$$

While (x_1, x_2, x_3) is a normalized vector, pointing along the magnetic field, and V_{ij} is the EFG in a fixed base. Therefore 2.64 becomes:

$$\Delta E = \gamma_{\mathrm{n}}\hbar H_0 + \frac{3(2m-1)}{4I(2I-1)}eQ\frac{\langle H|\, V_{\mathrm{ij}}\, |H\rangle}{|H|^2} \tag{2.66}$$

This more general form of the NMR transition energy can easily be reduced to the more commonly known formula 2.62 by applying axial symmetry to the EFG. With the asymmetry parameter $\eta = (V_{\mathrm{xx}} - V_{\mathrm{xx}})/V_{\mathrm{zz}} = 0$, the EFG in its eigenbase can be written as

$$V_{\mathrm{ij}} = \begin{pmatrix}V_{\mathrm{xx}} & 0 & 0\\ 0 & V_{\mathrm{xx}} & 0\\ 0 & 0 & V_{\mathrm{zz}}\end{pmatrix} \overset{\Delta V=0}{=} \begin{pmatrix}-V_{\mathrm{zz}}/2 & 0 & 0\\ 0 & -V_{\mathrm{zz}}/2 & 0\\ 0 & 0 & V_{\mathrm{zz}}\end{pmatrix}. \tag{2.67}$$

For an arbitrary magnetic field direction $\vec{H}/|\vec{H}|$, the angular dependent part of 2.66 becomes:

$$\begin{pmatrix}\sin(\theta)\cos(\phi)\\ \sin(\theta)\sin(\phi)\\ \cos(\theta)\end{pmatrix}\begin{pmatrix}-V_{\mathrm{zz}}/2 & 0 & 0\\ 0 & -V_{\mathrm{zz}}/2 & 0\\ 0 & 0 & V_{\mathrm{zz}}\end{pmatrix}\begin{pmatrix}\sin(\theta)\cos(\phi)\\ \sin(\theta)\sin(\phi)\\ \cos(\theta)\end{pmatrix} =$$

$$= V_{\mathrm{zz}}\left(-\frac{1}{2}\sin^2(\theta)\cos^2(\phi) - \frac{1}{2}\sin^2(\theta)\sin^2(\phi) + \cos^2(\theta)\right)$$

$$= V_{\mathrm{zz}}\left(-\frac{1}{2}\sin^2(\theta) + \cos^2(\theta)\right) = V_{\mathrm{zz}}\left(\frac{3\cos^2(\theta)-1}{2}\right) \tag{2.68}$$

For most applications, this expression is sufficient, however in more complex systems, it is required to apply a more general approach to the analysis of the quadrupolar interaction, given by 2.66. In order to be applicable to the experiments performed on GaV_4S_8, this formula needs to be written in terms of spin-echo modulations measured during T_2 decay experiments, which will be shown in the following.

2.3.2 Spin-Echo Modulations

The intensity of the spin echo, which is proportional to the number of nuclei subjected to the resonance condition $\omega = \omega_{\mathrm{L}}$, also has a dependence on the pulse separation time τ. The pulse separation time is important for T_2 relaxation, since the intensity follows an exponential $\exp(-2\tau/T_2)$ behaviour. With the introduction of quadrupolar

interaction to this decay curve, additional features emerge, and the intensity deviates from a simple exponential decay curve. The quadrupolar features are visible as cosine-type harmonic oscillations which are added onto the exponential curve. The quadrupolar interaction energy is proportional to the oscillation frequency, or the spin echo modulation, as it is referred to in the literature. The theory explaining its origin has been developed by Abe et al. [37] and a short overview of their work will be shown in the following part.
Here, the density matrix formalism was used. The intensity of the spin echo is proportional to the expectation value $\langle s(t)\rangle$ which is given by:

$$\langle s(t)\rangle = Tr(\sigma(t)\boldsymbol{I}) \tag{2.69}$$

Where $\boldsymbol{I}$ is the nuclear spin operator, and σ the density matrix, chosen in a way to describe the nuclear spins in an external field, while rf pulses are being applied. It is defined via the Hamiltonian

$$\frac{d\sigma(t)}{dt} = -i[\mathcal{H}, \sigma]. \tag{2.70}$$

The Hamiltonian $\mathcal{H}$ can be derived investigating the spin-echo sequence and assigning a partial Hamiltonian for each of the distinct segments, seen in Fig. 2.9 Here, for the

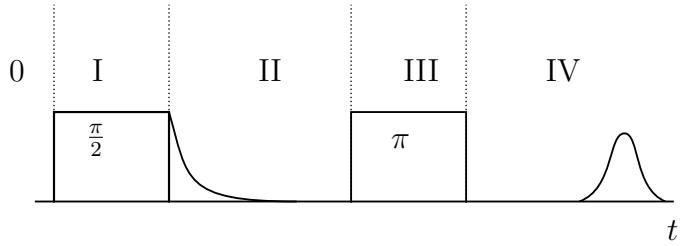

Figure 2.9: Sections of the spin-echo sequence: The Hamiltonian for each segment can be written separately. Adopted from [37].

time segments I to IV, the partial Hamiltonians are written as:

$$\hbar\boldsymbol{H}_{\mathrm{I}} = \hbar(\Delta\omega I_{\mathrm{z}} + aI_{\mathrm{z}}^2 + \omega_1 I_{\mathrm{z}}) \tag{2.71}$$
$$\hbar\boldsymbol{H}_{\mathrm{II}} = \hbar(\Delta\omega I_{\mathrm{z}} + aI_{\mathrm{z}}^2) \tag{2.72}$$
$$\hbar\boldsymbol{H}_{\mathrm{III}} = \hbar(\Delta\omega I_{\mathrm{z}} + aI_{\mathrm{z}}^2 + \omega_1' I_{\mathrm{z}}) \tag{2.73}$$
$$\hbar\boldsymbol{H}_{\mathrm{IV}} = \hbar(\Delta\omega I_{\mathrm{z}} + aI_{\mathrm{z}}^2) \tag{2.74}$$

Since the rotating frame is being used, the precession around the static magnetic field does not appear in the Hamiltonian, but since a inhomogeneity in the Zeeman energy is assumed, the term $\Delta\omega I_{\mathrm{z}}$ is used a the Zeeman term. The density matrix is being calculated by applying the propagators U_i on the density matrix for $t = 0$.

Since the Hamiltonians are time independent, the propagators are straightforward to calculate:

$$U_{\mathrm{I}} = \exp\Big(-i(\Delta\omega I_{\mathrm{z}} + aI_{\mathrm{z}}^2 + \omega_1 I_{\mathrm{z}})t_\omega\Big) \tag{2.75}$$

$$U_{\mathrm{II}} = \exp\Big(-i(\Delta\omega I_{\mathrm{z}} + aI_{\mathrm{z}}^2)(\tau - t_\omega)\Big) \tag{2.76}$$

$$U_{\mathrm{III}} = \exp\Big(-i(\Delta\omega I_{\mathrm{z}} + aI_{\mathrm{z}}^2 + \omega_1' I_{\mathrm{z}})t_\omega'\Big) \tag{2.77}$$

$$U_{\mathrm{IV}} = \exp\Big(-i(\Delta\omega I_{\mathrm{z}} + aI_{\mathrm{z}}^2 + \omega_1 I_{\mathrm{z}})(t - \tau - t_\omega')\Big) \tag{2.78}$$

The two different radio frequencies ω_1 and ω_1' indicate that arbitrary pulses have been used. In order to calculate the intensity of the NMR signal according to 2.69, the density matrix $\sigma(t)$ is calculated. The time dependence of the density matrix can be calculated by the initial density matrix for $t = 0$, before any pulses were applied, and the calculated propagators.

$$\sigma(t) = U_{\mathrm{IV}}U_{\mathrm{III}}U_{\mathrm{II}}U_{\mathrm{I}}\sigma(0)U_{\mathrm{I}}^{-1}U_{\mathrm{II}}^{-1}U_{\mathrm{III}}^{-1}U_{\mathrm{IV}}^{-1} \tag{2.79}$$

When assuming thermal equilibrium for $t = 0$, the initial density matrix can be approximated:

$$\sigma(0) = \sigma_{\mathrm{thermal}} \propto \exp\left(\frac{\hbar(\omega_0 I_{\mathrm{z}} + aI_{\mathrm{z}}^2)}{k_{\mathrm{B}}T}\right) \approx 1 + \frac{\hbar\omega_0}{k_{\mathrm{B}}T}I_z \tag{2.80}$$

While ω_0 is the resonance frequency of the center line.
Then, Eq. 2.79 is calculated explicitly via determining the matrix elements of all propagators. With these results, Abe et al. eventually calculated the quadrupolar contribution to the intensity:

$$I(2\tau) = C_0 + C_1\cos(2\tau a + \delta_1) + C_2\cos(4\tau a + \delta_2) \tag{2.81}$$

The resulting T_2 decay curve which shows the oscillation in intensity due to quadrupolar interaction can be fitted using a cosine modulated T_2 exponential decay curve [38]:

$$I(2\tau) = e^{-\frac{2\tau}{T_2}}(C_0 + C_1\cos(2\tau a + \delta_1) + ...) \tag{2.82}$$

Where C_0, C_1 are constants which determine the amplitude of the oscillation signal,τ is the pulse separation time, δ_1 is an arbitrary phase shift and the oscillation frequency a is given by:

$$a = \frac{3eQ}{8\hbar I(2I-1)}V_{\mathrm{zz}}(3\cos^2(\Theta) - 1) \tag{2.83}$$

Higher harmonics in 2.82 are neglected. The oscillation frequency a, scaling linearly with the strength of the quadrupolar interaction, here is written in a simplified EFG

case, where axial symmetry has been assumed. In order to modify this formula into the more general picture of a EFG matrix being multiplied with two field vectors, one uses Eq. 2.68.

$$a = \frac{3eQ}{4\hbar I(2I-1)} V_{zz} \frac{(3\cos^2(\Theta)-1)}{2} = \frac{3\pi eQ}{2hI(2I-1)} \frac{\left\langle \vec{H} \right| V_{ij} \left| \vec{H} \right\rangle}{|H|^2} \tag{2.84}$$

In the matrix picture, it is now straightforward to perform a more detailed analysis of the EFG if the oscillation frequency can be tracked through various values of $\vec{H}/|H|$.

Chapter 3

Multiferroicity and Lacunar Spinels

3.1 Multiferroicity

The term multiferroic refers to materials, where different ferroic orders are present simultaneously, such as ferromagnetism, ferroelectricity, ferroelasticity and ferrotoroidicity [39]. The different types of ferroic orders lead to different types of symmetry breakings. Since magnetic moments change sign upon time reversal, the ferromagnetic order breaks time reversal symmetry. Ferroelectric order on the other hand preserves the time symmetry, but breaks the spatial inversion symmetry, since the ferroelectric polarization is reversed upon inversion. Usually, the coexistance of ferroelectricity and ferromagnetism is referred to as multiferroicity, though the precise term for this case is magnetoelectric multiferroicity, as the coexistence of ferroic order parameters other than these two can also lead to multiferroicity. The surge in interest about multiferroics can be attributed to the work of Nicola Spaldin (then Hill) [40], posing the fundamental question "Why are there so few magnetic ferroelectrics?". Even though ferroelectric and magnetic ordering is often mutually exclusive due to their different driving mechanism, the quest for multiferroics inspired a new field in solid state physics, due to related phenomena of fundamental interest and the possible wide range of technical applications, such as storage devices, switches or sensors.

3.1.1 Classification and Mechanisms of Multiferroicity

Multiferroic materials may be classified into two categories, depending on how the multiferroic state is being established. The classification into two groups was proposed by Khomskii et al. [41], eventually calling them type I and type II multiferroics. In type I multiferroics the ferroelectric and ferromagnetic transition temperatures are different. In most cases, the ferroelectric structural transition occurs first at higher temperatures, with the electron spins ordering at lower temperatures within the

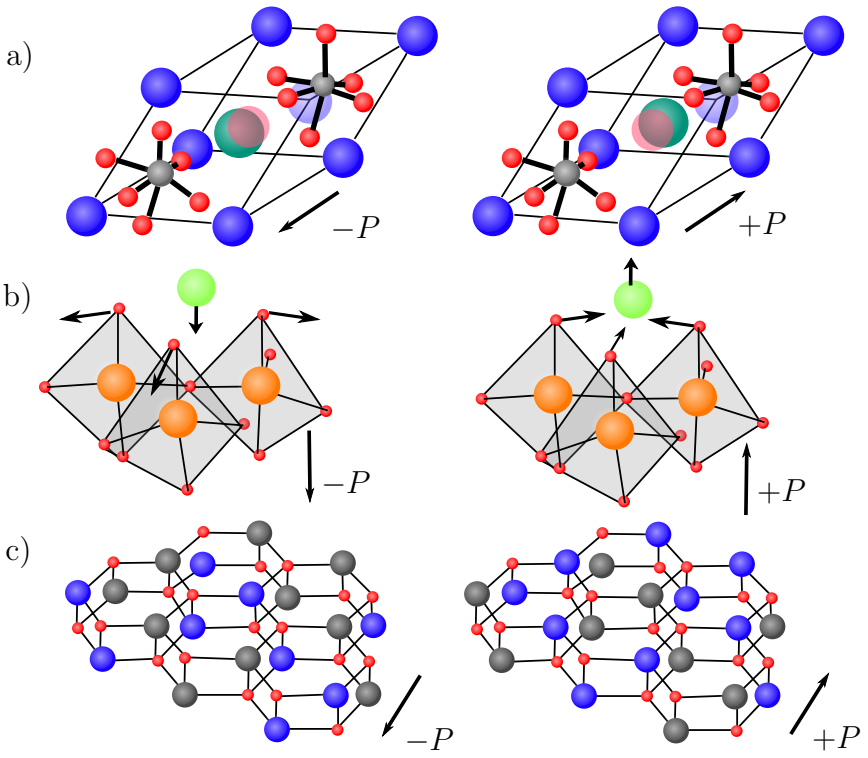

Figure 3.1: Microscopic mechanisms supporting type I multiferroicity. a) Lone pair mechanism in $BiFeO_3$ b) Geometric ferroelectricity in $YMnO_3$ c) Charge order in $LuFe_2O_3$, adopted from [42]

framework of the new crystal structure. The magnetic order is often associated with other atoms or ions in the unit cell than the ferroelectric order. In this case, the two orders are independent or only weakly connected. Type II multiferroics on the other hand, undergo their magnetic and ferroelectric order simultaneously. This is due to the ferroelectricity arising from the magnetic order itself, the so called spin-driven ferroelectricity.

Microscopic mechanisms for type I multiferroics In the following, we discuss different mechanisms of multiferroicity via representative materials and illustrate the mechanisms in Fig. 3.1. Perovskites have the chemical composition ABX_3, with prominent examples of $BiFeO_3$ and $BiMnO_3$, which are type I multiferroics. The multiferroicity is established by the lone-pair mechanism, where the off-center distortion of the A site is driven by a Bi-O hybridisation [43, 44]. The $6s^2$ lone pair of the A site ion causes the distortion due to a significant density of the 6p states below the Fermi level, which allows the hybridization with the 2p O states [43]. The B-site ion is not involved in this mechanism, and can have a partially filled d shell

and can therefore carry a magnetic moment, independently of the ferroelectricity.

In geometric ferroelectrics, instead of a hybridization, a rotational distortion of polyhedra drives the ferroelectricity, which is enabled by the small size of some A site cations. This was observed, e.g., in $YMnO_3$ [45].

Another mechanism for ferroelectricity is charge order, or orbital order. In compounds with mixed valency ions, the delocalized valence electrons can localize/order on a specific site or bond below the phase transition, inducing a ferroelectric polarization, if the electronic patterns are polar [46]. This has been observed and studied for instance in magnetite, or Fe_3O_4 [47, 48] and $LuFe_2O_3$ [49].

Microscopic mechanisms for type II multiferroics Several mechanisms have been established for spin-driven ferroelectricity with the exchange striction model, the spin current model and the spin dependent p-d hybridization models [50], which are visualized in Fig 3.2.

The exchange striction model describes the formation of a macroscopic polarization due to the symmetric part of the exchange interaction, in most cases the superexchange. The symmetric exchange depends on bond lengths and the crystal structure, thus can couple the electric and the magnetic properties. The formation of the magnetic order can cause striction along a specific crystallographic axis $\vec{\Pi}_{ij}$ depending on the spin orientations of $\vec{S}_i$ and $\vec{S}_j$, hence a finite net polarization of the material can be generated if the magnetic order is commensurate and non-centrosymmetric, and the polarization does not cancel when summing over the whole crystal [50]. The polarization is given by:

$$\vec{P}_{ij} \propto \vec{\Pi}_{ij} \cdot (\vec{S}_i \cdot \vec{S}_j). \tag{3.1}$$

This is the driving mechanism for multiferroicity in many materials, such as YMn_2O_5 [51], $DyFeO_3$ [52] and $GdFeO_3$ [53].

The spin current model, often described as inverse Dzyaloshinskii-Moriya interaction (inverse DMI), produces a polarization via the displacement of ligand ions in order to favor the DMI. The DMI, or anitsymmetric exchange, energetically favors the two neighbouring spins S_i and S_j to be perpendicular to each other [54, 55]. The Hamiltonian is given by:

$$\mathcal{H}_{ij}^{DM} = \vec{D}_{ij} \cdot (\vec{S}_i \times \vec{S}_j) \tag{3.2}$$

A finite spin orbit coupling (SOC) as well as a lack of an inversion center are prerequisites of the DMI. For magnetic orders with canted moments, a displacement of a ligand connecting two magnetic ions can decrease the energy via the DMI contribution, since the canting is enhanced when the spins are not collinear, hence inducing a ferroelectric polarization. The polarization is given by:

$$\vec{P}_{ij} \propto \vec{e}_{ij} \times (\vec{S}_i \times \vec{S}_j) \tag{3.3}$$

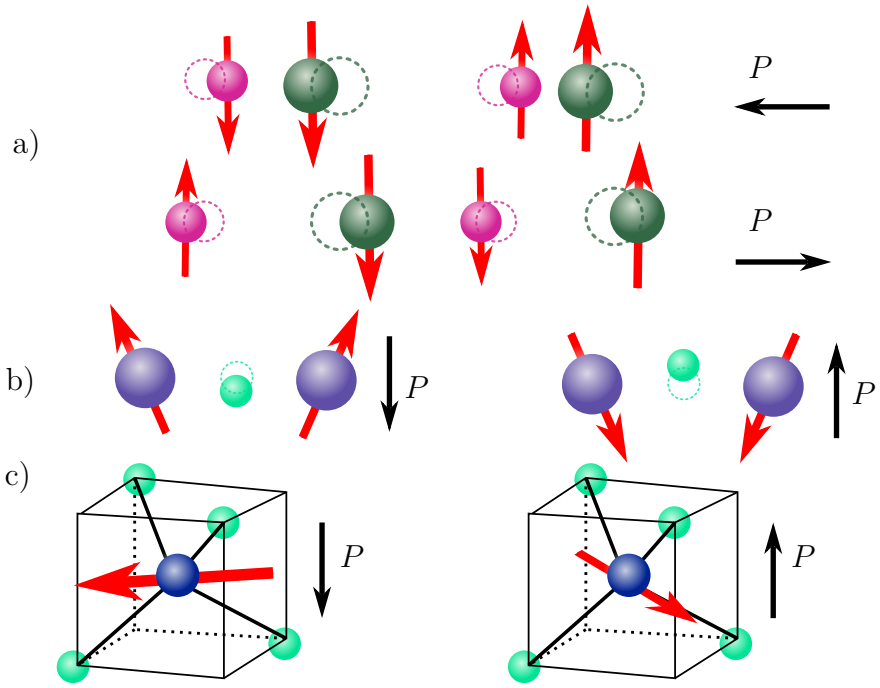

Figure 3.2: Microscopic mechanisms supporting type II multiferroicity. a) Exchange striction b) inverse DMI c) Spin dependent p-h hybridization in , adopted from [50]

Where e_{ij} is a unit vector pointing from one magnetic site to the other. This drives ferroelectricity in $LiCuVO_4$ [56, 57], $CoCr_2O_4$ [58] and $RMnO_3$(R=Tb,Dy...) [59].

The spin dependent p-h hybridization model describes a polarization, arising from the polar bond between the magnetic ion and the ligand to be dependent on spin direction. A strong spin orbit coupling drives the spin-orientation dependent hybridization, which produces a net bulk polarization, if the local polarizations do not cancel over the whole crystal. This has been observed in the collinear antiferromagnets $Ba_2CoGe_2O_7$ [60], $Ba_2MnGe_2O_7$ and $Ba_2CuGe_2O_7$ [61] as well as in the frustrated magnets $CuCrO_2$ [62] and $RbFe(MoO_4)_2$ [63].

3.1.2 Multiferroic Domains, Landau-Theory and Domain Control

A structural transition can be isomorphous, meaning that the space group of the initial and final phase are identical. Nonisomorphous phase transitions that also change the point group, are called ferroic phase transition. The loss of a point symmetry operator at the ferroic transition results in at least two equivalent states with different orientations (of the emerging polarization, magnetization or structural

distortion) [64]. Below the ferroic transition temperature T_c, connected unit cells with common polarizations, magnetizations or distortions form macroscopic regimes, called ferroic domains. With ferroelectrics as an example, the total polarization of the bulk crystal depends on the sum of polarizations of the different domains, and can be zero even after the ferroelectric transition, if the polarizations of the different domains cancel out. Similarly, ferromagnets can form domains and the overall magnetization of the sample depends on the population of domains with different orientations of the magnetization. Such ferromagnetic domains are also known as Weiss-districts [65]. In multiferroics of type I, the ferromagnetic order is embedded in the formerly established ferroelectric order, where the magnetic anisotropy (easy and hard magnetization directions) are predetermined by the distorted crystal lattice. Consequently, magnetic domains can further subdivide ferroelectric domains. In type II multiferroics, the ferroelectricity arises alongside, and is coupled to, the ferromagnetic order. Therefore, the ferroelectric and magnetic domains are occupying the same spatial regions of the crystal, and are called multiferroic domains.

The population of these multiferroic domains can be controlled via electric and magnetic fields. To understand this, we look at the Gibbs free Energy of magnetic ferroelectrics by adding the electric and magnetic term to the Gibbs free energy following reference [64]:

$$G = U + pV - ST - EP - MH. \tag{3.4}$$

Here, U is the internal energy of the system. The extensive parameters S (entropy), V (volume), P(polarization) and M (magnetization) are each multiplied by their respective intensive variables T (temperature), p (pressure), E (electric field) and H (magnetic field), each of them making a contribution to the free energy. A certain phase of a compound has specific values for the extensive parameters. The free energy can be reduced by undergoing a phase transition into a phase with different, more favourable extensive parameters, according to the Landau-theory of phase transitions, which will be introduced in the following, in close accordance with references [64,66]). In Landau-theroy, the symmetry of the crystal is being reduced by a phase transition accompanied by the emergence of an order parameter. The order parameter is zero above the critical temperature, i.e. for $T > T_c$, and rises for temperatures $T < T_c$. The free energy can then be expanded polynomially in the order parameter (usually M or P in multiferroics). Near the phase transition, the order parameter is close to zero, hence a Taylor expansion can be performed. The Landau-potential of a ferroelectric with polarization P in zero external electric field reads as [66]:

$$G = g_0 + \frac{1}{2}g_2P^2 + \frac{1}{4}g_4P^4 + ... \tag{3.5}$$

The prefactors g_i are temperature and phase dependent. Terms being odd powers of P are not allowed, as the potential should be invariant upon the symmetry of the paraelectric phase, i.e. invariant under spatial inversion. Higher order terms are

neglected. The minimum of the free energy with respect to the order parameter is most stable, hence the first derivative must vanish, while the second derivative is greater than zero:

$$\frac{\partial G}{\partial P} = g_2 P + g_4 P^3 \stackrel{!}{=} 0 \tag{3.6}$$

$$\frac{\partial^2 G}{\partial P^2} = g_2 + 3 g_4 P^2 \stackrel{!}{>} 0 \tag{3.7}$$

For the disordered phase, the order parameter P vanishes, and it is finite for the ordered phase. In order to satisfy these conditions in the ordered phase, the simplest functions of temperature for g_2 and g_4 are chosen:

$$g_2 = a(T - T_c) \tag{3.8}$$

$$g_4 > 0 \tag{3.9}$$

Here, a is a positive constant. The order parameter in the ordered phase $T < T_c$ can therefore be calculated via the non trivial solution to Eq. 3.6 [64]:

$$P^2 = -\frac{g_2}{g_4} = -\frac{a(T - T_c)}{g_4} \tag{3.10}$$

The Landau theory is phenomenological, hence the actual values for the prefactors g_i are determined by the experiment.
The application of an electric field introduces the term $-EP$ to the free energy and lowers it for phases with polarizations parallel to the electric field, and increases it for the other phases (depending on the direction of the polarization). Accordingly, the phase transition occurs in order to minimize the free energy, which will populate certain domains over others, enabling a domain control over the crystal.

Analogously, this can be done via magnetic fields for the order parameter M. The expansion in terms of magnetization M is given by

$$G = g_0 + aM^2 + cM^4 + \dots \,, \tag{3.11}$$

where a and c are temperature dependent coefficients. Combining the polarization and magnetization in the magnetoelectric effect, yields the Landau potential of magnetoelectrics [67, 68]:

$$G = g_0 - \frac{1}{2}\epsilon_0 \epsilon_{ij} E_i E_j - \frac{1}{2}\mu_0 m u_{ij} H_i H_j - \alpha_{ij} E_i H_j - \frac{\beta_{ijk}}{2} E_i H_j H_k - \frac{\gamma_{ijk}}{2} H_i E_j E_k + \dots, \tag{3.12}$$

with α_{ij} describing the linear magnetoelectric coupling, and β_{ijk} and γ_{ijk} are the second order magnetoelectric coupling coefficients.

In multiferroics, the application of magnetic fields can favour certain ferroelectric domains if, for example, the magnetic easy axis coincides with the polar axis, which is the case in certain type I multiferroic lacunar spinels, which will be introduced in the following.

3.2 Introduction to Lacunar Spinels

3.2.1 Crystal Structure and Structural Transitions

Lacunar spinels are a novel material class, which is a subdivision of spinels. Spinels share a common composition of AM_2X_4 while in lacunar spinels, every second A site is removed in an ordered fashion, resulting in the structure AM_4X_8. A-site ions occupy tetrahedral spaces, forming an A-site diamond sublattice, with the octahedral B site being organized in a pyrochlore lattice. Due to the ordered voids at the A sublattice, the pyrochlore lattice formed by the M site develops a "breathing" with smaller and larger M_4 tetrahedral clusters alternating with each other. In lacunar spinels, the A site is often occupied by Ga, Al or Ge, while the chalcogens S and Se are used for X. The M site contains transition metals of a large variety, such as V ($3d$) [69–72], Mo ($4d$) [73, 74], Nb ($4d$) [75–77] and Ta($5d$) [78, 79].
The room temperature structure of lacunar spinels is cubic and non-centrosymmetric with $F\bar{4}3m$ space group. It contains two units, the AX_4 and M_4X_4 clusters, which are organized in a NaCl-like fcc lattice, see Fig. 3.3 a). The A site is in a tetrahedral coordination with the X site, where the $A-X$ bonds point along the cubic diagonal $\langle 111\rangle$ type directions, see Fig. 3.3 b). Similarly, the M_4X_4 cluster, building a cubane, contains the two X_4 and M_4 subclusters, each building up a tetrahedron, see Fig. 3.3 c). The orientation of the X_4 tetrahedron is identical to the AX_4 tetrahedron, while the M_4 has the inverted orientation, where the $M-M$ bonds within a cluster point along the <110>-type directions, i.e. along the face diagonals of the cubic unit cell. In contrast to the ligand coordination of the A site, the M site is in a nearly octahedral crystal field at room temperature, see Fig. 3.3 d). This splits the d orbitals into t_2 and e.

The two lacunar spinels, investigated in this work, are GaV_4Se_8 and GaV_4S_8. In both compounds, the oxidation numbers for the A, M and X sites are identical. With Ga having a charge of +3, and S/Se contributing with each -2, the V_4 unit contains 12 electrons in total, for which 7 are used for metal-metal bonding [72]. This results in an unpaired electron occupying the triply degenerate t_2 molecular orbitals of the V_4 clusters, as seen in Fig.3.4.
The orbital degeneracy of the V_4 cluster therefore drives a Jahn-Teller transition by lowering the energy of one orbital via a structural distortion. The distortion elongates the V_4 tetrahedron along one of its vertices, corresponding to a stretching along one of the cubic body diagonal, $\langle 111\rangle$-type directions. The transition temperatures for the two compounds are similar with $T_{\mathrm{JT}} = 42\,\mathrm{K}$ (GaV_4Se_8) and $T_{\mathrm{JT}} = 44\,\mathrm{K}$ (GaV_4S_8). As a result of the transition, the symmetry changes from cubic ($F\bar{4}3m$) to rhombohedral ($R3m$), which also distorts the $GaS(e)_4$ tetrahedra along the same body diagonals. For each of the four possible distortion directions, one ferroelectric

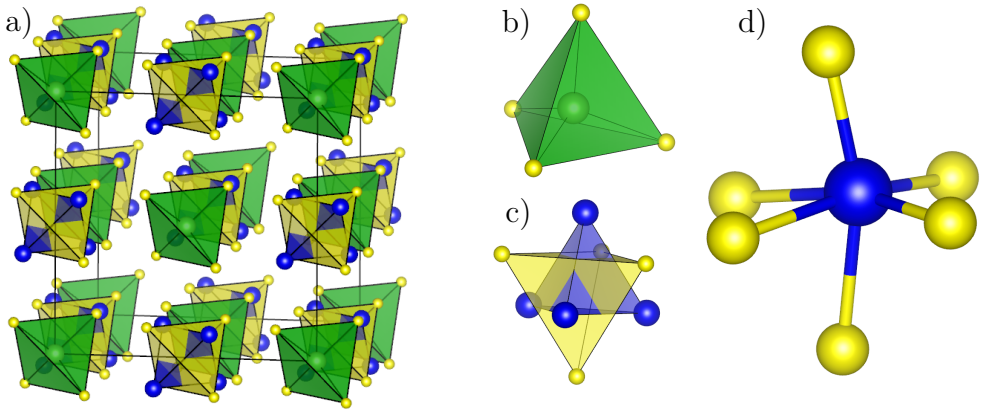

Figure 3.3: a) Crystal structure in the cubic phase of lacunar spinels AM_4X_8. b) Depiction of a AX_4 unit. c) M_4X_4 unit containing of two tetrahedra, forming a cubane. d) Near octahedral surroundings of a M site.

domain can emerge, which produces a multidomain structure upon cooling below the transition temperature T_{JT}. Additionally, the single unpaired electron in the V_4 cluster carries a spin of 1/2, which is responsible for the magnetism of these compounds, which is discussed in more detail in the following.

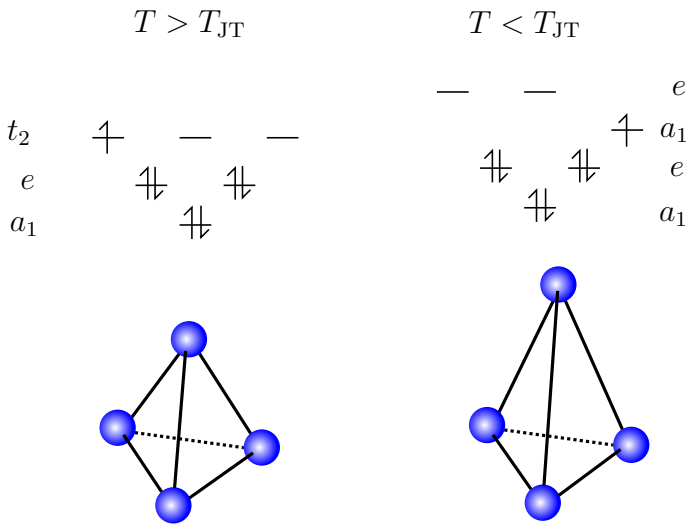

Figure 3.4: Molecular Orbital scheme and electronic configurations of GaV_4Se_8 and GaV_4Se_8. Below the Jahn Teller transition, the V_4 tetrahedron is stretched towards one of the 4 cubic diagonal [111] type directions. Adopted from [72].

3.2.2 Polar and Magnetic Properties

Since the elongation of the V_4 tetrahedron, driven by the Jahn-Teller effect, points along one of the tetrahedron's vertices, four ferroelectric domains can emerge. The charge separation created by the elongation produces a bulk polarization, with the polar axis parallel to the elongation axis. Due to the polar axes of the four domains pointing along the cubic diagonals, without inversion domains, an equal distribution of the domain population results in a zero net polarization. In real crystals however, the geometry of the sample, the direction of the temperature gradient within the cryostate, and the history of the sample can affect the domain population and can lead to finite polarization even without a poling electric field applied while cooling the crystal through T_{JT}. In general, one domain will be preferred, leading to a net polarization in the direction of the polar axis of that domain. In the following we refer to the naturally preferred polar axis as the [111] direction. This direction typically connects the largest opposing (111) surfaces of the sample. In our studies, electrical contacts are applied to these surfaces in a capacitor-like geometry.

The polarization is measured via pyroelectric current, where the current flowing from one contacted surface to the other is measured, as the sample undergoes the structural transition. Via integrating the current, the resulting charge $Q = \int I dt$ and by dividing with the surface area of the contacts, the polarization can be extracted. In Fig. 3.5a) and b), the influence of electric poling on the polarization is shown for GaV_4Se_8 and GaV_4S_8, respectively. By applying electric fields along the polar axis when cooling through the Jahn-Teller transition, a domain can be enhanced in population, or suppressed, depending on the field direction. Due to the lack of inversion domains, an opposite field direction would therefore favour the other three domains. The polarizations detected for the D1 monodomain state, where only the domain with polarization perpendicular to the contacted surfaces is populated, is $+P$. When this domain is missing and the other three, D2, D3 and D4, are populated with arbitrary fractions, the detected polarization (the projection of the polarization perpendicular to the contacts) is $-P/3$.

Below the ferroelectric ordering temperature both GaV_4Se_8 and GaV_4S_8 undergo a ferromagnetic transition at $T = 18\,K$ and $T = 13\,K$, respectively. Due to the rhombohedral distortion, magnetic anisotropy develops below T_{JT}, namely the magnetic susceptibility is different for magnetic fields applied along and perpendicular to the polar rhombohedral axis. Both compounds behave as easy-axis magnets, at least in fields above 5 T, thus magnetic fields along the rhombohedral axis lead to the highest magnetizations. This supports the magnetic selection of certain domains if a poling magnetic field is applied while cooling the sample through T_{JT}. Magnetic field applied parallel to any cubic body diagonal increases the population of the domain with polarization along this body diagonal, irrespective of the sign of the magnetic

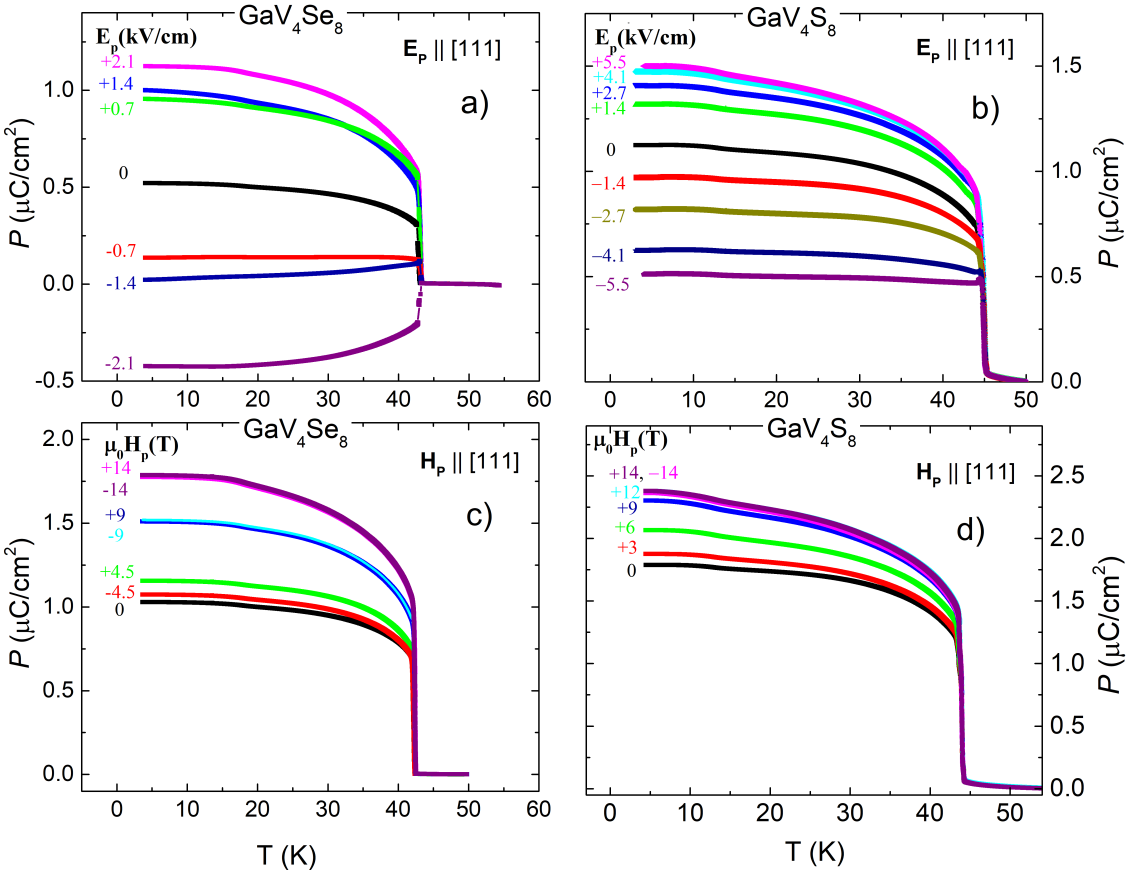

Figure 3.5: a)-b) Polarization measurement under electric field poling along the polar [111] axis for GaV_4Se_8 and GaV_4S_8. c)-d) Polarization under magnetic field poling along the magnetic easy axis [111] for GaV_4Se_8 and GaV_4S_8. The polarization was determined via the integration of the measured pyroelectric current. Credit: Lilian Prodan, Vladimir Tsurkan, Maximilian Winkler, Korbinian Geirhos and Somnath Ghara [80].

fields [81]. The latter is because the magnetic free energy in the paramagnetic state is an even function of the external magnetic field.

In GaV_4Se_8, as shown in Fig. 3.5c), it is unclear if a monodomain state was achieved due to the lack of saturation, when the highest possible poling fields were reached. In GaV_4S_8, however, as seen in Fig. 3.5 d) increasing the poling field above 12 T left the polarization unchanged, likely reaching a monodomain state.

In the low temperature regime, modulated phases emerge, forming spin cycloid or skyrmion lattice (SkL) states. The formation of the modulated phases is driven by the competition between the Heisenberg exchange and the antisymmetric exchange, also

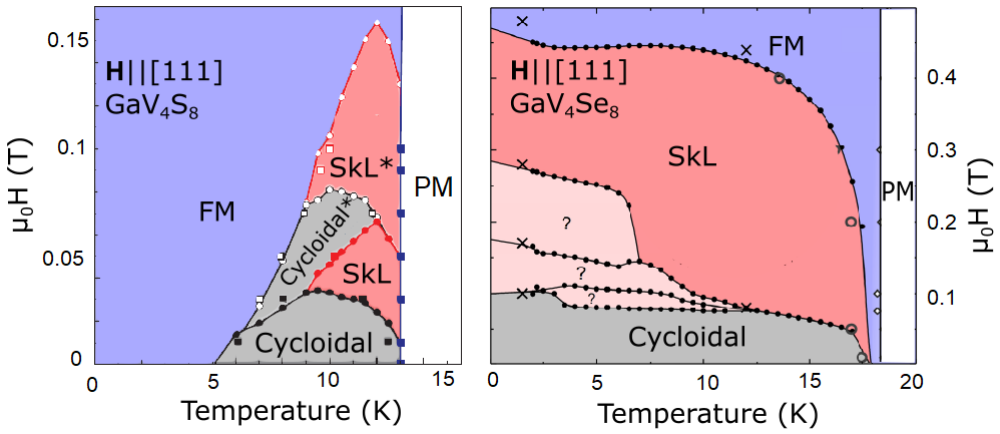

Figure 3.6: Phase diagram of GaV_4S_8 (left panel) and GaV_4Se_8 (right panel) for $\mu_0\vec{H} \parallel [111]$. The SkL and cycloidal phase extends down to the lowest temperatures in GaV_4Se_8, while GaV_4S_8 is ferromagnetic for $T < 5\,K$. The SkL* and cycloidal* correspond to the domains, where the polar axis spans 71° with the magnetic field. Adopted from [71](left) and [84](right).

knwon as Dzyaloshinskii-Moriya interaction [54, 55], which energetically favors perpendicular spin orientations, see Eq. 3.2). Due to this interaction, a canting of spins is established, giving rise to spin cycloids, helices or SkL states [71, 82–85], of which the cycloidal Neél type skyrmions (other than helical Bloch type skyrmions) were first discovered in lacunar spinels (GaV_4S_8 [71]). In GaV_4S_8 these modulated and SkL phases even carry additional polarization [86]. The phase diagrams of GaV_4Se_8 and GaV_4S_8 each containing cycloidal and SkL phases are shown in Fig. 3.6, for magnetic fields along the polar [111] axes.

The field dependent magnetization curves for both compounds are shown in Fig. 3.7 a)-b) (high field) and 3.7 c)-d) (low field). From the measurements at high fields, it is clear that the electron magnetization follows the external magnetic field, as the saturation magnetization is reached at about 2 T for both compounds and each roughly each equal in value for all directions. The small deviation between saturation magnetizations hints towards the uniaxial anisotropy tilting the electron spins slightly towards the easy axis, showing the largest magnetization at $\vec{H} \parallel [111]$. For lower fields, the magnetizations for both compounds undergo step-like changes corresponding to the phase transitions from the modulated cycloidal to skyrmion lattice (SkL) phases and from the SkL to ferromagnetic (FM) [71, 84]. In GaV_4S_8, the low-field magnetization was recorded at 10.5 K, instead of 2 K in order to observe the Cycloidal to SkL transition as well as the SkL to FM transition. Due to the multidomain character of the samples, the transitions occur at different fields for different domains because of the different orientations of the anisotropy axes. This

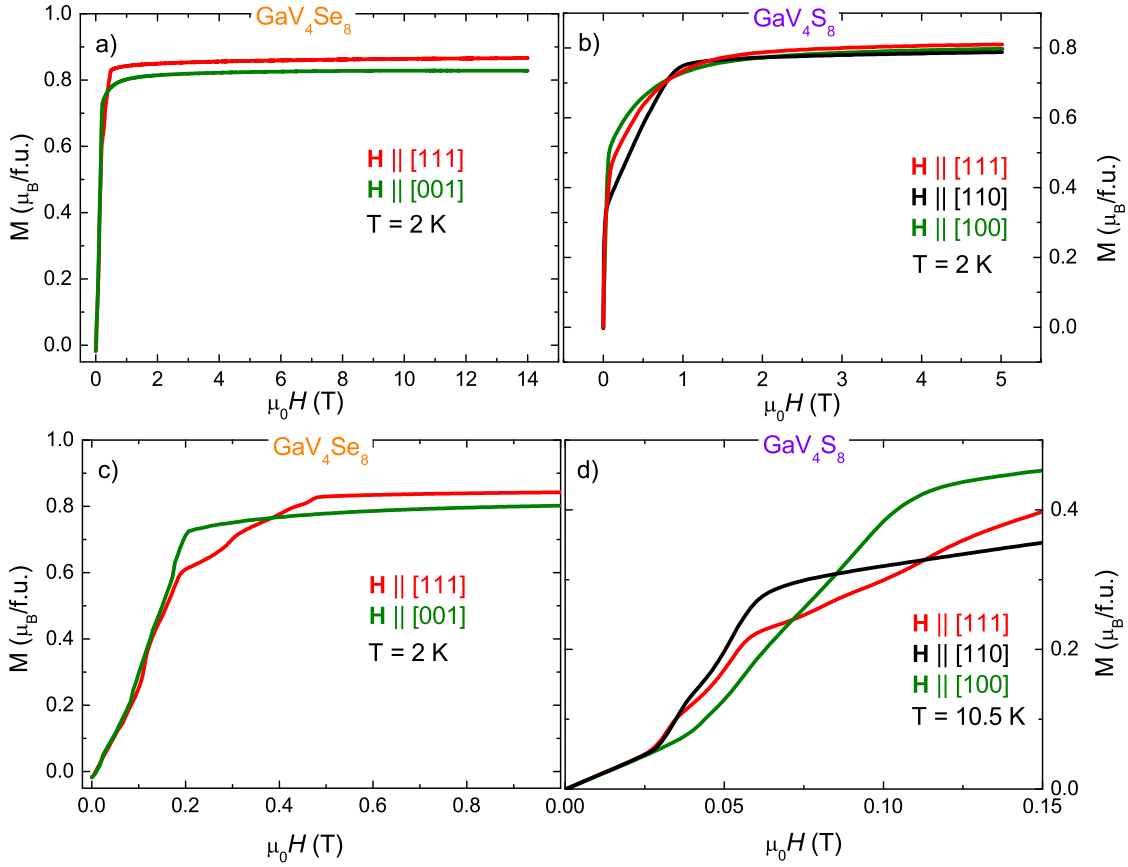

Figure 3.7: b) Magnetization curve for GaV_4Se_8 (left) and GaV_4S_8 (right). Above 2 T, the zeeman energy dominates, and the electron spins align with the applied magnetic field. Credit: Lilian Prodan, Dana Vieweg and Franz Mayr and Vladimir Tsurkan [87].

is illustrated via the SkL* and cycloidal* phases in the left panel of 3.6.

As the modulated phases in these compounds are present at small magnetic fields below 0.5 T, the necessary NMR frequencies that need to be used are very small as well, about $\nu < 5$ MHz for small internal fields. Depending on the hyperfine coupling, a measurement of the NMR signal in the modulated phases may be possible, but due to the specifics of the used spectrometer and the compounds, this study will focus on the ferromagnetic phases.

Chapter 4

Sample Preparation and Experimental Details

The NMR experiments have been performed in an Oxford variable temperature insert (VTI) in the dynamic mode. Its base temperature is 1.4k and can reach up to room temperature, however the temperature range between $4\,\mathrm{K} < T < 60\,\mathrm{K}$ was used for the actual experiments. The superconducting NbTi magnet reaches up to 9.5 T, and can be set up to reach 11 T when the the cooling liquid (^{4}He) is pumped to superfluidity("λ-stage"). A homemade spectrometer in the homodyne mode was used to record the field swept NMR spectra. Here, the signal intensity is being measured by substracting the area under the spin echo with noise of an equal length in time. While this method does not remove the noise itself from the measurement, it can eliminate offsets in the baseline, so the intensity will indeed drop to zero in the absence of a resonance signal.
In order to enhance the signal, the phase-cycling technique is used, where the phase of the 90° pulse is alternating between 0° and 180°. The two resulting time domain records of the induction voltage at the pickup coil are then subtracted from each other. Features with the same phase will then be eliminated while 180° phase shifted features will be doubled in magnitude. The 90° pulse and the resulting spin echo share the same phase, hence get doubled in magnitude, while the 180° pulse will apparently vanish(see Fig. 4.1). The phase of the echo can be understood as its refocusing direction, since it is a recorded as a DC-signal. The direction that the nuclear spins are being tilted to by the 90° pulse are phase dependent. Therefore, after the 180° pulse, the spins recombine at polar opposite directions, producing a respective negative sign. For small values of the pulse separation time τ, the spin echo can be very close to the 180° pulse, which is an additional reason to suppress the 180° pulse using phase cycling, because there might occur overlaps between the signal from the pulse and the spin echo itself.
Another influence on the quality of the measurement is the pulse duration or length T. When approximating the pulse in the time domain as a rectangle enveloping a cosine oscillating with the Larmor frequency, the resulting frequency output interacting with

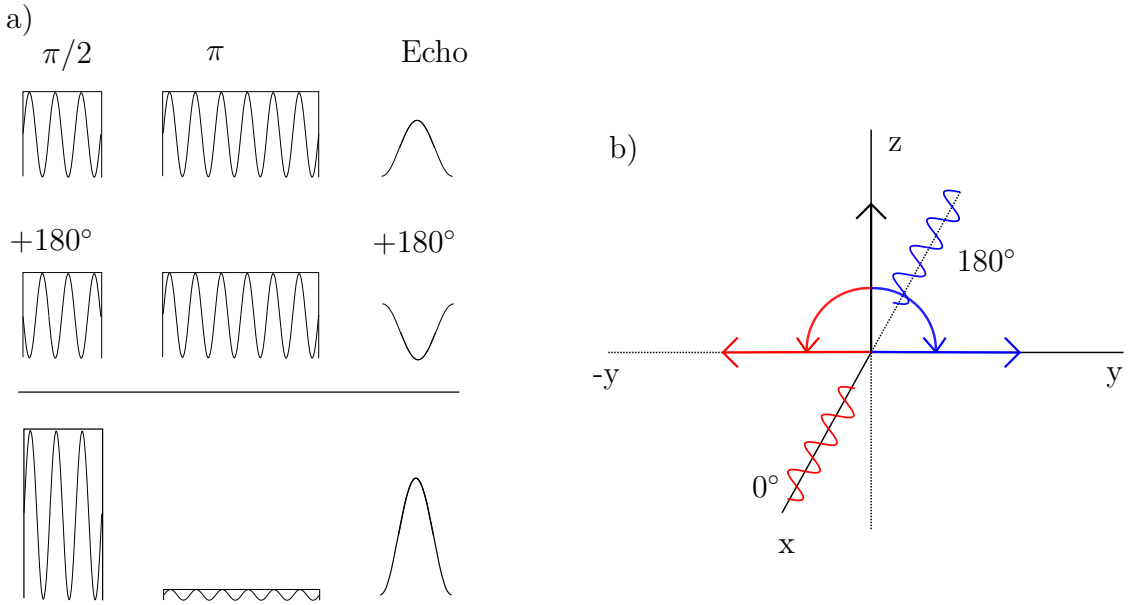

Figure 4.1: a) Effect of phase cycling on the pulse sequence. Two spin-echo sequences with different phases in the 90° pulse are being performed and subtracted. The resulting echo has twice the intensity due to the phase differences causing a summation of intensities during substraction of the spectra. b) Effect of phase cycling on the nuclear magnetization. The phase difference in the 90° pulses tilt the nuclear magnetization either in the y or $-y$ direction. The echos also recombine in opposing directions.

the sample can be calculated by Fourier transforming into the frequency domain. The rectangle function will be defined as:

$$f(t) = \begin{cases} 0 & \text{for} \quad t < -\frac{T}{2} \\ 1 & \text{for} \quad -\frac{T}{2} \leq t \leq \frac{T}{2} \\ 0 & \text{for} \quad t > \frac{T}{2} \end{cases} \tag{4.1}$$

While the oscillating waveform will be $g(t) = A\cos(\omega_{\mathrm{L}} t)$. The Fourier transform of the pulse therefore calculates as follows:

$$\tilde{f}(\omega) = \frac{1}{\sqrt{2\pi}} \int_{-\infty}^{\infty} f(t)g(t)e^{-i\omega t}dt = \frac{A}{\sqrt{2\pi}} \int_{-T/2}^{T/2} \cos(\omega_{\mathrm{L}} t)e^{-i\omega t}dt =$$

$$= \frac{A}{\sqrt{2\pi}} \int_{-T/2}^{T/2} \frac{e^{i\omega_{\mathrm{L}} t} + e^{-i\omega_{\mathrm{L}} t}}{2} e^{-i\omega t}dt = \frac{A}{2\sqrt{2\pi}} \int_{-T/2}^{T/2} e^{i(\omega_{\mathrm{L}}-\omega)t} + e^{-i(\omega_{\mathrm{L}}+\omega)t} =$$

$$= \frac{A}{2\sqrt{2\pi}} \left[\frac{1}{i(\omega_{\mathrm{L}} - \omega)} e^{i(\omega_{\mathrm{L}}-\omega)t} - \frac{1}{i(\omega_{\mathrm{L}} + \omega_{\mathrm{L}})} e^{-i(\omega_{\mathrm{L}}+\omega)t} \right]_{-T/2}^{T/2} =$$

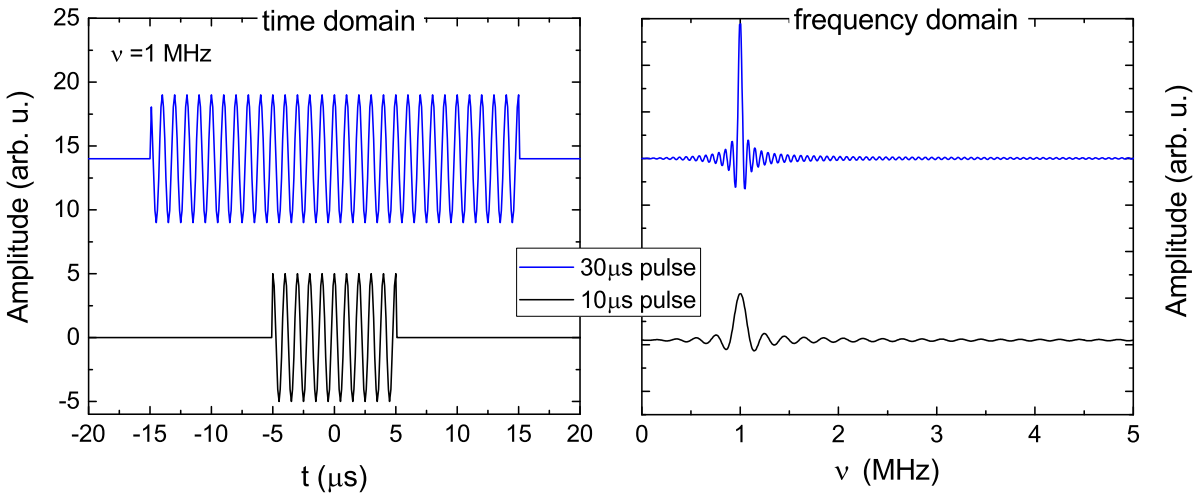

Figure 4.2: Time (left) and frequency (right) domain of a rectangular pulse with $30\mu s$ and $10\mu s$ pulses. The shorter $10\mu s$ pulses have a broader distribution of frequencies.

$$= \frac{A}{i2\sqrt{2\pi}} \left(\frac{e^{i(\omega_L-\omega)T/2} - e^{-i(\omega_L-\omega)T/2}}{\omega_L - \omega} + \frac{e^{i(\omega_L+\omega)T/2} - e^{-i(\omega_L+\omega)T/2}}{\omega_L + \omega} \right)$$

$$\tilde{f}(\omega) = \frac{A}{\sqrt{2\pi}} \left(\frac{\sin\left(\frac{T}{2}(\omega_L - \omega)\right)}{\omega_L - \omega} + \frac{\sin\left(\frac{T}{2}(\omega_L + \omega)\right)}{\omega_L + \omega} \right) \tag{4.2}$$

The solution includes negative and positive angular frequencies ω, making the solution invariant under $\omega \to -\omega$ transformation. In the graphical display, only the positive values for ω will be used. Due to the convergence of $\sin(ax)/x \overset{x\to 0}{\to} a$, larger T values will increase the amplitude at the Larmor frequency $\omega = \omega_L$ and decrease the width of the frequency window, see Fig. 4.2. For long pulses therefore, only a very small range of frequencies is being offered to the sample, which increases the resolution of the spectra. Shortening the pulses introduces an artificial broadening to the spectra as larger areas of the spectra are being excited, even with the center of the excitation window being in an off resonance position.

The measurement itself is performed by attaching the sample onto a sampleholder on a stainless steel probe, which is lowered into the cryostat, where the sample occupies a $1cm^3$ volume with magnetic fields being homogeneous down to 10 ppm. The sample itself is mounted on a non magnetic insulator using silver paste. Gold wires are connected to the top and the bottom of the sample ((111) surfaces) which will be used to apply electric fields along the [111] direction. Around the sample, the NMR pickup coil is placed in a way to have the applied external field oriented perpendicular to the rf-field of the coil, see Fig. 4.3. The whole setup including the NMR coil is

placed inside a tube, which is connected to the goniometer of the probe, and can be rotated by at least 180°, depending on the geometry of the wiring. Rotating by much larger angles might apply stress to the wires and either disturb the resonant circuit or break a soldering point.

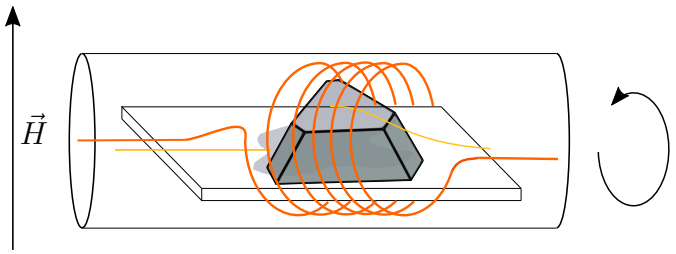

Figure 4.3: Experimental setup: The crystal is placed within the NMR pickup coil while gold wires are attached to the top and bottom (111) surfaces of the crystal, connected via silver paste. The whole setup can be rotated.

The NMR pickup coil itself needs to be wrapped around the crystal in a way, to maximize the volume fraction $V_{\text{crystal}}/V_{\text{coil}}$, in order to maximize the signal intensity. This so called "filling factor" is proportional to the density of nuclear magnetic moments within the NMR coil, and is therefore proportional to the induction voltage induced by the spin echo.
Another important quantity for signal optimization is the inductivity of the NMR coil, which is given by:

$$L = N^2 \frac{\mu_0 A}{l} \tag{4.3}$$

The length l and cross section area A are determined by the shape of the crystal, so the only free parameter is the winding number N. By choosing the wires to be as thin as feasible, a high inductivity can be reached. In order to set the frequency to the desired value, the capacitors have to be adjusted to the necessary value. Since the range of possible capacities is limited, and the thickness of the wires are at least 0.05 mm, the shape and size of the crystal roughly determines the range of frequencies it can be investigated with. In this work, the two lacunar spinels GaV_4Se_8 and GaV_4S_8 are investigated. The crystals are both grown via chemical transport reaction [83, 88]. The GaV_4Se_8 sample ATR374_1b has a mass of 9.22mg and well distinct (111) surfaces, see Fig. 4.4a). The GaV_4S_8 crystal ATR_421, with a mass of 18.8 mg is depicted in Figs. 4.4 b-d). The different rotation axes used in chapter 7.2.5 are well visible due to the clear (111) surfaces and ⟨110⟩ type axes.

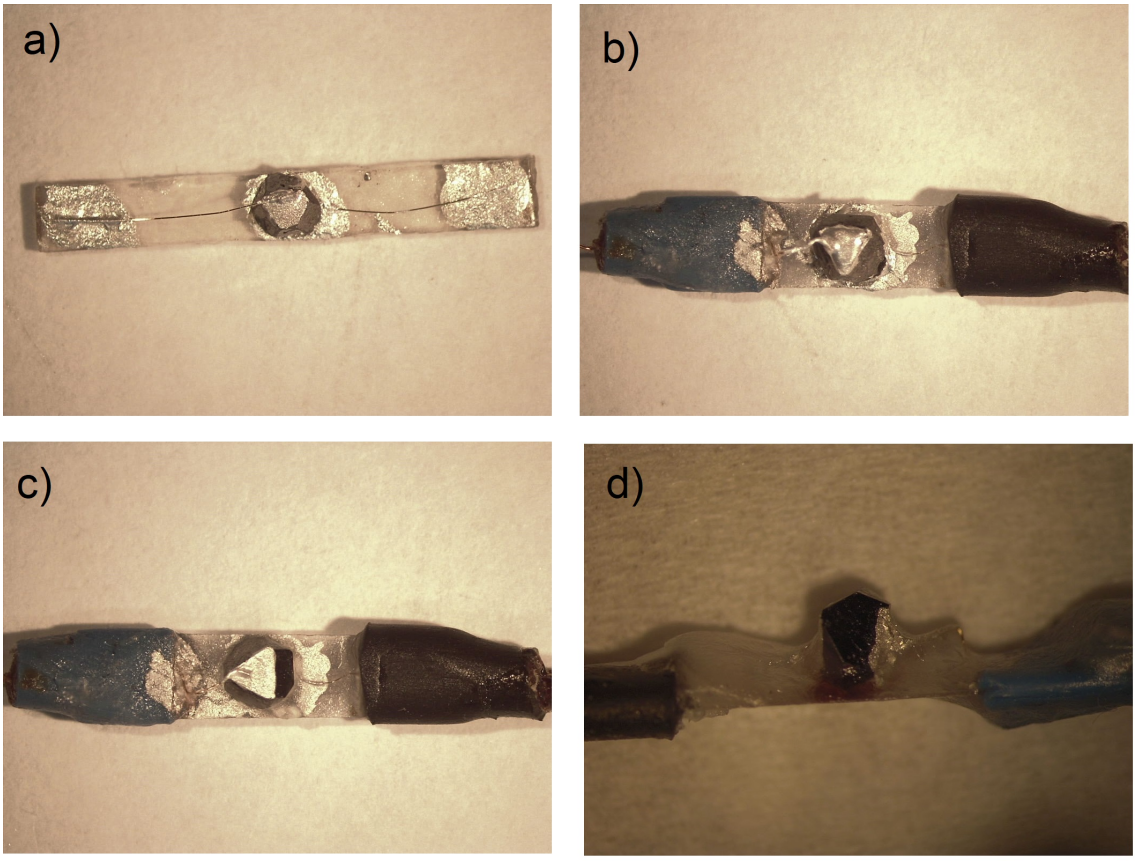

Figure 4.4: GaV_4Se_8(a) and GaV_4S_8 (b-c) single crystals with each contacted (111) surfaces. The rotation axes are [110] (a-b), [112] (c) and [111] (d)

Chapter 5

Tracing local Polarization and Magnetism via ^{71}Ga NMR spectra

The ^{71}Ga nuclei with finite quadrupolar moment of $Q = 10.7 \cdot 10^{30} \frac{1}{m^2}$ and spin $I = \frac{3}{2}$ are sensitive to electric field gradients via the quadrupolar interaction. This allows us to observe the structural transition of the lacunar spinels GaV_4Se_8 and GaV_4S_8 to their low-temperature polar state at T_{JT} and determine a local measure for the polarization, induced by the polar rhombohedral distortion. Additionally, the magnetic transition can also be followed in the NMR spectrum of ^{71}Ga. The magnetic fields transferred to the Ga sites from the magnetic V_4 clusters, causing a shift in the ^{71}Ga line, allows us to determine the temperature dependence of the magnetization that is the magnetic order parameter. The two isotopes ^{71}Ga and ^{69}Ga differ mainly in their gyromagnetic ratios and the quadrupolar moments. In order to have a clean signal, the ^{71}Ga isotope was chosen as a probe, since ^{69}Ga spectra sometimes overlap with the ^{51}V lines and nuclei originating from the experimental setup, such as ^{27}Al. In the following, the ^{71}Ga spectra and their analysis are shown and compared with either bulk measurements of the magnetization and polarization, or calculations of the local electric field gradient (EFG) at the Ga sites. Parts of these results have been published by Prinz-Zwick et al. [89].

5.1 Lineshapes

In the cubic phase right about T_{JT}, the ^{71}Ga spectra in GaV_4Se_8 and GaV_4S_8 consist of a single line, as expected due to the lack of a finite EFG at the Ga sites. The corresponding spectra are shown in Fig.5.1. The colour coding used in this chapter depicts spectra obtained for GaV_4Se_8 in orange and for GaV_4S_8 violet. The small paramagnetic moment of the V_4 cluster introduces a shift to the ^{71}Ga site via transferred fields, resulting in the rather small negative shift of $^{71}K = -0.23\,\%$ for GaV_4Se_8 and $^{71}K = -0.36\,\%$ for GaV_4S_8. The lineshape changes drastically when

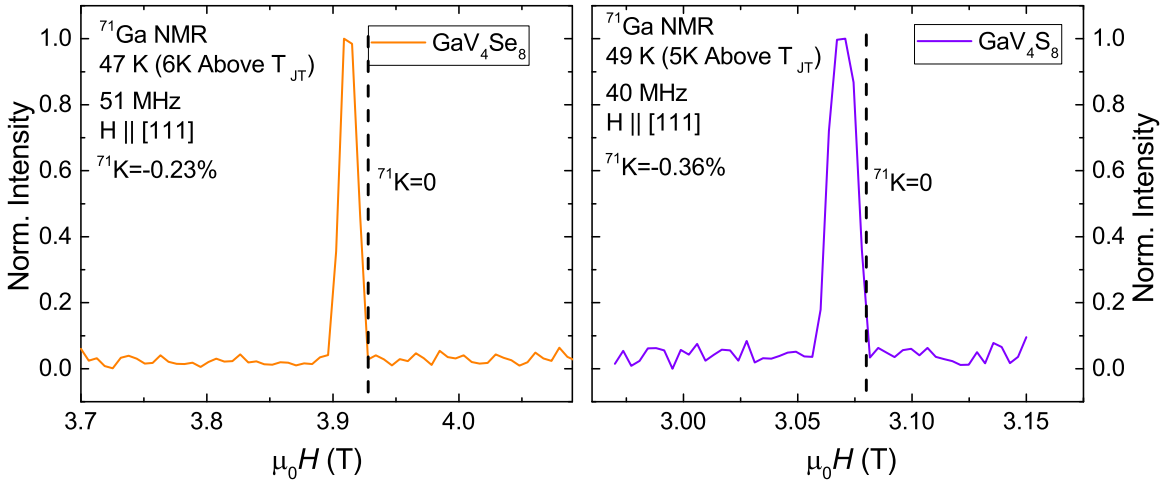

Figure 5.1: ^{71}Ga spectra of GaV_4Se_8(left) and GaV_4S_8(right) in the cubic phases above T_{JT}. A single line is observed in both cases due to the equivalence of all Ga sites above T_{JT}. A small paramagnetic shift of $^{71}K = -0.23\,\%$ for GaV_4Se_8 and $^{71}K = -0.36\,\%$ for GaV_4S_8 is present.

cooling slightly below T_{JT}, as the polar multi-domain nature of the samples is manifested in the spectra. For a given domain, the regular $GaSe_4$ and GaS_4 tetrahedra are stretched in a way, that one Se or S moves away from the Ga site, leading to rhombohedrally distorted clusters with two different Ga-S(e) bond lengths. Highly relevant to the NMR spectrum, this elongation of the tetrahedral unit, taking place along one of the cubis $\langle 111 \rangle$-type axes, generates an axially symmetric EFG with the principle axis being parallel to the direction of the rhombohedral distortion, i.e. the elongated Ga-S(e) bond (for more details on the EFG tensor, see section 5.2). The quadrupolar interaction is dependent on the angle Θ between the magnetic field $\vec{H}$ and this principle axis $\vec{V}_{zz}$, as discussed in Eq. 2.68. For $\vec{H}||[111]$, Θ is 0° for the domain with the rhombohedral axis along this direction, and Θ =71° for the other three domains with rhombohedral axes along the $[11\bar{1}]$, $[1\bar{1}1]$ and $[\bar{1}11]$ axes. This produces two distinct quadrupolar splittings in the ^{71}Ga spectra, each corresponding to their respective Θ angles, shown in Fig. 5.2. The $\Theta = 0°$ domain, can be identified as the outermost pair of quadrupolar satellite lines. The other satellite lines, corresponding to the other domains at $\Theta = 71°$, are closer to the center line. The center lines for all four different domains are roughly on top of each other, as the transferred fields due to the magnetization of the sample is still small enough at these temperatures for the central lines to overlap. The NMR spectra have the same structure for GaV_4Se_8 and GaV_4S_8, confirming the same type of distortion of the $GaS(e)_4$ units in the two compounds. With the paramagnetic moment growing upon further cooling, and the subsequent domain specific increase in the anisotropic lineshift, the center

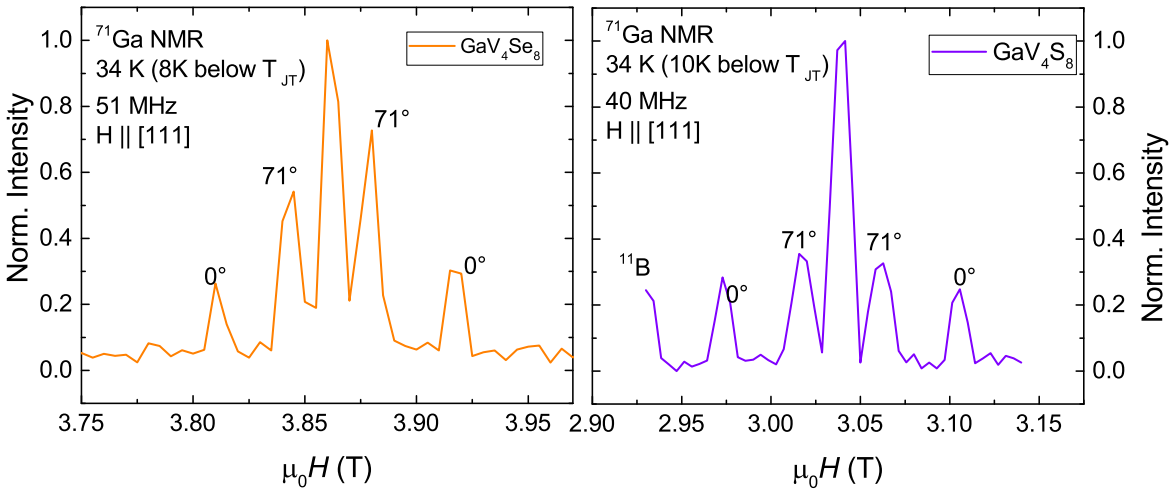

Figure 5.2: ^{71}Ga spectra of GaV_4Se_8(left) and GaV_4S_8(right) in the rhombohedral phases below T_{JT}. The line splits into two triplets below T_{JT}. Each triplet corresponds to a domain type, where the polar axis of the 0° domain is parallel with the magnetic field, and the 71° domains span an angle of 71°.

lines corresponding to the different domains eventually split as seen close to or below the ferromagnetic transition. The quadrupolar pattern (line splitting and distance to central line) stays roughly the same, since the EFG is not influenced by the magnetism of the sample, as it is only depending on the site symmetry and the charge distribution. The increase in lineshift as well as the unchanged quadrupolar patterns are shown in the spectra taken at 4.2 K, seen in Fig. 5.3. The quadrupolar pattern can still be fitted well, when introducing the anisotropic hyperfine shift, which also distinguishes the different domains due to the different angles spanned by the field with their rhombohedral axes. In the case of GaV_4Se_8, five separate lines are visible in total, while in GaV_4S_8 lines from the different domains overlap in a way that a total of four lines are observed.

In conclusion, the different lineshapes of ^{71}Ga NMR spectra were discussed, based on temperature. Above T_{JT}, all Ga sites are equivalent, with the absence of domains, resulting in a single line. For $T_N < T < T_{JT}$, the spectra show different quadrupolar splitting for each domain while the center lines are overlapping due to the hyperfine shifts being still small. Below T_N, the lineshifts become large enough to split the center lines of different domains, while the quadrupolar splitting stays unchanged.

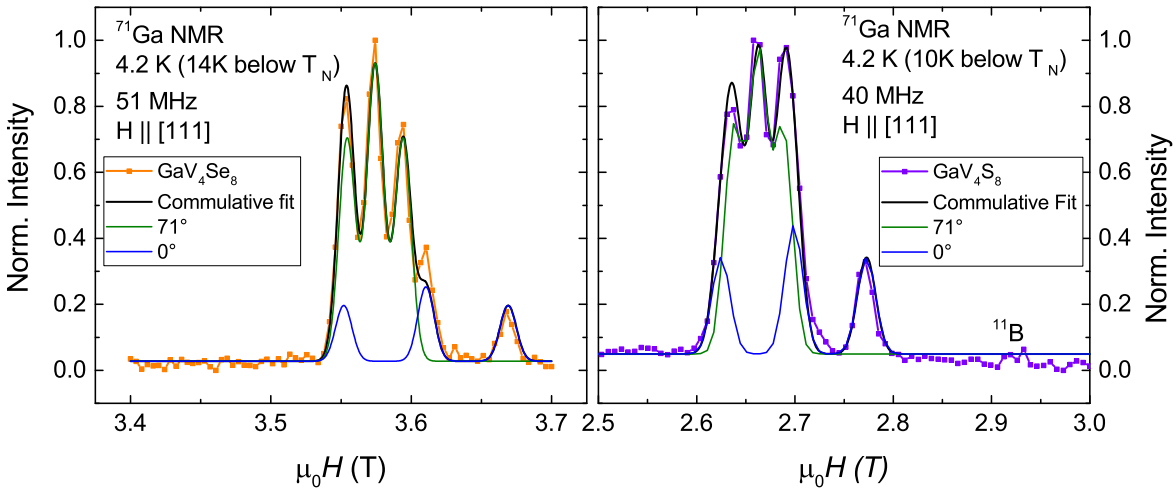

Figure 5.3: ^{71}Ga spectra of GaV_4Se_8 (left) and GaV_4S_8 (right) in the ferromagnetic phases below T_N. The lines exhibiting quadrupolar splitting are shifted in the magnetically ordered state. The internal fields at the Gallium site show a nonzero anisotropy as the center lines for the different domains shift with respect to each other (fits were performed according to Eq. 5.10, presented in the next section).

5.2 Quadrupolar Interaction Analysis

The local symmetry of the ^{71}Ga site in $GaS(e)_4$ clusters determines the shape of the EFG, and therefore how the quadrupolar interaction influences the NMR spectra. As seen in Fig. 5.1, the NMR spectra show no quadrupolar splitting in the cubic phase. The ^{71}Ga resides in the center of a regular $S(e)_4$ tetrahedron, not giving rise to a finite EFG, as sketched in Fig. 5.4. When the tetrahedron gets elongated towards the [111] direction, the EFG must therefore have an axial symmetric shape, with $\vec{V}_{zz} \parallel [111]$. The elements of the EFG tensor (given in the diagonal form), as calculated by ab initio Density Functional Theory (DFT) reflect this symmetry (Credit: Pavel Marton [90]):

$$V_{ij} = \begin{pmatrix} -5 & 0 & 0 \\ 0 & -5 & 0 \\ 0 & 0 & 10 \end{pmatrix} \frac{V}{\text{Å}^2} \qquad (GaV_4Se_4)$$

$$\eta = 0 \qquad \vec{V}_{zz} = \frac{1}{\sqrt{3}} \begin{pmatrix} 1 \\ 1 \\ 1 \end{pmatrix} \qquad V_{zz} = -10 \frac{V}{\text{Å}^2} \tag{5.1}$$

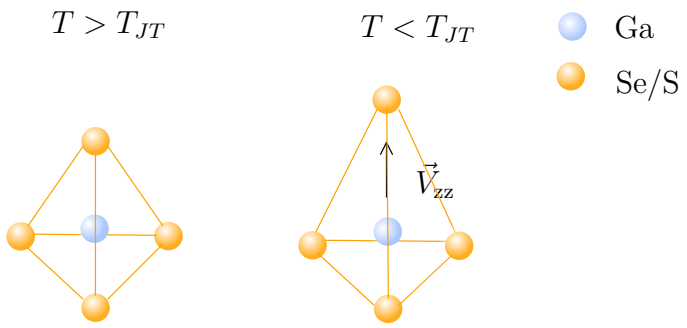

Figure 5.4: $GaS(e)_4$ cluster above and below T_{JT}. In the cubic state, no EFG is present. Due to the elongation towards the [111] axis in the rhombohedral state, an axial symmetric EFG arises with $\vec{V}_{zz} = [111]/\sqrt{3}$.

$$V_{ij} = \begin{pmatrix} 6.3 & 0 & 0 \\ 0 & 6.3 & 0 \\ 0 & 0 & -12.6 \end{pmatrix} \frac{V}{\text{Å}^2} \qquad (GaV_4S_4)$$

$$\eta = 0 \qquad \vec{V}_{zz} = \frac{1}{\sqrt{3}} \begin{pmatrix} 1 \\ 1 \\ 1 \end{pmatrix} \qquad V_{zz} = 12.61 \frac{V}{\text{Å}^2} \tag{5.2}$$

This statement about the shape of the EFG can easily be checked by looking at a ^{71}Ga spectrum with the field pointing along the [001] direction. The polar rhombohedral axis of each of the four domain spans the same angle with the magnetic field, making the domains equivalent with respect to the quadrupolar interaction as well as the hyperfine interaction, hence, the satellites corresponding to the different domains collapse on each other. In addition, according to the angular dependence in Eq. 2.62, the quadrupolar interaction vanishes at the so called "magic angle" of θ =55°, spanned by all four possible polar axes have with the magnetic field, if $\vec{H} \parallel [001]$. From this, the shape of the low temperature spectrum in the FM phase follows directly. Even below T_{JT}, no quadrupolar splitting should be observed, even in a multi-domain crystal. This is demonstrated in Fig. 5.5.

With this understanding, the spectra for $\vec{H} \parallel [111]$ will be used to analyse the quadrupolar interaction for the ^{71}Ga site. In order to do so, the quadrupolar frequency will be used as the orientationless measure of the quadrupolar interaction, as given by [17]:

$$\nu_Q = \frac{3eV_{zz}Q}{2hI(2I-1)} \tag{5.3}$$

In the field swept spectra, the quadrupolar splitting is observed as a difference in the resonance field, which is due to the change in energy of the Zeeman levels for the different nuclear spin states. From Eq. 2.61 the energy difference of the nuclear

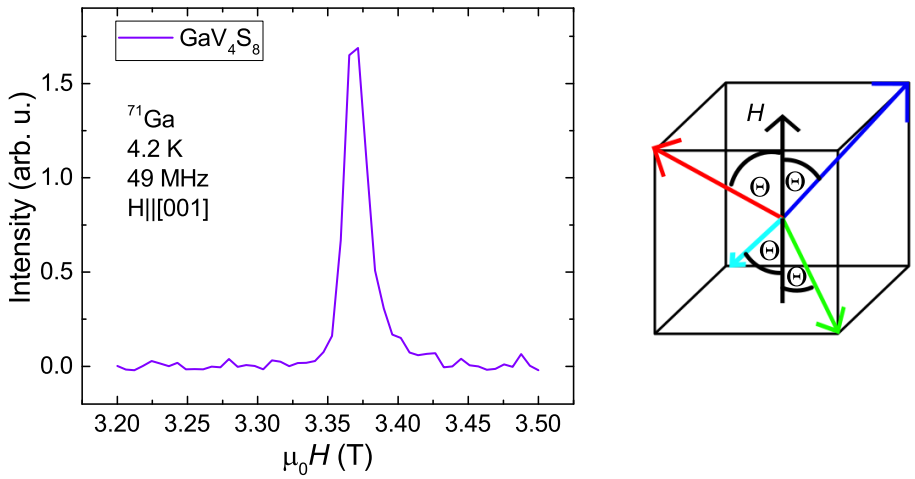

Figure 5.5: Left: ^{71}Ga spectrum of GaV_4S_8 in the ferromagnetic phase with $\vec{H} \parallel [001]$. No quadrupolar splitting is observed due to the angle $\Theta \approx 55°$ being close to the magic angle. The domain specific internal fields are also each equivalent. Right: Depiction of the domains being equal under $\vec{H} \parallel [001]$.

states and the difference in resonance fields can be calculated. For simplicity,

$$\Delta E = E_{\pm 3/2} - E_{\pm 1/2} = \gamma\hbar H_0 \pm \frac{eV_{zz}Q}{4I(2I-1)}\left(3\left(\pm\frac{3}{2}\right)^2 - 3\left(\pm\frac{1}{2}\right)^2\right)\frac{3\cos^2(\Theta)-1}{2} =$$

$$= \gamma\hbar H_0 \pm \frac{3eV_{zz}Q}{2I(2I-1)}\frac{3\cos^2(\Theta)-1}{2} = \gamma\hbar H_0 \pm \nu_Q h\frac{3\cos^2(\Theta)-1}{2} \tag{5.4}$$

The $\pm$ signs are used due to two different satellite lines appearing for transitions $1/2 \rightarrow 3/2$ and $-3/2 \rightarrow -1/2$, which will have their energy differences either increased or decreased, respectively. One has to note here, that the hyperfine coupling is anisotropic, i.e. H_0 also depends on Θ. This is the reason why the central peaks corresponding to the unique ($\Theta = 0°$) and the other three ($\Theta = 71°$) domains do not overlap below the magnetic ordering, as seen in Fig. 5.3.

In the case of $\Theta = 90°$, this energy difference is $\Delta E = \nu_Q h/2$, as shown in Fig. 5.6 to illustrate the fitting process. There, the quadrupolar frequency can be easily extracted graphically by observing the resonance field difference ΔH_Q between the satellite lines, since Θ is known. For the case of $\Theta = 90°$, the field difference of the satellites divided by γ of the nucleus equals ν_Q directly. With arbitrary Θ angles the field difference between the center line and one satellite becomes (for ^{71}Ga)

$$\Delta H_Q = \frac{\nu_Q}{^{71}\gamma}\frac{(3\cos^2(\Theta)-1)}{2}. \tag{5.5}$$

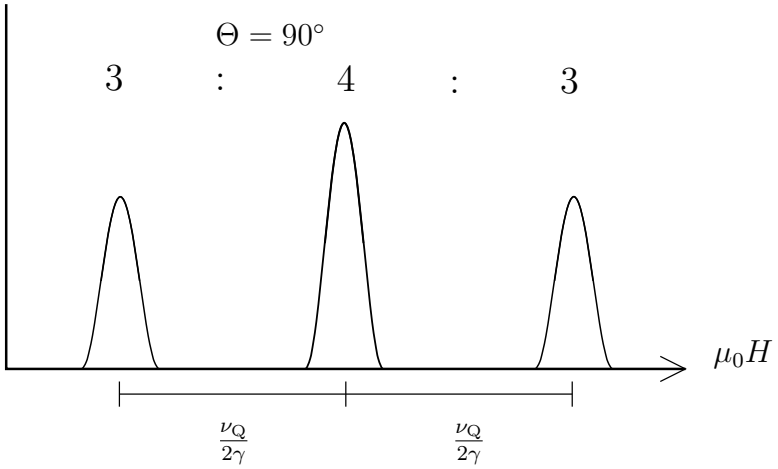

Figure 5.6: Schematic depiction of a NMR spectrum of a $I = 3/2$ nucleus with $\Theta = 90°$. The distance between the satellite lines can be translated into the quadrupolar frequency directly.

After determining the quadruppolar frequency, we analyse the hyperfine shift, that is the line shift due to the magnetic fields transferred to the Ga nucleus from the magnetic $V_4S(e)_4$ clusters. In the eigenbase of the hyperfine coupling tensor (z axis is the [111] direction, as the polar angle is determining the internal fields), it is written as a diagonal matrix

$$\mathcal{A}_{\mathrm{HF}} = \begin{pmatrix} H_{\mathrm{xx}} & 0 & 0 \\ 0 & H_{\mathrm{xx}} & 0 \\ 0 & 0 & H_{\mathrm{zz}} \end{pmatrix} \tag{5.6}$$

Where H_{xx} is the double degenerate eigenvalue with respect to the base vectors perpendicular to the z direction. This description, only utilizing the external field direction, is valid for fully saturated field regimes, which can be used since all NMR measurements were performed in the field aligned case. The internal field is then described as

$$\vec{H}_{\mathrm{int}} = \mathcal{A}_{\mathrm{HF}} \frac{\vec{H}_{\mathrm{ext}}}{H_{\mathrm{ext}}} = \begin{pmatrix} H_{\mathrm{xx}} & 0 & 0 \\ 0 & H_{\mathrm{xx}} & 0 \\ 0 & 0 & H_{\mathrm{zz}} \end{pmatrix} \begin{pmatrix} \sin\Theta\cos\phi \\ \sin\Theta\sin\phi \\ \cos\Theta \end{pmatrix} =$$

$$= H_{\mathrm{xx}} \begin{pmatrix} 1 & 0 & 0 \\ 0 & 1 & 0 \\ 0 & 0 & 1 \end{pmatrix} \frac{\vec{H}_{\mathrm{ext}}}{H_{\mathrm{ext}}} + (H_{\mathrm{zz}} - H_{\mathrm{xx}}) \begin{pmatrix} 0 & 0 & 0 \\ 0 & 0 & 0 \\ 0 & 0 & 1 \end{pmatrix} \begin{pmatrix} \sin\Theta\cos\phi \\ \sin\Theta\sin\phi \\ \cos\Theta \end{pmatrix} =$$

$$= H_{\mathrm{iso}} \frac{\vec{H}_{\mathrm{ext}}}{H_{\mathrm{ext}}} + H_{\mathrm{aniso}} \begin{pmatrix} 0 \\ 0 \\ \cos\Theta \end{pmatrix} \tag{5.7}$$

As seen in Fig. 5.3, the magnetic moment of the $V_4S(e)_4$ cluster introduces a lineshift to the ^{71}Ga spectra depending on the domain, since the hyperfine coupling for the Ga site with distorted environment is anisotropic and described by a tensor. The anisotropic lineshift depends on the angle Θ. For GaV_4Se_8, the lineshift at 4.2 K is given by ^{71}K= -8.8%, and for GaV_4S_8, ^{71}K= -19.1% for $\Theta = 0°$. The hyperfine coupling shifts the center line and the satellites equally and has no influence on the quadrupolar term, and therefore does not influence the quadrupolar frequency parameter. A very simple model for the hyperfine fields at the ^{71}Ga sites used in the fitting process is a cosine function, capturing the anisotropic hyperfine amplitude H_{aniso}. Therefore the position of the center lines H_{CL} are described by

$$H_{\text{CL}}(\Theta) = H_{\text{diam}} + H_{\text{int}}. \tag{5.8}$$

Where H_{diam} is the diamagnetic Gallium position. The positions of the satellites are closely related to the center line:

$$H_{\text{Sat1,2}} = H_{\text{diam}} + H_{\text{int}} \pm \frac{\nu_{\text{Q}}}{^{71}\gamma} \frac{(3\cos^2(\Theta) - 1)}{4} \tag{5.9}$$

The resulting fit formula used for the ^{71}Ga spectra is a simple sum of two triplet Gaussian lines, with each triplet accounting for one type of domain, either $\Theta = 0°$ or $\Theta = 71°$:

$$\begin{aligned}\text{Int}(H) = A_1 \left(e^{\frac{(H-H_{\text{CL}}(0°))^2}{2w^2}} + R_s e^{\frac{(H-H_{\text{Sat1}}(0°))^2}{2w^2}} + R_s e^{\frac{(H-H_{\text{Sat2}}(0°))^2}{2w^2}} \right) + \\ + A_2 \left(e^{\frac{(H-H_{\text{CL}}(71°))^2}{2w^2}} + R_s e^{\frac{(H-H_{\text{Sat1}}(71°))^2}{2w^2}} + R_s e^{\frac{(H-H_{\text{Sat2}}(71°))^2}{2w^2}} \right)\end{aligned} \tag{5.10}$$

A_1 and A_2 are the intensity factors for the two domain types, which can be used to measure domain populations (see chapter 6). The width of the Gaussian is described by w, and R_s is the intensity ratio between the satellite lines and the center line, usually around 3/4 for $I = 3/2$ [91].

With this, the values for V_{zz} obtained by DFT and the experiment via fits of the 4.2 K spectra can be compared. For GaV_4Se_8, $V_{zz} = 5.88$ V/Å^2 (DFT : 10.0 V/Å^2), and for GaV_4S_8, $V_{zz} = 7.31$ V/Å^2 (DFT : 12.6 V/Å^2), which is in rough agreement.

In conclusion, the quadrupolar splitting of the ^{71}Ga spectra together with the axial symmetry of the Ga site in the rhombohedral phase was utilized to determine the EFG tensor. Using the fit formula shown above, the temperature dependence of the quadrupolar frequency and other properties are deduced and shown in the following subsection.

5.3 Local Probes of the Order Parameters

The ferroelectric transition below 42 K and 44 K in GaV_4Se_8 and GaV_4S_8, respectively, is accompanied by a spontaneous emergence of a bulk polarization, which is the order parameter of the transition. The ferromagnetic transition ($T_N = 18$ K in GaV_4Se_8 and $T_N = 14$ K GaV_4S_8) gives rise to a bulk magnetization associated with the V_4Se_4 and V_4S_4 clusters. Both the bulk polarization and the magnetization can be measured via local probes, utilizing the quadrupolar splitting and the hyperfine fields, respectively. In Fig. 5.7, the temperature dependence of the ^{71}Ga NMR spectra are shown for both compounds. The emerging quadrupolar linesplitting at T_{JT} corresponds to the electric polarization, which vanish above T_{JT}, where only a single line is observed. For each spectrum, the quadrupolar frequency is extracted via the fitting method described in the previous subsection. The center line of the 0° domain is then used to determine the lineshift of the ^{71}Ga lines. To demonstrate the ability of NMR to determine multiple order parameters simultaneously, we compare the temperature-dependent quadrupolar frequency with the bulk ferroelectric polarization and the hyperfine field with the bulk magnetization. The curves, normalized to their value at 4.2 K, are shown in Fig. 5.8. In both materials, the local probes of the order parameters are agreeing with the bulk data, providing the possibility to measure electric and magnetic properties of the multiferroic compounds via NMR. Studying the quadrupolar interaction can therefore give additional insight into the ferroelectric nature of the compounds, where a detailed study of the lineshifts allows us to deeper understand the magnetism of the molecular clusters. Note that the lineshifts of ^{51}V lines are included in Fig. 5.8, which are introduced in chapter 6. Both ^{71}Ga and ^{51}V exhibit a finite lineshift as well as a quadrupolar interaction, which makes both nuclei great candidates for further investigation, however more focus will be drawn towards the ^{51}V nucleus, as the $V_4S(e)_4$ cluster drives the Jahn-Teller transition as well as the complex magnetism in both multiferroic compounds.

In conclusion, the NMR parameters, namely the quadrupolar splitting and the hyperfine shift, were compared with the order parameters, namely the bulk polarization and magnetization, respectively. The local polar distortion and magnetic moments of the $V_4S(e)_4$ cluster drive the bulk polarization and magnetization, respectively, and therefore correlate well with NMR measurements. In the following, the knowledge about the local order parameters, and their connection to the multiferroic domains, will be used to quantify domain populations.

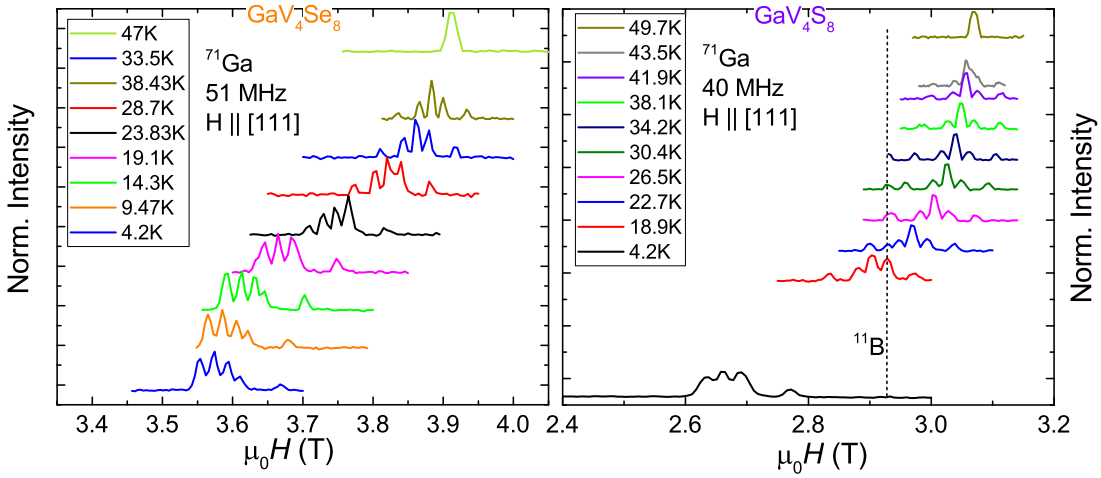

Figure 5.7: Temperature dependence of the ^{71}Ga spectra for GaV_4Se_8(left) and GaV_4S_8(right). The magnetic shift as well as the quadrupolar frequency can be traced from the ferromagnetic to the cubic state. The ^{11}B line is an artifact line originating from the experimental setup.

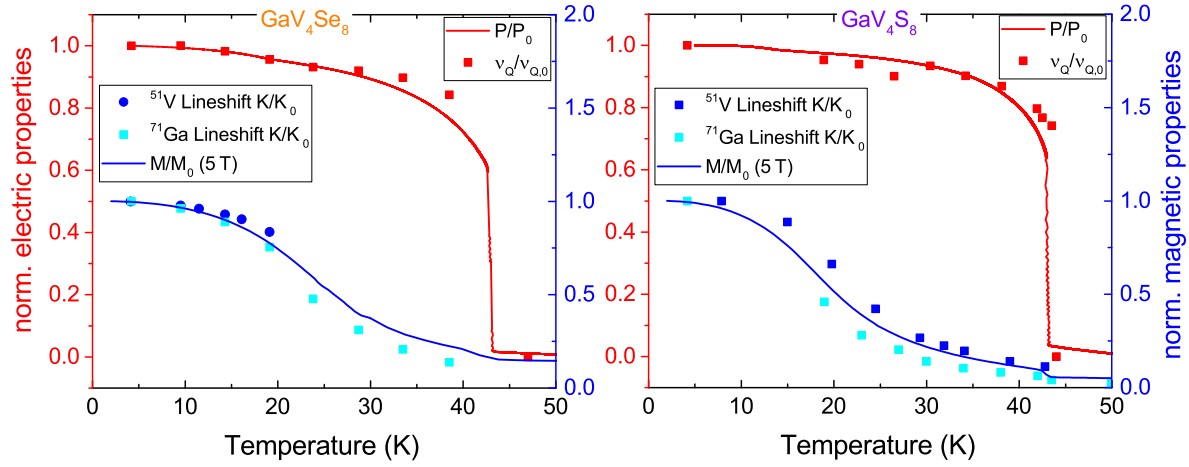

Figure 5.8: Normalized quadrupolar frequency $\nu_Q/\nu_{Q,0}$, normalized polarization P/P_0(each red), normalized lineshift K/K_0 and normalized magnetization M/M_0 (each blue) versus temperature for GaV_4Se_8(left) and GaV_4S_8 (right). The order parameter P is being measured locally via ν_Q, while the lineshift measures the magnetization. The data was normalized via division with the values obtained at 4.2 K. Data obtained from ^{51}V spectra, which will be discussed in detail in chapter 6.2, was added for completion.

Chapter 6

Measuring Domain Populations via local Probes of the Order Parameters

NMR is a local probe, which measures properties such as EFGs and/or internal magnetic fields at the position of the nucleus, however, the spin-echo intensity originates from the nuclei in the entire bulk crystal. The NMR intensities, which consist of a sum of signals of individual nuclei, are proportional to the number of nuclei contributing to the magnetic resonance. This motivates a deeper look at intensity ratios of NMR lines, which depend on microscopic properties, and also allows conclusions about volume fractions of magnetic and/or polar domains. In many applications, T_2 decay experiments are used to determine the ratio of two co-existing thermodynamic phases via the same type of nucleus [92, 93]. We propose a similar approach that is applicable for the quantification of (multi)ferroic domains by NMR spectroscopy. We describe different methods for domain quantification in multiferroics using the benchmark material GaV_4Se_8, and demonstrate their power in following the evolution of domain population upon electric and magnetic domain control. In GaV_4Se_8, four domains are present, one for each of the possible [111] type axes of elongation of the V_4Se_4 cluster. The two domains with their polar axes within the (110) magnetic field rotation plane are called D1 and D2, while the other two are D3 and D4. The introduction to the domain quantification methods will partly follow reference [94], which was a joint effort with Thomas Gimpel. However, the following sections describe these domain-quantification approaches in more detail.

6.1 Measuring Domain Populations via Quadrupolar Interaction

As seen in the previous chapter, the quadrupolar interaction at the ^{71}Ga nucleus is anisotropic, since the principle axis of the EFG is parallel to the polar axis of each domain. For NMR spectra taken below T_{JT}, depending on the orientation of the

external field, the quadrupolar satellite lines originating from different domains can be resolved independently. The paramagnetic moment of the V_4Se_4 cluster shifts the ^{71}Ga lines anisotropically. In order to have the central lines of the different domains on top of each other, the hyperfine coupling should be reduced as much as possible, hence the best temperature range to investigate the polar domain structure of GaV_4Se_8 is slightly below $T_{JT} = 42\,K$ and well above $T_N = 18\,K$, where the magnetization is still weak. Therefore, the field-swept spectra were taken at $T = 38.5\,K$. Assuming that the orientation of the magnetic field does not influence the nuclear spin relaxation rates, nor does it change the relative intensities of the corresponding NMR lines of different domains by any other means, the comparison between the intensities of the corresponding quadrupolar satellites of the different domains should yield the domain population directly. Since the quadrupolar interaction is rather weak in the special case of ^{71}Ga in GaV_4Se_8, there is no such orientation of the magnetic field, where peaks from the different domains can be resolved without any overlap. Instead, spectra from different orientations must be compared with each other, and intensities from overlapping lines must be subtracted. Nevertheless, at least two distinct methods for quantifying domain populations are possible using the ^{71}Ga spectra, which will be shown in the following.

The polar axis method

In this method the NMR spectra are measured for two orientations of the magnetic field, namely for fields parallel to the [111] polar axis of D1 and the $[\bar{1}\ \bar{1}1]$ polar axis of D2. Consequently, as seen from the spectra in Fig. 5.2, two distinct pairs of satellite lines appear for the two possible orientations. In Fig. 6.1, the spectra for the two external field directions are shown, for each of the two [111]-type directions. The outer satellite lines ($\theta = 0°$) correspond to a single domain, while the inner satellite lines ($\theta = 71°$) are an overlap of the remaining three domains. The intensities of D1 and D2 can therefore be directly measured via the are under the curve in the respective field orientations. The lines corresponding to domains D3 and D4 are always contained within the inner satellites. For each of the two field orientations, an intensity value for D3+D4 can be calculated via subtraction of intensities.

$$I_{H\|P1}(D3 + D4) = I_{H\|P1}(D2 + D3 + D4) - I_{H\|P2}(D2) \tag{6.1}$$

$$I_{H\|P2}(D3 + D4) = I_{H\|P2}(D1 + D3 + D4) - I_{H\|P1}(D1) \tag{6.2}$$

Here, the index of I refers to the external field direction where the spectrum was taken, and the argument refers to the domain, of which the satellite line was integrated. If the intensity values $I_{H\|P2}(D3 + D4)$ and $I_{H\|P1}(D3 + D4)$ are identical within the accuracy of the measurement, then the aforementioned assumption, proposing an invariance of satellite intensities upon changing the field direction, is

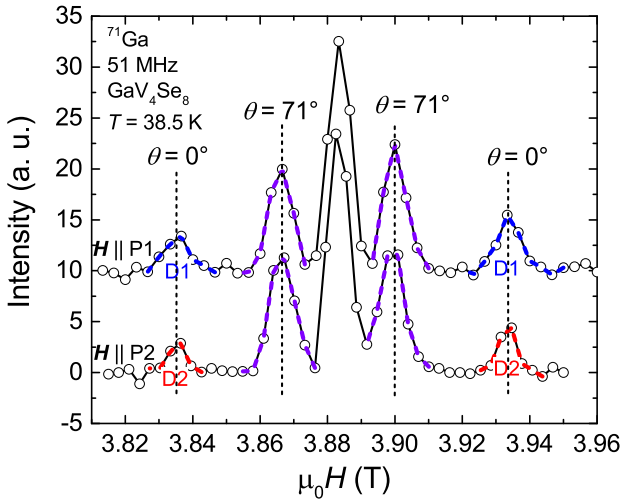

Figure 6.1: ^{71}Ga spectra, taken in the process of measuring domain populations via the polar axis method. For $\vec{H} \parallel P_1(P_2)$, the satellites at the $\theta = 0°$ position correspond to D1 or D2. The $\theta = 71°$ satellite lines contain contributions from the other three domains.

confirmed. Since this is observed to be the case, the domain fractions can be calculated straightforward.

$$V(D1) = \frac{I_{H\parallel P1}(D1)}{I_{H\parallel P1}(D1) + \frac{1}{2}(I_{H\parallel P1}(D3+D4) + I_{H\parallel P2}(D3+D4)) + I_{H\parallel P2}(D2)}$$

$$V(D2) = \frac{I_{H\parallel P2}(D2)}{I_{H\parallel P1}(D1) + \frac{1}{2}(I_{H\parallel P1}(D3+D4) + I_{H\parallel P2}(D3+D4)) + I_{H\parallel P2}(D2)}$$

$$V(D3+D4) = \frac{\frac{1}{2}(I_{H\parallel P1}(D3+D4) + I_{H\parallel P2}(D3+D4))}{I_{H\parallel P1}(D1) + \frac{1}{2}(I_{H\parallel P1}(D3+D4) + I_{H\parallel P2}(D3+D4)) + I_{H\parallel P2}(D2)} \tag{6.3}$$

For the spectra shown in Fig. 6.1, the volume fractions therefore are:

$$V(D1) = 27.5\% \quad V(D2) = 17.4\% \quad V(D3+D4) = 55.1\% \tag{6.4}$$

The 90° method

In this approach, the magnetic field is chosen to have an angle of 90° with the polar axes of the observed domains. This is realized by rotating from one field orientation, with perpendicular alignment with respect to the polar axis of one domain, to the next. The chosen field rotation plane is a $(1\bar{1}0)$ plane. Beginning from $\vec{H} \parallel [001](\phi =$

0°), these perpendicular configurations appear at the angles of $\phi = 35°$ (D2), $\phi = 90°$ (D3+D4) and $\phi = 145°$ (D1), corresponding to the crystallographic axes [112] (D2), [110] (D3+D4) and [11$\bar{2}$] (D1). In Fig. 6.2 the spectra measured at these field orientations are shown. Due to the quadrupolar splitting being proportional to $(3\cos^3\Theta - 1)$, the position of the satellites is identical for $\Theta = 90°$ and $\Theta = 35°$, which makes it unavoidable to have line overlaps for $\vec{H} \parallel [110]$, as all domains are oriented either at $\Theta = 35°$ or $\Theta = 90°$ in this case. In the spectra $\vec{H} \parallel [112]$ and $\vec{H} \parallel [11\bar{2}]$, D1 and D2 can each be measured separately, whereas D3 and D4 overlap with the central line. In order to obtain the intensity of satellite lines for D3 and D4, the intensities of D1 and D2 must be subtracted from the intensities of the overlapping satellite lines in the $\vec{H} \parallel [110]$ spectrum. With a total of four satellite lines each representing D1 and D2, the intensities will be averaged.

$$I(D1) = \frac{1}{4}\left(I_{[112],1}(D1) + I_{[112],2}(D1) + I_{[11\bar{2}],1}(D1) + I_{[11\bar{2}],2}(D1)\right) \tag{6.5}$$

$$I(D2) = \frac{1}{4}\left(I_{[112],1}(D2) + I_{[112],2}(D2) + I_{[11\bar{2}],1}(D2) + I_{[11\bar{2}],2}(D2)\right) \tag{6.6}$$

The intensities $I(D1)$ and $I(D2)$ are the average intensities of the satellite lines, corresponding to D1 and D2, respectively. The average is taken over all satellites of the same domain in all spectra, where the satellite lines are resolved independently. Those individual intensities of single satellite lines have the field direction and their number (left=1, right=2) as an index. Similarly, $I(D3 + D4)$ calculates as:

$$I(D3 + D4) = \frac{1}{2}\left[I_{[110],1}\left(\sum_{i=1}^{4} D_i\right) + I_{[110],2}\left(\sum_{i=1}^{4} D_i\right)\right] - I(D1) - I(D2) \tag{6.7}$$

The sums in the argument of the intensity functions describe the stacking of the satellite lines of all domains on top of each other for the field direction $\vec{H} \parallel [110]$. The volume fractions then are:

$$V(D1) = \frac{I(D1)}{I(D1) + I(D2) + I(D3 + D4)} \tag{6.8}$$

$$V(D2) = \frac{I(D2)}{I(D1) + I(D2) + I(D3 + D4)} \tag{6.9}$$

$$V(D3 + D4) = \frac{I(D3 + D4)}{I(D1) + I(D2) + I(D3 + D4)} \tag{6.10}$$

For the spectra shown in Fig. 6.2, which were measured in the same cooling run as the spectra in Fig. 6.1, the volume fractions are:

$$V(D1) = 28.3\% \quad V(D2) = 17.3\% \quad V(D3 + D4) = 54.4\% \tag{6.11}$$

This is in very good agreement with the previous method. Additionally, this approach has been verified using a different method based on ^{51}V NMR which will be covered in the following sections. The volume fractions obtained from the ^{51}V method (90° method) in the same cooling run are:

$$V(D1) = 27.2\% \quad V(D2) = 21.3\% \quad V(D34) = 51.5\% \tag{6.12}$$

Small differences in the percentages may well be due to the rather small signal to noise ratio of the ^{71}Ga spectra, as the higher temperatures used for the spectra reduce the intensity due to relaxation effects and the Boltzmann factor.

In conclusion, two methods were shown, utilizing the different quadrupolar splittings in ^{71}Ga spectra originating from different domains. The intensities of domain specific quadrupolar satellite lines were recorded, and the relative intensities were then used to calculate the domain fractions.

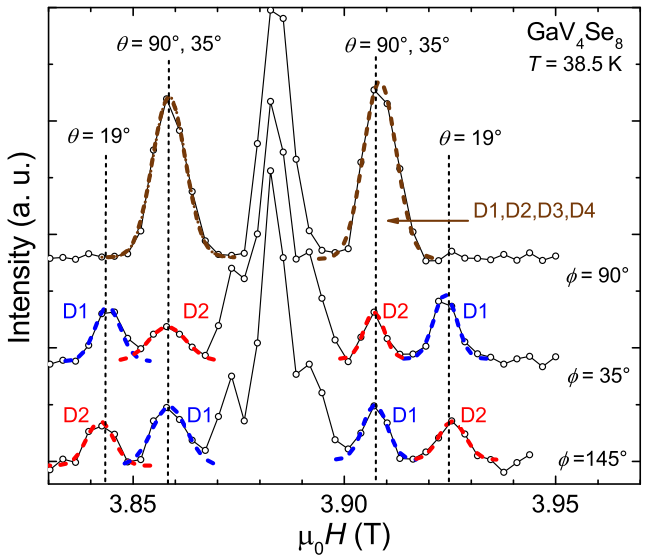

Figure 6.2: ^{71}Ga spectra, taken in the process of measuring domain populations via the the "90° method". The satellite lines for $\vec{H} \parallel [110]$ contains contributions from all domains, while satellite lines originating from D1 and D2 are resolved individually for $\vec{H} \parallel [112]$ and $\vec{H} \parallel [11\bar{2}]$.

6.2 Temperature and Angular Dependence of the ^{51}V Spectra

With vanadium being the magnetic ion, the ^{51}V NMR spectra are rich in information about the magnetism of the material. In the cubic phase, however, the lack of distinct domains and the small hyperfine fields due to the paramagnetic moment restricts fruitful measurements to temperatures below T_{JT}. There, ^{51}V NMR probes the magnetization via hyperfine lineshift and yields information about the different multiferroic domains, as seen in Fig. 6.3. For both GaV_4Se_8(left) and GaV_4S_8(right), the lineshift follows the bulk magnetization (see Fig. 5.8 in the previous chapter, where the ^{51}V lineshifts were already shown).

The ^{51}V spectra in GaV_4Se_8 could not be detected above 20 K, probably due to a large increase in the T_2 relaxation rate approaching T_{JT}. Faster T_2 relaxation rates increase the decay of the in-plane magnetization $\vec{M}$xy after the initial 90° pulse, which reduces the spin-echo intensity. In GaV_4S_8, the ^{51}V lines were traced up to 52 K, well above the Jahn-Teller transition temperature. In GaV_4Se_8, the chosen field orientation for the temperature dependent spectra was the [111] direction, where three domains are equivalent. In GaV_4S_8 an arbitrary axis was chosen (approximately [0.12 0.12 0.98]), in order to have a field orientation where all domains are inequivalent. This already indicates, that the magnetic field direction is crucial for the shape of the vanadium spectra as it determines whether the lines corresponding to different domains are separated or overlapping. The magnitude of the hyperfine shift directly correlates with the bulk magnetization as seen in Fig. 5.8, which is the reason why the ^{51}V line shifts towards the diamagnetic position ^{51}K= 0, when approaching higher temperatures. Since the largest magnetic moment and therefore the largest lineshift is present at the lowest temperatures, the angular dependence of the ^{51}V spectra were recorded at 4.2 K. In order to have all high symmetry axes (namely the $\langle 111\rangle$ $\langle 110\rangle$ and $\langle 001\rangle$-type directions) in one field rotation, the magnetic field was rotated about the $[1\bar{1}0]$ direction. When rotating the field in the $(1\bar{1}0)$ plane, the multiferroic domains in GaV_4Se_8 and GaV_4S_8 separate in two categories depending on whether the polar axis lies within or outside of the field rotation plane. The polar axes of D1 and D2 are within the field rotation plane, wheras the polar axes of D3 and D4 are each equivalent under this rotation and point outside of this field rotation plane. In Fig. 6.4, the ^{51}V spectra under field rotation can be seen for GaV_4Se_8(left) and GaV_4S_8(right). For both materials, the angular dependence is nearly identical, indicating a very similar hyperfine coupling tensor. The angle θ between the polar axis and the magnetic field is the strongest contributing parameter for the resonance field for a specific domain, while ϕ is the field rotation angle with respect to the starting position [001]. The maximum lineshift is reached when the polar angle is $\theta = 90°$, in other words when the magnetic field lies within the base plane of the V_4 tetra-

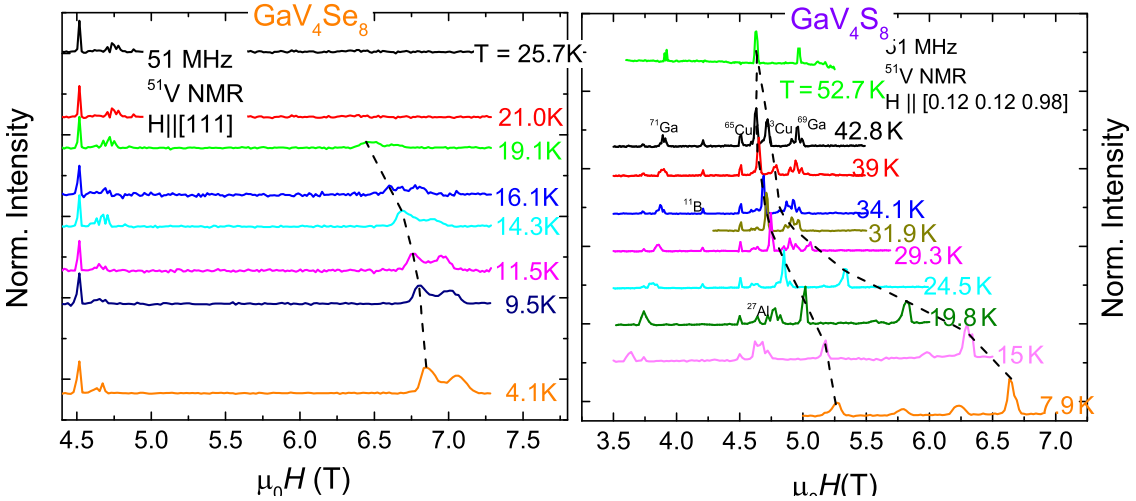

Figure 6.3: Temperature dependence of the ^{51}V spectra for GaV_4Se_8(left) and GaV_4S_8(right). The signal is lost above 20 K in GV_4Se_8 presumably due to fast T_2 relaxation. The different lines corresponding to the different domains converge at T_{JT} due to the vanishing lineshift and the disappearance of polar domains. The dashed lines indicate the temperature dependence of the hyperfine fields for the cases of minimal or maximal hyperfine coupling.

hedron. The different spectra were recorded with 10° steps, which means that some specific orientations were missed by about 5°, but can be extrapolated by the nearest spectra. In fact the lowermost spectrum, is 5° misaligned from [001]. At $\vec{H} \parallel [001]$, all polar axes span an angle of $\theta = 55°$ with the magnetic field, making the domains equivalent, resulting in the ^{51}V NMR lines overlapping. Due to a misalignment, D3 and D4 are not equivalent and the lines do not perfectly merge.
After rotating by $\phi = 35°$ from [001], the polar axis of D2 spans a polar angle of 90° with the magnetic field, where its maximum lineshift is observed. At $\phi = 55°$, the [111] direction is reached, where the lines corresponding to D2, D3 and D4 overlap with each a the polar angle of $\theta = 71°$, while D1 exhibits its smallest lineshift at $\theta = 0°$. Note that D1 is close to the ^{51}V diamagnetic position here, which means that all internal fields cancel out in this field direction. In the [110] position at $\phi = 90°$, D1 and D2 are equivalent as $\theta = 35°$ for both domains. D3 and D4 are in their θ =90° position, causing the corresponding lines to have their maximum lineshift. At $\phi = 125°$ another [111] position is reached, where $\theta = 0°$ for D2 and $\theta = 71°$ for D1, D3 and D4. D1 reaches its maximum lineshift at $\phi = 145°$, corresponding to $\vec{H} \parallel [11\bar{2}]$. Note that all NMR lines corresponding to the different domains eventually reach the same point of maximum lineshift at a polar angle of $\theta = 90°$ within a full rotation. This fact will be utilized later when determining the domain population of

these domains.
After 180°, the starting position is recovered. The strong anisotropy of the hyperfine field (2.7 T from minimum to maximum) is well suited for analysing the different domains independent of each other. This will be done in the following section in order to measure the domain populations based on the anisotropy of the hyperfine field. The following studies of the domain populations will focus on data obtained by GaV_4Se_8 NMR.

In conclusion, the temperature and angular dependence of the ^{51}V spectra were recorded. The orientation of the magnetic field with the polar axes of the multiferroic domains determines the angular dependence of the hyperfine shift, which can be each different for different domains. Above T_{JT}, all lines originating from different domains converge.

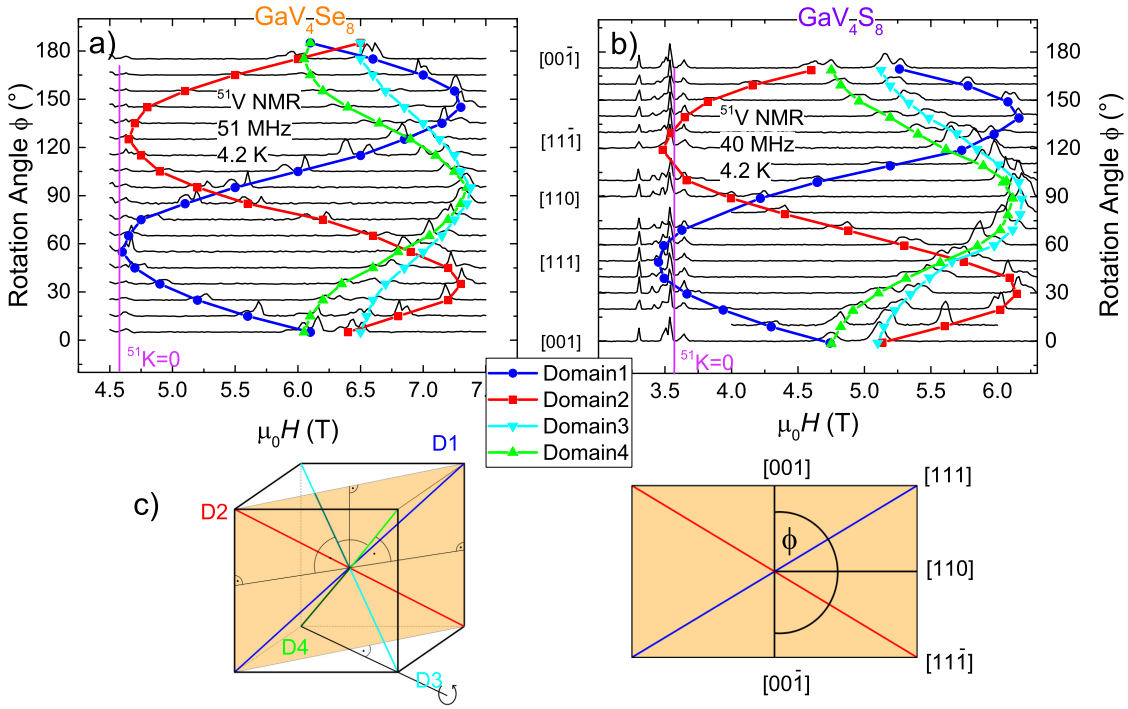

Figure 6.4: ^{51}V spectra originating from the four different domains in GaV_4Se_8(a) and GaV_4S_8(b), measured under 180° rotation about the $[1\bar{1}0]$ axis. The polar axes of D1 and D2 are within the field rotation plane, and therefore exhibiting the strongest anisotropy of the hyperfine field. Small misalignments lift the degeneracy of D3 and D4, which can be resolved individually for the majority of the angular range. c) Depiction of the rotation plane within the $V_4S(e)_4$ cubane

6.3 Measuring Domain Populations via Anisotropy of the Hyperfine Coupling

As already seen in the Figs. 5.7 and 6.4, the ^{71}Ga and ^{51}V spectra show the presence of multiple domains in the form of line splittings. In the case of ^{71}Ga, the splitting is of quadrupolar nature and domain specific as discussed in the previous chapter. For ^{51}V, the local magnetic moment of the $V_4S(e)_4$ cluster drives a strong hyperfine coupling. Its anisotropy is causing a line splitting in the NMR spectra, as different domains have different hyperfine fields at the V sites. This anisotropy can be used to separate NMR lines corresponding to different domains and investigate them individually. By doing so, several methods can be thought of, on how to utilize the anisotropy of the hyperfine coupling in the ^{51}V spectra to measure the domain population of GaV_4Se_8. The three methods shown in the following use either the full angular range of spectra, just one spectrum in a specific field orientation or each domain at a θ =90° angle between the field and the particular polar axes of the domains, where θ will be called "polar angle".

The full angular range method

From Fig. 6.5 it is apparent, that the intensities of the NMR lines for each domain follow an angular dependence, similar to the anisotropy of the resonance fields $\mu_0 H_{\mathrm{Res}}$, which is the external field value where the line is observed. This dependence on the polar angle θ roughly takes a squared sinusoidal form. With the reasonable assumption, that NMR intensity is a linear function of the volume fraction, the following formula for the angular dependent intensity of a NMR line of the domain i in GaV_4Se_8 emerges:

$$I_i(\theta) = V_{i,\mathrm{abs}}(A_I \sin^2(\theta) + I_0) \tag{6.13}$$

Here, $V_{i,\mathrm{abs}}$ is a scalar factor proportional to the volume fraction of domain i, while A_I and I_0 are the amplitude and the offset value of the sinusoidal angular dependence, respectively. Regarding the angular dependence of the NMR intensity $I_i(\theta)$, only the term describing the volume of the domain differs between domains, as they share the same angular dependence. Using the spectra shown in Fig. 6.4a) and Eq. 6.13, the intensity curves $I_i(\theta)$ can be determined for each domain i. When scaling the intensity curves onto each other, as shown in Fig. 6.5b), the used scaling factors S_i can be used for the domain quantification. The S_i are defined as

$$I_1(\theta)S_1 = I_2(\theta)S_2 = I_3(\theta)S_3 = I_4(\theta)S_4 = c_0(A_I \sin^2(\theta) + I_0), \tag{6.14}$$

where c_0 is an arbitrary constant. The scaling factor S_i is therefore inverse proportional to $V_{i,\mathrm{abs}}$.

$$V_{i,\mathrm{abs}} = \frac{c_0}{S_i}$$

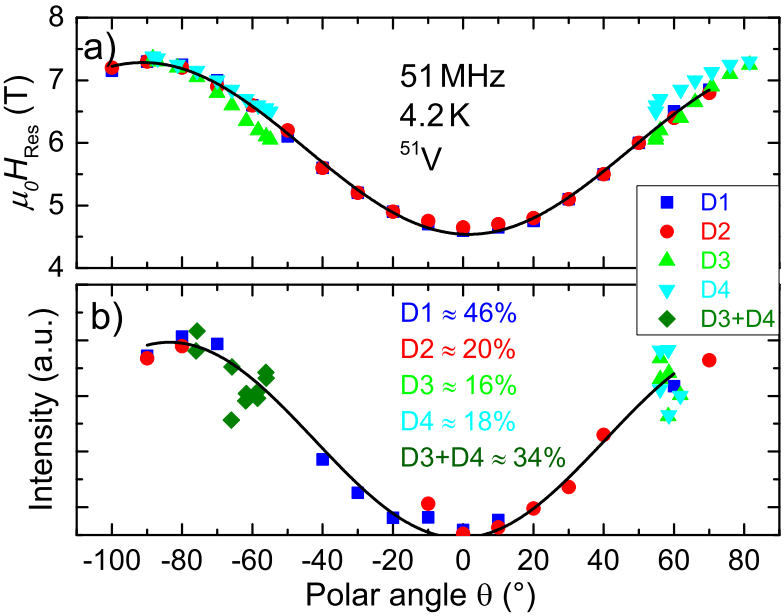

Figure 6.5: a) Dependence of the ^{51}V resonance fields on the angle between the polar axis and the magnetic field (polar angle θ).
b) The absolute intensity of the ^{51}V NMR line corresponding to each domain (scaled to the same value) versus the polar angle. The scaling factor yields information about the domain population. Negative polar angles are used to visibly separate intensity values of lines corresponding to D3+D4 and the individual D3 and D4 domains within the graph.

The volume fractions therefore calculate as:

$$V_i = \frac{V_{i,\mathrm{abs}}}{\sum_j V_{j,\mathrm{abs}}} = \frac{1/S_i}{\sum_j 1/S_j} \tag{6.15}$$

As seen in Fig. 6.5 b), the volume fractions derived from the scaling factors are:

$$\begin{aligned} V(\mathrm{D1}) &= (45.5 \pm 6.8)\% \\ V(\mathrm{D2}) &= (20.6 \pm 2.9)\% \\ V(\mathrm{D3}) &= (15,7 \pm 2.3)\% \\ V(\mathrm{D4}) &= (18.1 \pm 2.7)\% \end{aligned}$$

Note that this method has a rather large error, as the spectra for D3 and D4 do not show a large angular range and are overlapping. This method requires a series of spectra over the whole 180° rotation about the $[1\bar{1}0]$ axis, which additionally

introduces an error due to possible misalignment, as the polar angles θ may be assigned incorrectly. Estimating the error is rather difficult, as it depends on various properties, such as the scaling error, originating from scaling the intensity curves onto each other, which is done manually. An error of about 15% is plausible. However, this result already gives a clear indication that the domain D1 is preferred by the crystal itself, probably due to geometric reasons.

The single spectrum method

This method utilizes the fact that specific field orientations allow the four domains to be measured as separate lines without overlap, as seen in Fig. 6.6. With a previously measured angular dependence of the NMR intensity via the previous method, we can measure the domain population with a single spectrum. The angular dependence of H_{res}, described by a squared sinusoidal function, can be seen in Fig. 6.5 a). The formula then corresponds to:

$$H_{\mathrm{Res}}(\theta) = A_{\mathrm{H}} \sin^2(\theta) + H_{\mathrm{diam}} \tag{6.16}$$

Eliminating the $\sin^2(\theta)$ in Eq. 6.13, reveals the intensity formula based on resonance field:

$$I_i(\mu_0 H_{\mathrm{Res}}) = V_{i,\mathrm{abs}} \left(\frac{A_{\mathrm{I}}}{A_{\mathrm{H}}} \mu_0 (H_{\mathrm{Res}} - H_{\mathrm{diam}}) + I_0 \right) \tag{6.17}$$

In order to utilize this formula, the parameters A_{I},A_{H} and I_0, which are independent of the investigated domain but are instead material parameters, must be determined beforehand via the previous method. To do this, the previously measured domain fractions are inserted into Eq. 6.13. For $\theta = 0°$, I_0 can be directly evaluated via $I_0 = I_i(\theta = 0°)/V_i$. Then A_{I} follows directly from the amplitude of the intensity curves given by 6.13, while A_{H} is a fit parameter of the squared sinusoidal capturing the amplitude of the anisotropy of the hyperfine fields. With all parameters known, the scalar proportional to the domain volume can be calculated:

$$V_{i,\mathrm{abs}} = \frac{I_i(\mu_0 H_{\mathrm{Res}})}{\frac{A_{\mathrm{I}}}{A_{\mathrm{H}}}(H_{i,\mathrm{Res}} - H_{\mathrm{diam}}) + I_0} \tag{6.18}$$

The volume fractions follow directly:

$$V_i = \frac{V_{i,\mathrm{abs}}}{\sum_j V_{j,\mathrm{abs}}} \tag{6.19}$$

In Fig. 6.6, two of the five spectra out of the dataset in Fig 6.5 a) are shown, where four different domains are each visible as NMR lines without overlap. The errors given are the standard deviation of the five different spectra, with an additional

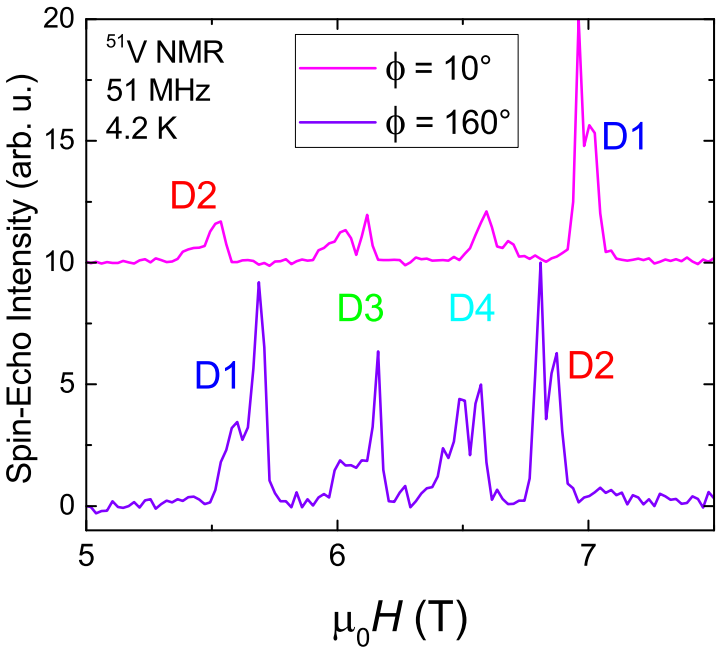

Figure 6.6: Two exemplary ^{51}V spectra, showing the angular dependence of the NMR intensity (taken from Fig. 6.4). Without changing the domain population via heating and recooling through T_{JT}, different intensity ratios are observed for the different lines corresponding to the different domains. The lines corresponding to D1 and D2 switch places for these two spectra, indicating that the NMR intensity is enhanced for lines exposed to larger lineshifts.

estimated 5% via built up errors from the previous method. Using the center of mass of the lines as their $\mu_0 H_{\mathrm{Res}}$, the volume fractions follow from Eq. 6.19.

$$\begin{aligned} V(\mathrm{D1}) &= (42.5 \pm 8.8)\% \\ V(\mathrm{D2}) &= (20.7 \pm 5.5)\% \\ V(\mathrm{D3}) &= (18,9 \pm 5.7)\% \\ V(\mathrm{D4}) &= (17.9 \pm 5.1)\% \end{aligned}$$

The resulting volume fractions are in accordance with the previous method, however a prior measurement of the necessary parameters was needed. This method is not optimal in general due to errors of the previous method building up. The assignment of the polar angle for an arbitrary field direction causes an additional error due to

potential misalignments. When it comes to checking a series of crystals of the same material, for example when looking for the largest initial D1 population in a single crystal, this method would be useful though, as the measurement can be performed quickly due to just one spectrum being recorded.

The 90° spectrum method (preferred)

Instead of eliminating all angular dependences via correction calculations, the measurement itself can also be performed in a way, to have all domains under the same polar angle to begin with. Similar to the already shown "90° method" utilizing ^{71}Ga spectra, the ^{51}V spectra are measured under the same field orientations as the ^{71}Ga nuclei ($[11\bar{2}]$ (D1), [110] (D3+D4) and [112] (D2)). For $\theta = 90°$, according to Eq. 6.13, the intensity of the NMR line becomes:

$$I_i(\theta = 90°) = V_{i,\mathrm{abs}}(A_\mathrm{I} + I_0) \tag{6.20}$$

Therefore, the volume fractions of domain i are calculated as:

$$V_i = \frac{V_{i,\mathrm{abs}}}{\sum_j V_{j,\mathrm{abs}}} = \frac{I_i(\theta = 90°)}{\sum_j I_j(\theta = 90°)} \frac{A_\mathrm{I} + I_0}{A_\mathrm{I} + I_0} = \frac{I_i(\theta = 90°)}{\sum_j I_j(\theta = 90°)} \tag{6.21}$$

By measuring the domains under the same conditions, the intensities can be directly compared with each other. Additionally, no previous determination of the volume fractions are needed to perform the analysis of the spectra and intensities, since no parameters other than the raw intensities are used. This increases the accuracy, as it does not accumulate errors from previous measurements. Due to the equivalence of D3 and D4 under $[1\bar{1}0]$ rotation, only the sum of the two intensities can be observed. In the previous two methods, however, distinguishing the two domains was possible due to a small misalignment separating the lines sufficiently. This method is not strongly affected by misalignments, as the line separation also depends on the anisotropy of the hyperfine coupling. In the case of $\theta = 90°$ the derivative $dH_\mathrm{Res}/d\theta$ vanishes, which causes an invariance of H_Res for small misalignments, while at arbitrary angles, changes in H_Res can be large enough to separate the lines if the derivative and misalignment are sufficiently large. The spectra shown in Fig. 6.7 correspond to the domains D1, D2 and D3+D4. In this dataset from Fig. 6.5 a), an offset of 5° between the shown spectrum for D3+D4 and their 90° position is present, which is adjusted for in the measurements of the next subsection. With the current dataset, however, the resulting domain population is given by:

$$\begin{aligned} V(D1) &= (52.0 \pm 5.2)\% \\ V(D2) &= (23.7 \pm 2.4)\% \\ V(D3 + D4) &= (24.3 \pm 2.4)\% \end{aligned}$$

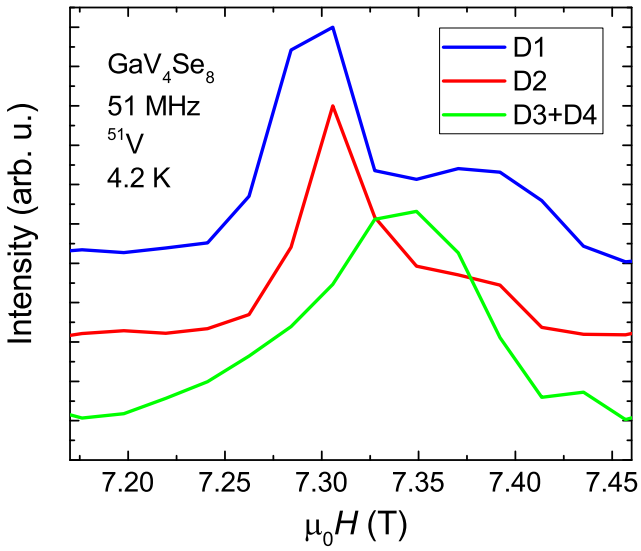

Figure 6.7: Example of three ^{51}V spectra corresponding to the domain D1, D2 and D3+D4 measured in the $\theta = 90°$ position (taken from Fig. 6.4). The relative intensities are being used to calculate the domain population directly.

The discrepancy with respect to the previous measurements is rather small when considering misalignments, angular offsets or accumulating fit errors present in the methods. For this dataset, the error is assumed to be around 10%. The 90° method has successfully been compared with the two shown ^{71}Ga-based methods and showed good agreement for the same crystal in the same cooling run as shown in Tab. 6.1. Therefore the domain population can be reliably measured by NMR, which will be utilized in the following section, as the GaV_4Se_8 crystal will be poled by electric and magnetic fields, while the domain population is monitored via NMR.

Table 6.1: Comparison between the different domain population measurement methods, based on different nuclei

Domain	^{71}Ga polar axis method	^{71}Ga 90° method	^{51}V 90° method
D1	28 %	27 %	27 %
D2	17 %	21 %	21 %
D3+D4	55 %	52 %	52 %

In conclusion, a set of different methods for measuring the population of multiferroic domains in GaV_4Se_8 was shown. The preferred method utilizes ^{51}V spectra, taken at field directions $[11\bar{2}]$(D1), [110](D3+D4) and [112](D2), where the relative intensities of the NMR lines directly correspond to the domain fractions.

6.4 Electric and Magnetic Domain Control

In this subsection, using the "90° method" with ^{51}V nuclei, the domain population is monitored while performing several magnetic and electric poling experiments. The fact that the magnetic easy axis and the polar axis are identical, makes it possible to favour one ferroelectric domain via magnetic fields. The domain with its anisotropy axis parallel to the magnetic field gets favoured in comparison to the other domains. With electric poling, a domain can either be favoured or unfavoured, based on the electric field direction. Since there are no inversion domains in GaV_4Se_8, a suppression of one domain increases the population of the other three, resulting in a multi domain state. The resulting domain populations obtained by NMR in these poling experiments can then be compared with the polarization obtained from pyroelectric current measurements.
The experiments have been performed by applying electric or magnetic fields along the anisotropy axes of certain domains while cooling through the Jahn-Teller transition. At 4.2 K, when the domain wall movement is rigid, the NMR measurements determining the domain population were carried out. The frozen domain wall movement at these temperatures (far away from T_{JT}) is important, since the domain population must not change under the magnetic fields applied by the NMR setup itself [95]. The pyroelectric current measurements, used to compare the NMR results with, were performed afterwards, in a different experimental setup, and therefore were measured in different cooling runs. Nevertheless, the small noise within the set of domain population measurements suggests a good reproducability, and the results are therefore comparable.
The extreme end spectra of the electric poling experiments with electric fields parallel to the polar axis of D1 are shown in Fig. 6.8 a). The voltages were chosen to be rather small, as the crystal is not supposed to undergo an electric breakthrough event. The y-scaling was chosen in a way, that all spectra in the middle column have the same area, while the same scaling factor is also used for the left and right column as well, to show the intensity differences. From the evolution of intensities, a clear indication is given, that D1 is being enhanced by positive electric fields while the other domains are suppressed. The more detailed evolution of the domain population is shown in Fig. 6.8 b), as a linear increase/decrease is obvious for D1,D2 and D3+D4. This is to be expected, as the free energy of a ferroelectric material in an electric field is a linear function of the electric field E [66].

From the domain population obtained by NMR, the unitless polarization P_{UL} can be defined, which is proportional to the bulk polarization by a scaling factor P_0.

$$P_{\mathrm{NMR}} = P_0 P_{\mathrm{UL}} = P_0[V_1 - \cos(71^\circ)(V_2 + V_3 + V_4)] \tag{6.22}$$

P_0 is obtained by comparing pyroelectric current measurements with the equivalent NMR experiment at zero poling field.
When plotting the two polarizations against each other, using the electric poling field as a common parameter, one obtains a linear curve, shown in Fig. 6.8c). The slope, however is not equal to 1, as it would be expected if the same properties are measured. The geometry of the crystal, especially the contacted surfaces with each different surface areas cause an inhomogeneous electric field throughout the crystal, less efficiently poling the outer edges of the crystal. This causes the pyroelectric current measurement to detect a larger polarization than the NMR experiment, as NMR measures the whole crystal, including the outer edges. This is illustrated in Fig. 6.9, where the shape of the crystal and its surfaces are shown.

This interpretation can be checked via magnetic poling experiments. Due to the magnetic field being homogeneous, the difference between measuring the whole sample, or a subsection of it, should not matter, as long as the domains are also distributed homogeneously, which is a reasonable assumption to make. The sample was therefore poled with magnetic fields parallel to the polar axis of D1. The corresponding plot comparing the polarizations obtained by NMR and pyroelectric current is shown in Fig. 6.10 c). GaV_4Se_8 shows easy-plane magnetism for small magnetic fields ($H < 3\,T - 5\,T$), and becomes an easy-axis magnet for larger fields [96, 97]. Therefore, the polarizations show large scattering for small fields, within the easy-plane regime. When considering larger field values only, NMR polarization and the pyroelectric polarization correspond directly to each other with a slope of 1, further establishing the accuracy of the measurement technique presented in this thesis.
In Fig. 6.10 a), the evolving spectra for 0 T, 5 T and 9 T magnetic poling field along the anisotropy axis of D1 are shown for each domain. The resulting volume fractions are shown in Fig. 6.10 b). The domain population shows a quadratic dependence, instead of being linear with the poling field, as the free energy is a quadratic function of H [81], which also causes negative and positive magnetic poling fields to yield the same result. This quadratic poling efficiency is also visible for the poling experiments with the magnetic poling field parallel to the polar axis of D2.

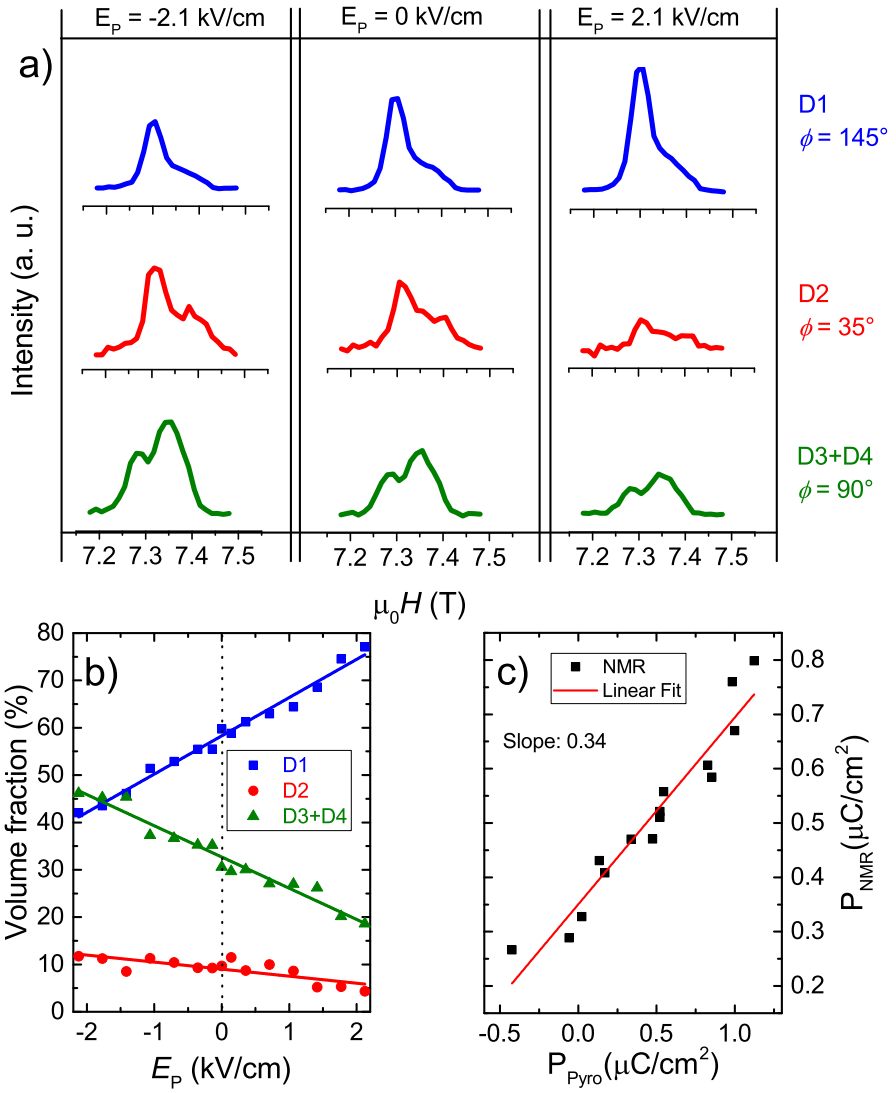

Figure 6.8: a) Table of ^{51}V spectra, under different electric poling fields along the anisotropy axis of D1. The y-axes are scaled in a way to display the middle column spectra each with the same area. The reducing/increasing intensity represents the evolution of the domain population. b) The volume fractions, measured via the "90° method", change linearly with the electric field. c) The resulting polarization obtained by NMR is plotted against the polarization obtained from pyroelectric current measurements.

The already preferred D1 domain population is only reduced by a small amount when poling D2, as most of the domain conversion occurs from D3+D4 towards D2, as seen in Fig. 6.11 b). This suggests that it is harder to depopulate D1 than the other domains, since the poling field has to overcome the previous geometric advantage of

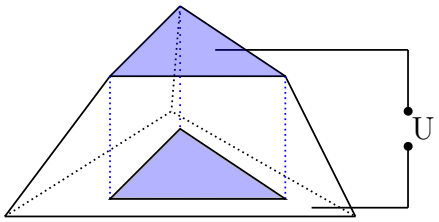

Figure 6.9: Illustration of the measured GaV_4Se_8 crystal. The pyramidal shape causes a discrepancy between the estimated polarization by NMR and the pyroelectric current measurements. NMR measures the whole crystal, including the less efficiently poled side edges, whereas the pyroelectric current method measures the volume defined by the contacted surfaces.

a D1 population. The resulting unitless polarization P_{UL} is shown in Fig. 6.11 c), where P_{UL} is projected on the P2 direction. Since there are no electrical contacts on the (111) surfaces corresponding to D2, which would allow a measurement of the polarization in this direction via pyroelectric currents, P_{UL} is shown alone. It shows a quadratic increase in the polarization until it eventually reaches 0 at around 9 T, where D2 is populated enough to cancel out the other three domains.
With these poling experiments and the subsequent continuous conversion from one type of domain into others, another possibility to check the used quantification method emerges. If the method, using the NMR intensity of domain specific lines to obtain the domain population is valid, then the sum of all intensities should be constant over all experiments, as intensity from one domain is transferred to another. If one domain happens to have a larger intensity than another domain while being populated equally, either due to relaxation effects or potentially other unknown processes, the sum of line intensities of all domains would show a bias towards one domain upon poling, as a higher population on the preferred domain enhances its NMR intensity disproportionately. The sum of intensities for the three poling experiments is constant within the accuracy of the measurement, excluding major unknown correction factors that would have been necessary to include:

$$\begin{aligned} \text{Electric poling; D1}: &\quad \sum_{i=1}^{4} I_i = 24.4 \pm 0.4 \\ \text{Magnetic poling; D1}: &\quad \sum_{i=1}^{4} I_i = 25.2 \pm 0.4 \\ \text{Magnetic poling; D2}: &\quad \sum_{i=1}^{4} I_i = 24.6 \pm 0.5 \end{aligned} \tag{6.23}$$

The standard deviation is about 1% and no bias towards any domain was observed, regarding NMR line intensity.

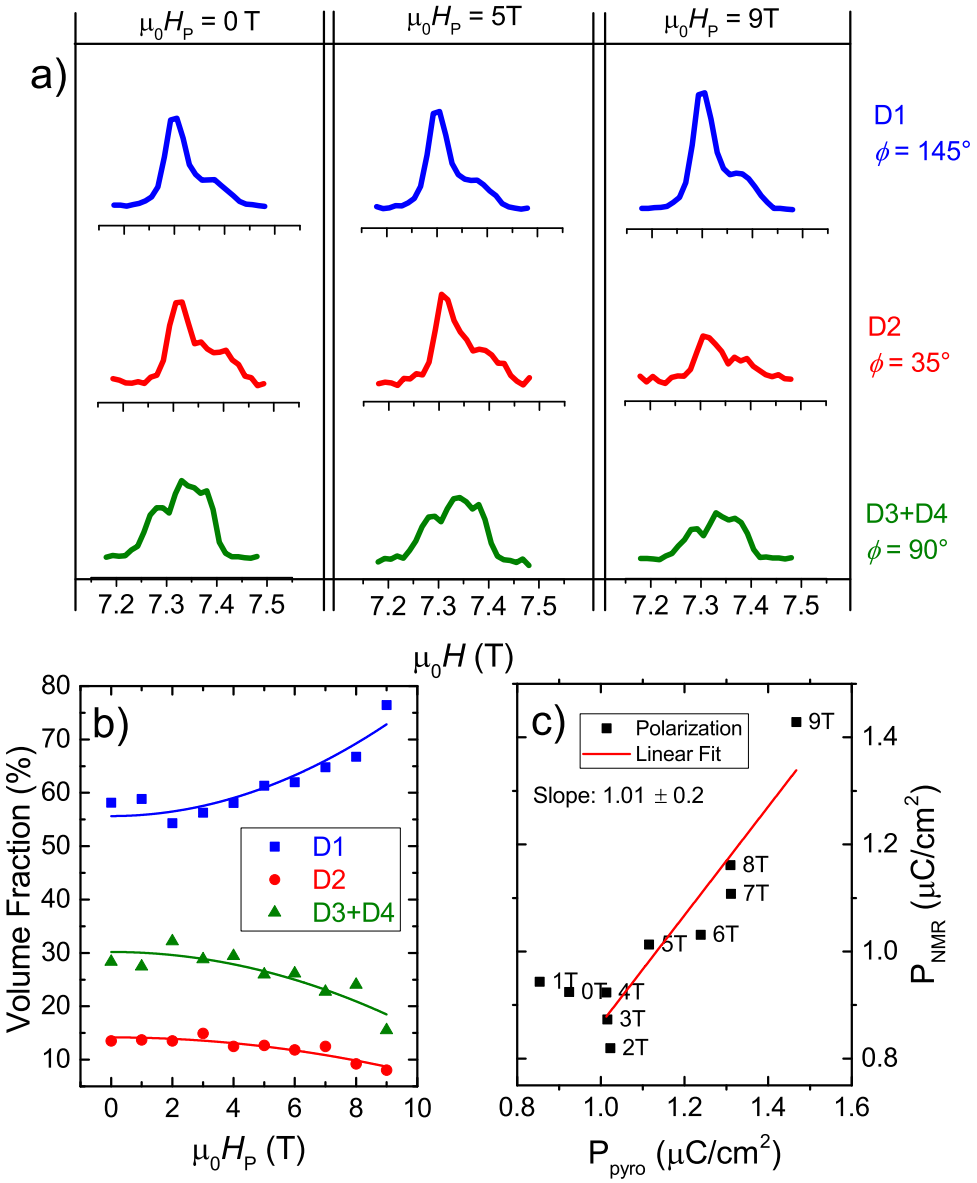

Figure 6.10: a) Table of ^{51}V spectra under different magnetic poling fields along the anisotropy axis of D1. The y axes are scaled in a way to display the middle column spectra each with the same area. The reducing/increasing intensity represents the evolution of the domain population. b) The volume fractions, measured via the "90° method", change quadratically with the magnetic field. c) The resulting polarization obtained by NMR is plotted against the polarization obtained from pyroelectric current measurements.

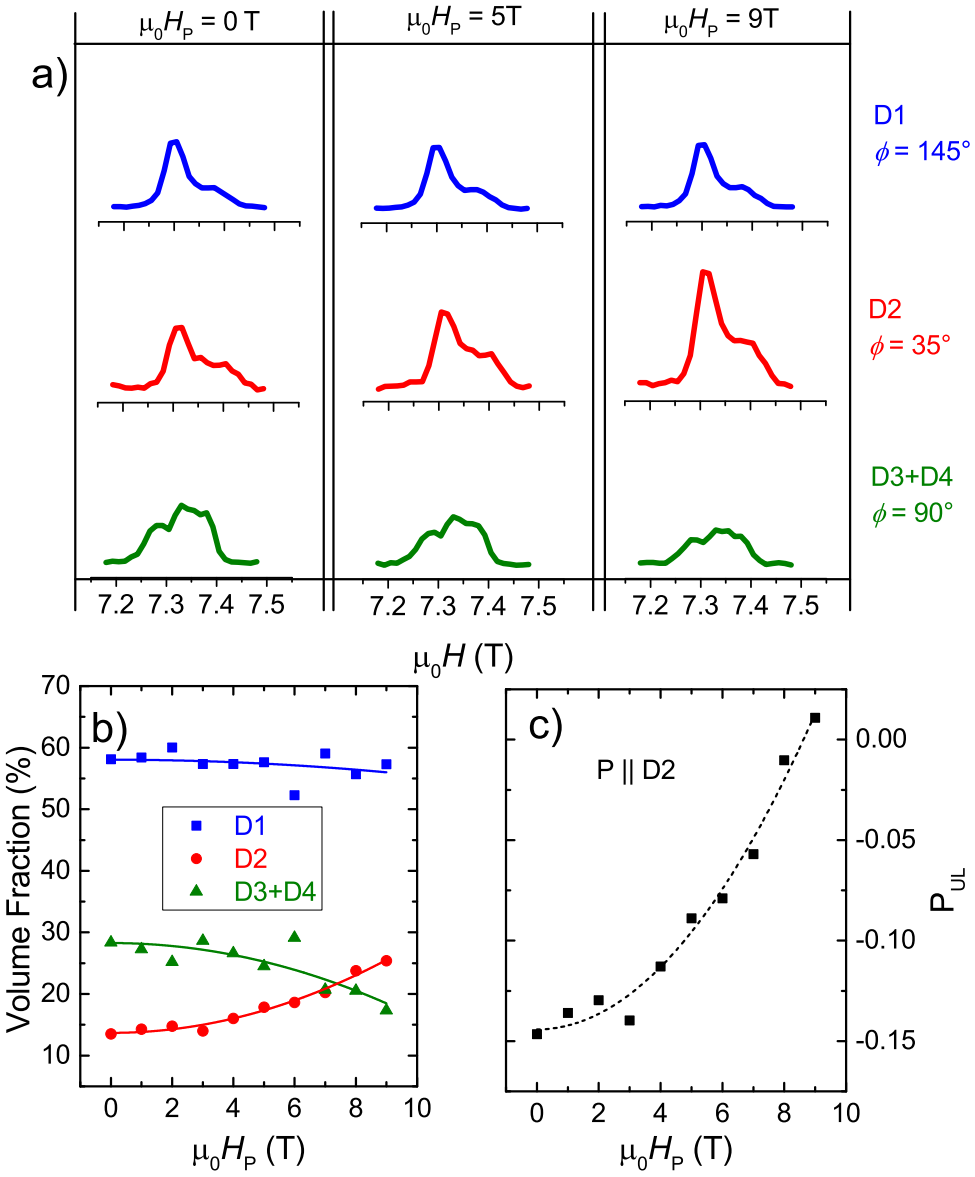

Figure 6.11: a) Table of ^{51}V spectra under different magnetic poling fields along the anisotropy axis of D2. The y-axes are scaled in a way to display the middle column spectra each with the same area. The reducing/increasing intensity represents the evolution of the domain population. b) The volume fractions, measured via the "90° method", change quadratically with the magnetic field. c) The resulting unitless polarization obtained by NMR is shown without pyroelectric current reference, as this data has not been measured.

In conclusion, a domain quantification technique based on ^{51}V NMR was investigated, measuring the domain population of multiferroic domains upon applying different poling electric and magnetic fields. As the poling experiments along the polar axis of D2 direction shows, the main benefit of this measurement technique, other than quantifying the domain population itself, is that NMR measurements can be performed without electrical contacts. Crystals without accessable surfaces, or chemical instability towards certain solvents, could have their (unitless) polarization measured by NMR, if the necessary criteria are met. The NMR active nuclei in the material must be distinguishable via local order parameters, such as the magnetization via the hyperfine coupling or the polarization via the quadrupolar splitting. This rather broad set of criteria makes this method applicable for a possibly wide range of ferromagnets, ferroelectrics or multiferroics.

Chapter 7

Charge and Spin Distribution over the V_4S_4 Cluster

7.1 Electric Field Gradients in GaV_4S_8

In the previous chapters we showed that the ferroelectric and ferromagnetic order parameters can be detected via the quadrupolar splitting and the hyperfine shift, respectively, in GaV_4Se_8 and GaV_4S_8. In addition, this also allowed us to determine the volume fractions of different domains. Here we demonstrate that the full-depth analysis of the NMR spectra and the quadrupole splitting they exhibit can also be exploited to determine the electron distribution over the V_4S_4 clusters in the ferromagnetic state of GaV_4S_8. This chapter mainly reflects the content of Prinz-Zwick et al. [98].

7.1.1 ^{51}V Site Identification

In order to investigate the quadrupolar interaction of the ^{51}V sites, it is important to know the exact orientation of the external magnetic field with respect to the principle axis of the EFG tensor. As compared to the case of ^{71}Ga, the analysis of the quadrupolar splitting is more complex due to the following reasons:

1. ^{51}V is not a unique site in the unit cell
2. In the polar rhombohedral state, there are two different ^{51}V sites (the unique corner of the V_4 tetrahedron and the other three basal corners), each characterized by different EFGs
3. the site symmetry is different for the two cases of ^{71}Ga and ^{51}V

4. the quadrupolar splitting for the ^{51}V nuclei in GaV_4S_8 is smaller, thus harder to resolve (which is the reason why spin-echo modulations are used in order to investigate the quadrupolar interaction)

This requires a detailed measurement of the NMR spectra and the quadrupolar patterns, obtained via spin-echo modulations in T_2 decay experiments described in section 2.3.2. These spectra and spin-echo modulations are measured as a function of magnetic field orientation with a $[1\bar{1}0]$ field rotation axis, similar to the experiments shown in Fig. 6.4. The angle θ between the anisotropy axis and the magnetic field

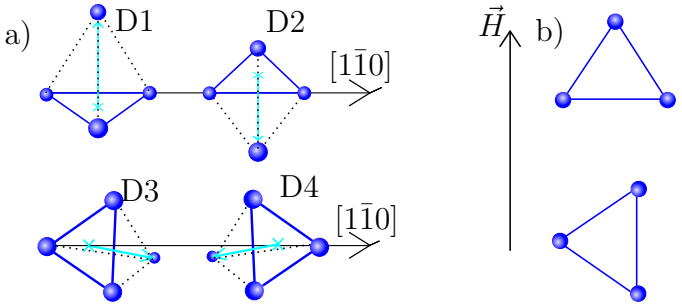

Figure 7.1: a) Orientation of V_4 tetrahedra from different domains with respect to the $[1\bar{1}0]$ rotation axis. b) Illustration of the three bottom corners under the angle $\theta = 90°$ between the magnetic field and the polar axis. In the case of D1,D2 (top) and D3,D4 (bottom), the configurations differ from each other, hinting towards different quadrupolar interactions.

mainly determines the hyperfine shift, therefore lines corresponding to different domains can be on top of each other for certain field directions. For the analysis of the spin echo-modulations, it is important that the analysed NMR lines consist of exactly one domain, as different domains subjected to the same hyperfine fields can have different quadrupolar patterns. This is illustrated in Fig. 7.1 a), where the four different domains are depicted via representative V_4 tetrahedra and a $[1\bar{1}0]$ field rotation axis. The example for a $\theta = 90°$ orientation for representatives of D1/D2 (top) and D3/D4(bottom) in Fig. 7.1 b) shows the different alignments and possible different quadrupolar splittings. The threefold symmetry of the basal plane and the twofold site symmetry suggest that the two configurations are unequal with respect to the quadrupolar patterns. This is why the spectral analysis must and will be focused on exactly one domain in order to have a consistent result. In Fig. 7.2 electric and magnetic field poling has been used to bring the crystal close to a mono-domain state, to increase the intensity of the observed lines and reduce possible overlaps with lines of other domains. Using electric and magnetic field poling favouring the D1 domain, a doubling in intensity has been achieved, speaking for the enhanced population of the D1 domain. This spectrum has been recorded with the external magnetic field parallel to the [111] direction, where the hyperfine fields are the small-

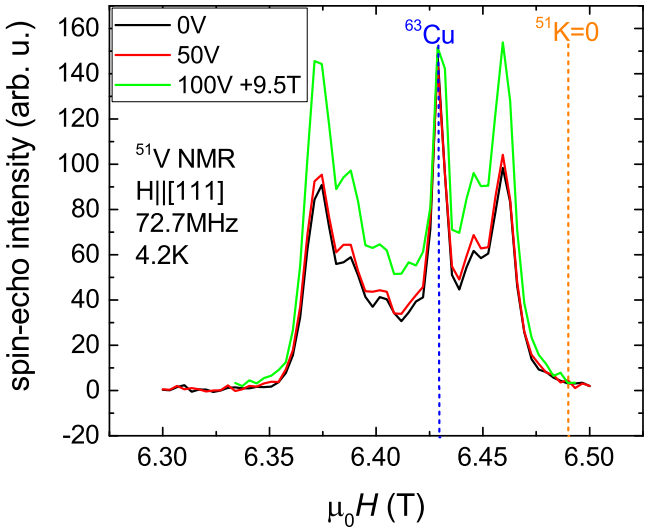

Figure 7.2: ^{51}V spectra corresponding to D1 under electric and magnetic field poling, achieving a near mono-domain state. The seven lines due to quadrupolar splitting are well visible, with the central line having the smallest intensity. Due to the magnetic magnetic field being parallel to the [111] axis, the ^{51}V spectrum overlaps with the spurious ^{63}Cu signal originating from the pickup coil of the experimental setup. It has no further influence on the analysis of the ^{51}V spectra.

est, i.e. the NMR line is close to the diamagnetic position $^{51}K = 0$. With ^{51}V having a nuclear spin of 7/2, a total of seven lines are expected for a single spectrum, which is well observed in this spectrum. The ^{63}Cu line, originating from the copper coil around the sample, unfortunately overlaps with the ^{51}V spectrum, being located near the central line. Poling the crystal into a mono-domain state helped to reduce the relative intensity of the parasitic line, but it is not possible to suppress the line to a non visible degree without replacing the copper coil with silver (which was done in later experiments). The ^{63}Cu line is independent of the orientation of the magnetic field, which means that it will not interrupt any other measurements as soon as we rotate the magnetic field away from the [111] axis. Changing the frequency to a higher value would, in principle, be an option to separate the two lines, but this is not possible due to technical limitations as we already reach the maximal field of the magnet (9-9.5 T) at larger θ angles for this frequency ($\nu = 72.7$ MHz).
Measurements of the spin-echo modulation will not be influenced by this copper line, since no quadrupolar patterns can arise from elementary copper due to the cubic fcc crystal structure and the subsequent absence of electric field gradients.
In the polar rhombohedral phase, there are two different ^{51}V sites with different site

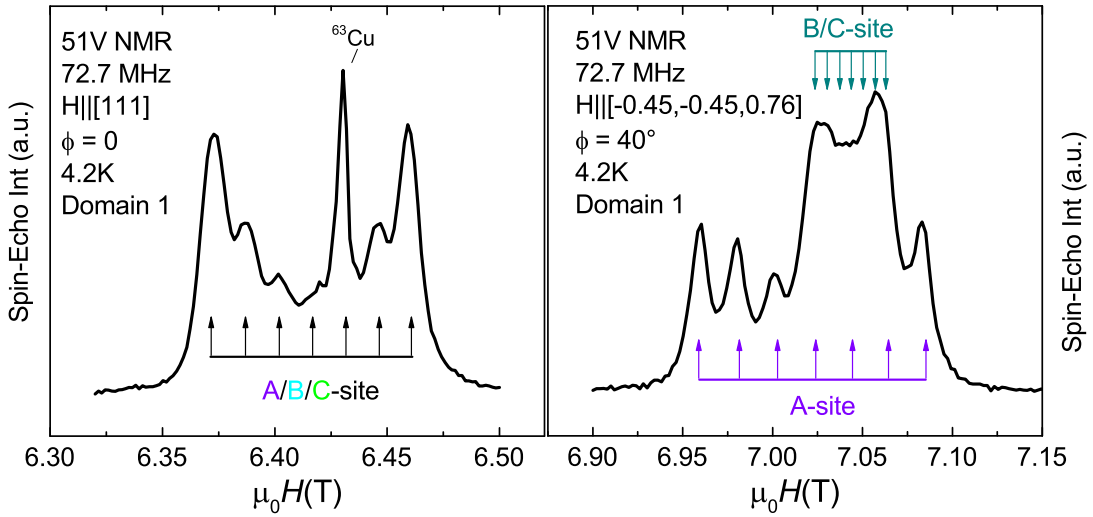

Figure 7.3: Left: ^{51}V spectrum for $\vec{H} \parallel [111]$, where only one type of quadrupolar splitting is observed.
Right: Spectrum after rotation shows inequivalent splittings, leading to the conclusion that the NMR lines originate from base triangle of the elongated V_4 tetrahedron.

symmetries. The unique corner (U site) shows a threefold symmetry, as the bottom corner sites (A/B/C sites) only show a twofold site symmetry, each rotated by 120° with respect to each other. At arbitrary field directions, this can cause differences in quadrupolar splitting for the bottom A/B/C sites, although being crystallographically equivalent. For magnetic fields parallel to the [111] direction though, they are equivalent. Due to the unequal crystallographic positions, different EFGs are expected for the U site and the A/B/C sites. Which sites are probed by the NMR experiments can be determined by comparing two spectra at different field directions. Two spectra are shown in Fig. 7.3, where the shape of the ^{51}V lines is observed under field rotation about the $[1\bar{1}0]$ axis. In the spectrum in the left panel, the field direction is parallel to the polar axis of the investigated domain (D1). Since seven lines in total are expected for a ^{51}V nucleus and are in fact observed, only one type of ^{51}V site is being measured in this very spectrum. An overlap of all four sites is unlikely, since the EFGs of the U site and the bottom sites are different and would cause 14 lines in total to be observed. Therefore, the spectrum either probes the U site alone or the A/B/C sites of the vanadium tetrahedron. If the spectrum on the left hand side corresponded to the U site, then a rotation of the magnetic field would result in an increasing or decreasing splitting of the quadrupolar satellite lines. But the spectrum in the right panel of Fig. 7.3 shows a separation into two branches, one with converging and one with diverging satellites, which reveals that the ^{51}V sites being investigated here are the A, B and C sites of the V_4 unit.

Therefore, spectra which belong to the U site have not been observed yet. There are several possible reasons for this.

- The line of the U site is out of the range of the magnet due to much stronger internal fields
- A fast T_2 relaxation rate would cause the line to vanish
- The EFG is too small to produce a line splitting and the unique corner signal is hidden within the lines of the bottom corners
- A very long T_1 relaxation time would reduce the ability of the nucleus to relax back after a pulse sequence, and would therefore disappear after consecutive pulses
- The line shows no strong anisotropy, and is hidden under a stationary line, produced by either an artifact nucleus or one of the Ga isotopes

More than one of these reasons can occur simultaneously, making it hard to predict the actual reason for the non-observation. So from now on, the focus will be on the three bottom corner sites.

From Fig. 7.3, it is apparent that the quadrupolar patterns can be studied well by measuring the full angular dependence of the splitting. For small splittings, however, the individual satellite lines are not resolved (see B/C sites in the right panel of Fig. 7.3). Therefore, the property being measured for determining the quadrupolar interaction is the spin-echo modulation frequency in the T_2 decay, which has a higher resolution, since the resolution is only limited by the usable pulse widths and is independent of natural line widths.

In conclusion, it was determined that the observed NMR nuclei in the V_4S_4 cluster are the three bottom sites of the elongated V_4 tetrahedron. This was determined by the specific angular dependence of the spectra, which are consistent with quadrupolar satellites originating from the three base sites.

7.1.2 Angular Dependence of quadrupolar Spin-Echo Modulations

In this subsection, the measurement and discussion of the angular dependence of the spin-echo modulations, obtained from T_2 decay measurements, will be presented. These spin-echo modulations give detailed information about the quadrupolar splitting without the need for resolving individual satellite lines, which is especially useful

for small splittings. The spin-echo modulation frequency a is correlates linearly with the field difference due to quadrupolar splitting:

$$a = \frac{3\pi eQ}{2hI(2I-1)} \frac{\left\langle \vec{H} \middle| V_{\mathrm{ij}} \middle| \vec{H} \right\rangle}{|H|^2} = \frac{^{51}\gamma}{\pi} \Delta H_{\mathrm{Q}} \frac{\left\langle \vec{H} \middle| V_{\mathrm{ij}} \middle| \vec{H} \right\rangle}{|H|^2} \tag{7.1}$$

In the experiment, a rotation about a [110] axis separates the three bottom corners into two distinct sites, which are only equal for $\vec{H} \parallel [111]$. The two sites connected by the rotation axis are the B/C site, while the opposing corner is the A site. In Fig. 7.4, the splitting into two quadrupolar branches can be seen locally, via the different quadrupolar splittings illustrated by the different Θ_1 and Θ_2 angles upon rotation.

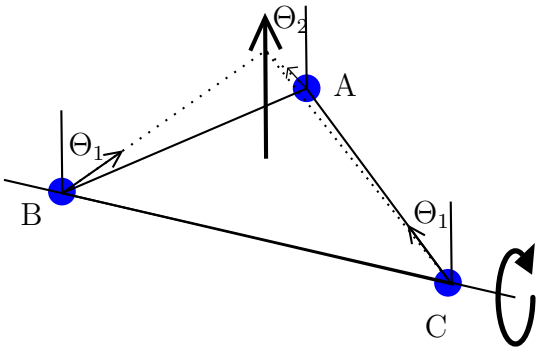

Figure 7.4: Splitting of the base triangle into two branches due to rotation around a [110] axis. The different angles Θ_1 and Θ_2 represent their different quadrupolar patterns expected in arbitrary rotation angles. Θ loosely describes the orientation of the EFG to the external magnetic field $\mu_0 H$

A waterfall plot of the ^{51}V spectra under field rotation is shown in Fig. 7.5, where the field axes $\mu_0 H$ of the spectra are shifted to have the same resonance field as the spectra with $\vec{H} \parallel [111]$, neglecting the hyperfine shifts for the purpose of spectra comparison. These spectra are the basis for the spin-echo modulation measurements, discussed in the following.

At first, it is important to see, how the modulation frequency in the T_2 decay looks like for the different satellites in the [111] orientation. Fig. 7.6 shows, that the oscillation frequency is the same for all of the seven lines (the center line and the three pairs of satellites) within the experimental error. Please recall that the three ^{51}V nuclei at the base triangle have identical NMR spectra for this field orientation. This is an important consequence to the analysis of the angular dependent measurements. If two distinct peaks, observed in a field-swept spectrum recorded at arbitrary orientation of the external field, are characterized by different oscillation frequencies, then they must originate from non-equivalent ^{51}V sites. For a $[1\bar{1}0]$ field rotation axis, the sites B and C stay equivalent, while the A site would exhibit different quadrupolar

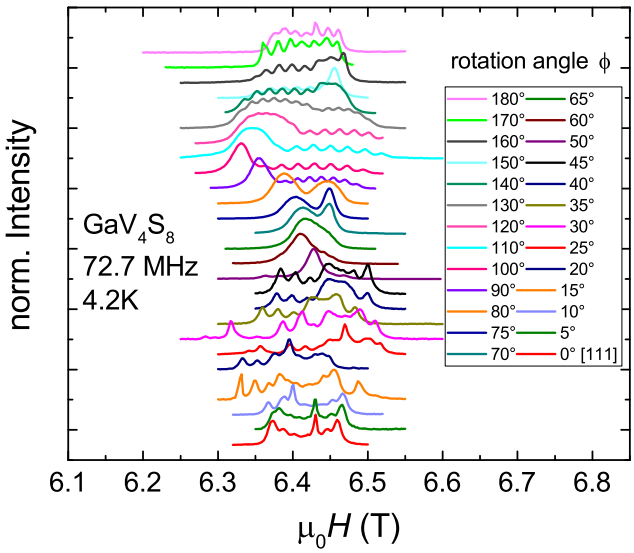

Figure 7.5: Angular dependence of ^{51}V spectra under field rotation about the $[1\bar{1}0]$ axis. The hyperfine shifts are neglected in this plot, shifting all spectra to the same resonance field as for $\vec{H} \parallel [111]$. The A and B/C sites each exhibit different quadrupolar splitting and slightly different hyperfine fields.

splitting throughout the field rotations. However, a field rotation about other axes (for example the $[11\bar{2}]$ axis) would result in three different quadrupolar splittings for the A, B and C site. Recording these spin-echo modulation measurements for most of the satellite lines during a 180° rotation yields the angular dependence of the quadrupolar oscillation frequency for the A- and B/C sites.
A series of example oscillations are shown in Fig. 7.7, where T_2 decay curves are displayed under different field orientations, showing a variety of frequencies and amplitudes. The panels a) and b) each show the T_2 decays for the A and B/C sites, respectively, where the magnetic field points along the $[11\bar{2}]$ ($\phi = 90°$) direction. The amplitudes are comparable, whereas the frequencies differ by a factor of 10. In panel c) an overlap between the A and B/C sites is shown, each having similar frequencies. The fitting was performed manually, meaning the parameters of the formula were adjusted manually until satisfactory accordance with the experiment was reached. This was done in order extract only the oscillation coming from the dominant site alone. Panel d) shows one of the cases, where the oscillation frequency was very slow and had a small amplitude, making the fitting process rather inaccurate. Although a bump in the curve is visible, corresponding to a maximum in the oscillation, a full period is not observed in the data. Slower oscillations are not included in the final dataset. From the comparison between panel e) and a), it is clear that there is a

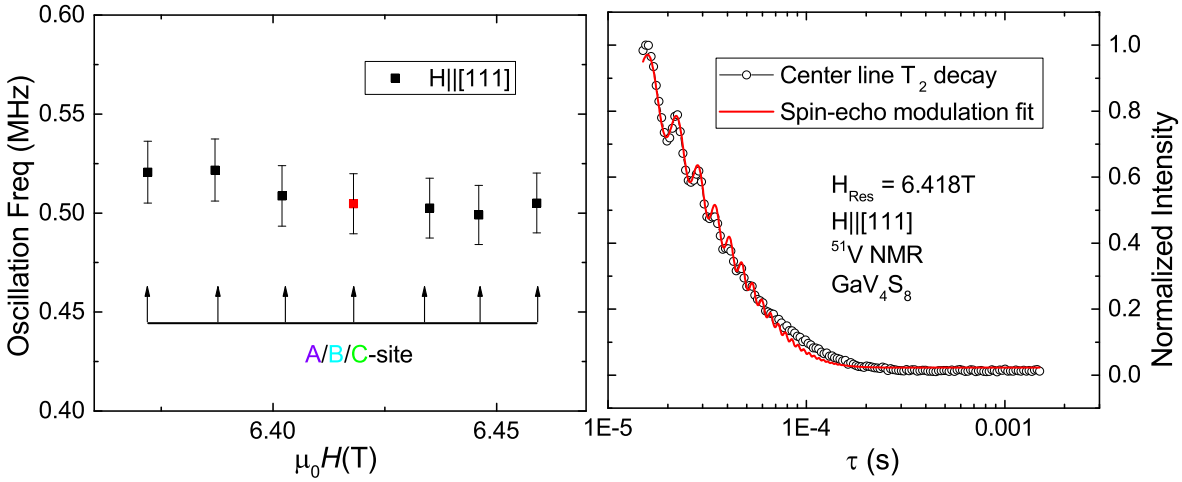

Figure 7.6: Left: Oscillation frequencies for the satellite lines in $\vec{H} \parallel [111]$ configuration. Assuming a 3% error in the fitting/measurement process, all satellite lines have the same frequency within the accuracy of the experiment.
Right: Example of a T_2 decay measurement, which yields the oscillation frequency of the spin-echo modulation. The T_2-decay curve for the center line is shown.

large range of amplitudes of the oscillations which are independent of the frequency and site. The largest observed amplitude is shown in panel f).

In Fig. 7.8 a), all obtained oscillation frequencies are plotted versus the rotation angle ϕ. Since the fitted values for oscillation frequencies are positive by definition, all of the plotted frequency values are positive. In principle, the oscillation frequency a as shown in Eq. 7.1 can have negative values based on the field direction and the EFG tensor. This is taken into account by changing the sign of the frequency values after the graph passes through the x axis at an angle. This reveals a waveform pattern for the oscillation frequency, shown in Fig. 7.8 b). Note that the two branches corresponding to the A and the B/C sites are well visible, however not yet assigned to the respective sites.
At around $\phi = 50°$ to $\phi = 70°$, the quadrupolar interaction becomes rather weak, resulting in slow oscillation frequencies. The fitting for these oscillations is very difficult, as shown in Fig. 7.7 d), which causes the large scattering in Fig. 7.8 a). The frequencies obtained from satellite lines of the same site have been averaged to obtain a single data point for each site, which results in the graph shown in Fig. 7.8b). Fits with high potential errors are removed from the dataset, leaving a short angular window behind, without any data points between $\phi = 50°$ and $\phi = 70°$.

The two different branches originating from the two different A and B/C sites are

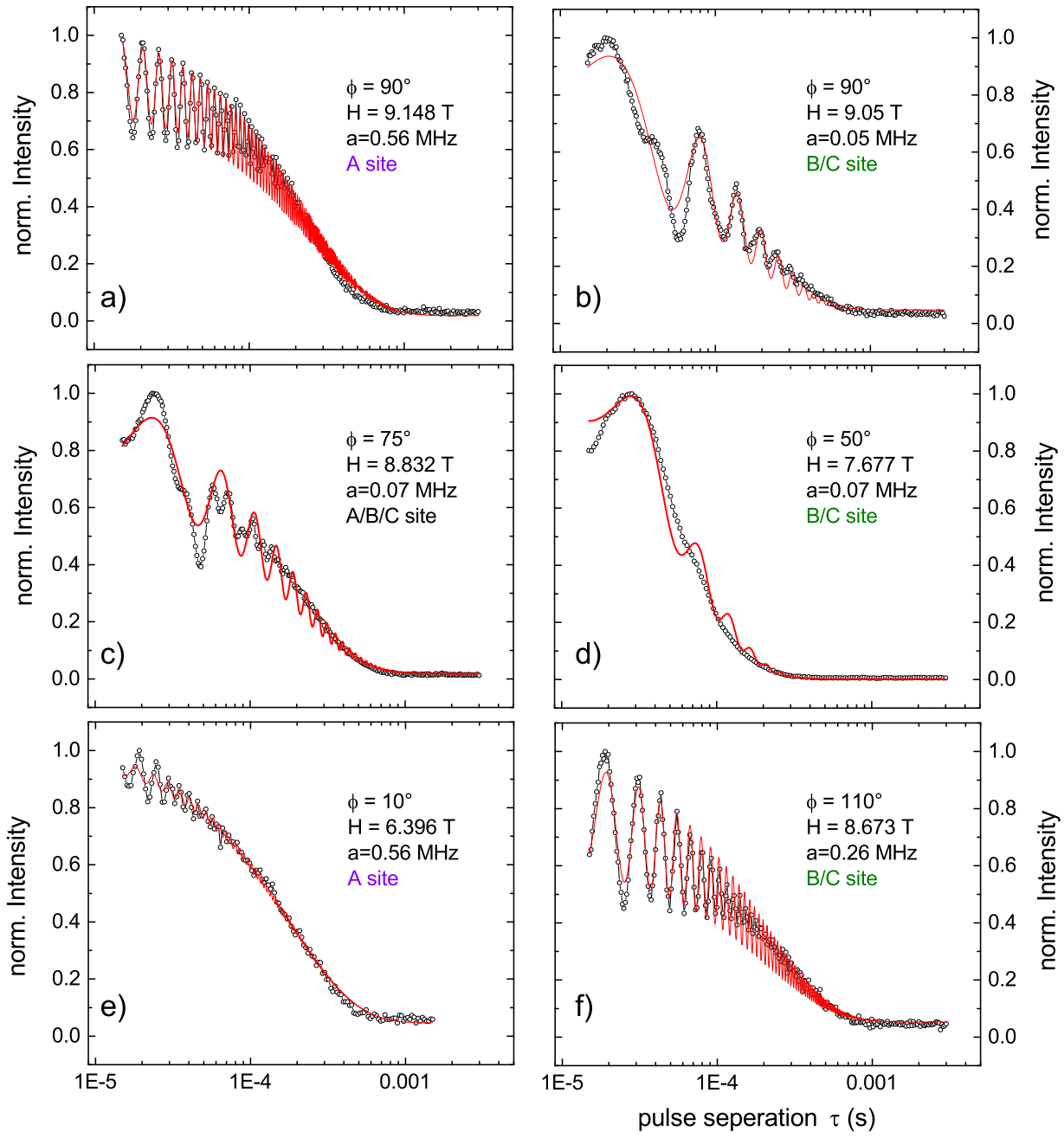

Figure 7.7: Examples for T_2 decay curves showing quadrupolar oscillations. Panels a)-b) show the curves corresponding to the A and B/C sites for the $\phi = 90°$ spectra. c) and d) shows examples of where the fitting was not optimal. e) and f) show the strongest differences in amplitude over the 180° range.

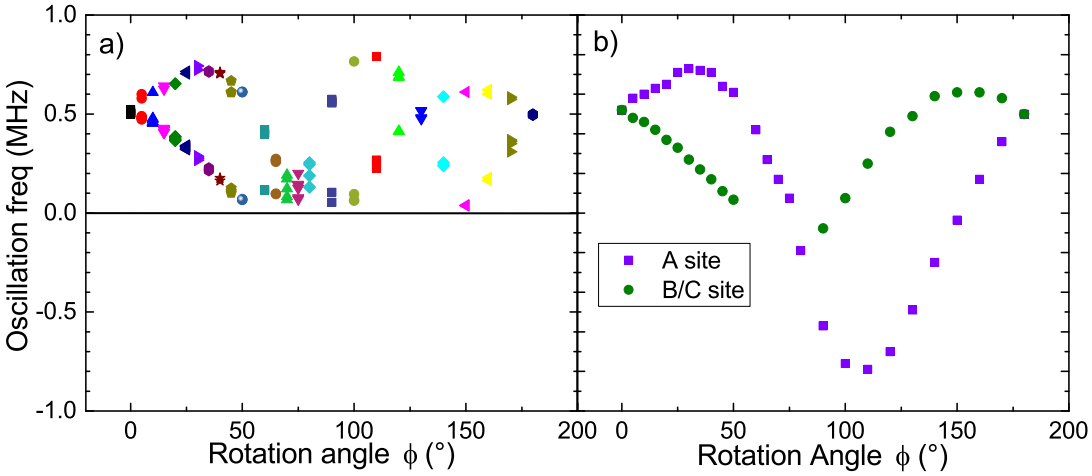

Figure 7.8: Left: Raw data of all oscillation frequencies obtained from all T_2 measurements over the 180° rotation. By definition, all frequencies are positive, hence non differentiable points on the $y = 0$ axis are treated as zero crossings, and one side of the curves is reflected at the $y = 0$ axis.
Right: Reflected data points have been assigned to negative values, and the axis and corner sites have been identified by their individual curves. Data points from measurements, that could not be sufficiently fitted, have been omitted.

distinguishable via their orientation with respect to the rotation axis of the magnetic field. Since the mirror plane of the A site is within the field rotation plane, it spans the largest variation of angles between the external field and the EFG basis, when considering two eigenvectors of the EFG to be within the mirror plane. This results in a larger amplitude when considering spin-echo modulation frequencies, therefore the curve shown in 7.8 b) using purple square symbols corresponds to the A site, the other one to the B/C site.
Since only two branches appeared, this is an additional indication, that in fact, only the three bottom sites of the V_4 cluster are being observed by NMR, and no signal is observed from the ^{51}V nucleus of the unique corner of the distorted tetrahedron.
In addition to the oscillation frequency, one can obtain the actual values for the T_2 relaxation as one parameter of the fit. Since the value of T_2 can depend on the satellite line being observed, it is crucial, when comparing T_2 values between different angles, to always use the same line type. Therefore the center line of the A site has been used as the reference line, since it is rather easy to identify, as the quadrupolar splitting has the largest amplitude. Therefore one can find the center line position by taking the half distance between the outermost satellites. In Fig. 7.9, the angular dependence of T_2 is shown for the A site center line. The relatively large scattering is explained by the complicated form of the T_2 decay, exhibiting strong

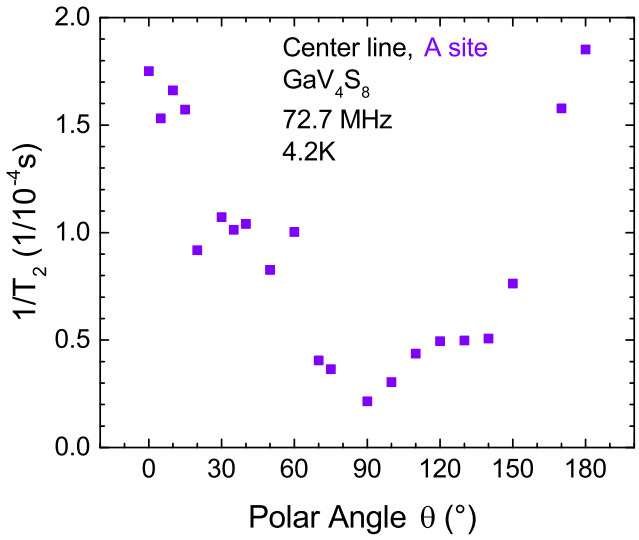

Figure 7.9: Angular dependence of $1/T_2$, obtained from the spin-echo modulation fits for the center line of the A site. A maximum is reached for $\vec{H} \parallel [111] (\theta = 0°, 180°)$, with a minimum at $\theta = 90°$. Larger $1/T_2$ relaxation rates reduce the NMR intensity.

oscillations. In the fitting process, the main focus is on the oscillation frequency, while differences in T_2 only play a minor role. False assignments of the center line of the A site are also possible in some spectra, also explaining the relatively large scattering. Nevertheless, a clear pattern is visible, which appears to have a similar $\sin^2\theta$ shape as the angular dependence of the resonance field. T_2 has its shortest value, meaning the fastest relaxation rate, when the magnetic field is parallel to the [111] axis. The larger the internal fields, the slower the T_2 relaxation becomes due to a yet unknown mechanism. This is a good explanation for the angular dependence of the spin-echo intensity, shown in section 6.3 in the case of GaV_4Se_8.

In conclusion the angular dependence of spin-echo modulations were recorded for the A and B/C sites. The oscillation frequency is a linear function of the quadrupolar splitting, and therefore provides information about the EFG, which will be determined in the following section.

7.1.3 Analysis of the Local Electric Field Gradients

In case we know the elements of the EFG tensor, we can calculate the expected oscillation frequency for a given magnetic field direction using Eq. 2.84. Conversely, if the quadrupolar splitting is determined as a function of the field orientation, one may be able to determine the EFG tensor based on NMR data. Since the local surroundings of the three V sites at the regular triangular base of the distorted V_4 tetrahedron are more complex than for Ga, the site symmetry is lower with merely one mirror plane per site. Correspondingly, an axial symmetric EFG may not properly describe these three sites. In order to reconstruct the EFG from the measured spin-echo modulations, it is important to determine the minimum number of independent elements in the EFG tensor. First, we enter the local coordinate system, instead of the crystallographic coordinates.

$$\vec{x} = \frac{1}{\sqrt{2}}\begin{pmatrix}1\\-1\\0\end{pmatrix} \quad \vec{y} = \frac{1}{\sqrt{6}}\begin{pmatrix}1\\1\\-2\end{pmatrix} \quad \vec{y} = \frac{1}{\sqrt{3}}\begin{pmatrix}1\\1\\1\end{pmatrix} \tag{7.2}$$

The rotation axis of the magnetic field in the previous experiment, and the normal vector of the mirror plane is the new $\vec{x}$ axis. The $\vec{z}$ axis is the polar [111] axis, while the $\vec{y}$ axis points from the A site towards the $\vec{x}$ axis. This coordinate system will be referred to as the natural base.
The form of the EFG tensor, i.e. is dictated by the site symmetry at the corresponding nucleus. Explicitly having a mirror plane perpendicular to $\vec{x}$, and the three sites having the same EFG but rotated by 120°. For the crystal being mirrored by the $(1, 0, 0)$ plane (natural base coordinate system), the EFG must therefore be invariant under a mirror operation:

$$\begin{pmatrix}-1&0&0\\0&1&0\\0&0&1\end{pmatrix}\begin{pmatrix}V_{xx}&V_{xy}&V_{xz}\\V_{xy}&V_{yy}&V_{yz}\\V_{xz}&V_{yz}&V_{zz}\end{pmatrix}\begin{pmatrix}-1&0&0\\0&1&0\\0&0&1\end{pmatrix} =$$

$$\begin{pmatrix}V_{xx}&-V_{xy}&-V_{xz}\\-V_{xy}&V_{yy}&V_{yz}\\-V_{xz}&V_{yz}&V_{zz}\end{pmatrix} \stackrel{!}{=} \begin{pmatrix}V_{xx}&V_{xy}&V_{xz}\\V_{xy}&V_{yy}&V_{yz}\\V_{xz}&V_{yz}&V_{zz}\end{pmatrix} \tag{7.3}$$

$$\Rightarrow V_{xy} = V_{xz} = V_{yx} = V_{zx} = 0 \tag{7.4}$$

And therefore the shape of the EFG in the natural base becomes:

$$V_{ij} = \begin{pmatrix}\tilde{V}_{xx}&0&0\\0&V_{yy}&V_{yz}\\0&V_{yz}&V_{zz}\end{pmatrix} \tag{7.5}$$

While $\tilde{V}_{xx}$ is the first eigenvalue. One of its eigenvectors is therefore given by $\vec{E}_x = (1,0,0)$.
When written in its eigenbase, the EFG becomes diagonal:

$$\begin{pmatrix} 1 & y_1 & z_1 \\ 0 & y_2 & z_2 \\ 0 & y_3 & z_3 \end{pmatrix}^{-1} \begin{pmatrix} \tilde{V}_{xx} & 0 & 0 \\ 0 & V_{yy} & V_{yz} \\ 0 & V_{yz} & V_{zz} \end{pmatrix} \begin{pmatrix} 1 & y_1 & z_1 \\ 0 & y_2 & z_2 \\ 0 & y_3 & z_3 \end{pmatrix} = \begin{pmatrix} \tilde{V}_{xx} & 0 & 0 \\ 0 & \tilde{V}_{yy} & 0 \\ 0 & 0 & \tilde{V}_{zz} \end{pmatrix} \tag{7.6}$$

The tilde indicates that these are the actual eigenvalues of the EFG instead of matrix elements. The eigenvectors of the EFG make up a orthonormal base, and with $\vec{E}_x = (1,0,0)$ already known, the remaining two eigenvectors must be within the mirror plane perpendicular to $\vec{E}_x$. The eigenvectors $\vec{E}_y$ and $\vec{E}_z$ would not necessarily be parallel to the y and z axes, but instead span an angle α with them.
This reduces the amount of parameters, since the whole basis system can be described by a single angle α.

$$\begin{pmatrix} 1 & 0 & 0 \\ 0 & \cos(\alpha) & -\sin(\alpha) \\ 0 & \sin(\alpha) & \cos(\alpha) \end{pmatrix} \begin{pmatrix} y_1 \\ y_2 \\ y_3 \end{pmatrix} = \begin{pmatrix} 0 \\ 1 \\ 0 \end{pmatrix}$$

$$\begin{pmatrix} 1 & 0 & 0 \\ 0 & \cos(\alpha) & -\sin(\alpha) \\ 0 & \sin(\alpha) & \cos(\alpha) \end{pmatrix} \begin{pmatrix} z_1 \\ z_2 \\ z_3 \end{pmatrix} = \begin{pmatrix} 0 \\ 0 \\ 1 \end{pmatrix} \tag{7.7}$$

Since the basis of the EFG can easily be described by one parameter α, the number of free parameters so far is 4, with one value for each eigenvalue $\tilde{V}_{xx}$,$\tilde{V}_{yy}$ and $\tilde{V}_{zz}$ and α defining its base. The diagonal form of the EFG, however, can be written in a more simplified way, by including the Laplace law $\Delta V = 0$ and introducing the asymmetry parameter η for the EFG:

$$\eta = \frac{\tilde{V}_{xx} - \tilde{V}_{yy}}{\tilde{V}_{zz}} \tag{7.8}$$

$$\begin{pmatrix} \tilde{V}_{xx} & 0 & 0 \\ 0 & \tilde{V}_{yy} & 0 \\ 0 & 0 & \tilde{V}_{zz} \end{pmatrix} = \begin{pmatrix} -\tilde{V}_{zz}(1-\eta)/2 & 0 & 0 \\ 0 & -\tilde{V}_{zz}(1+\eta)/2 & 0 \\ 0 & 0 & \tilde{V}_{zz} \end{pmatrix} \tag{7.9}$$

The local EFG can therefore be described by three parameters, the basis rotation angle α, the largest eigenvalue $\tilde{V}_{zz}$ and the asymmetry parameter η. Using these free parameters, the angular dependence of the spin-echo modulation needs to be reproduced for the A and B/C vanadium sites.
In order to do so, a program using the Python language has been written which performs an algorithm, explained in the following.
In order to perform a field rotation, a rotation matrix about the x axis with rotation angle ϕ is created, which is then multiplied onto the starting vector [111] of the

field rotation process. The EFG in its diagonal form is set up by using the initial parameters η and $\tilde{V}_{zz}$ according to Eq. 7.9. With an initial value for α, the assumed eigenvectors $\vec{E}_y$ and $\vec{E}_z$ are calculated by rotating the y and z axis about the x axis by α, according to Eq. 7.7. They are called "assumed" since the α parameter will be refined over the iterations, until the basis is correct.
Using these eigenvectors, the diagonal form of the EFG is being transformed into the natural base, which results in an EFG as seen in Eq. 7.5. In order to do so, the basis transformation matrix A_{ij} is calculated:

$$\begin{pmatrix} 1 & y_1 & z_1 \\ 0 & y_2 & z_2 \\ 0 & y_3 & z_3 \end{pmatrix} \begin{pmatrix} A_{11} & A_{12} & A_{13} \\ A_{21} & A_{22} & A_{23} \\ A_{31} & A_{32} & A_{33} \end{pmatrix} = \begin{pmatrix} 1 & 0 & 0 \\ 0 & 1 & 0 \\ 0 & 0 & 1 \end{pmatrix} \tag{7.10}$$

With this transformation matrix, multiplying it onto the diagonal form yields the EFG in the natural base.

$$V_{ij} = \begin{pmatrix} \tilde{V}_{xx} & 0 & 0 \\ 0 & V_{yy} & V_{yz} \\ 0 & V_{yz} & V_{zz} \end{pmatrix} =$$

$$= \begin{pmatrix} A_{11} & A_{12} & A_{13} \\ A_{21} & A_{22} & A_{23} \\ A_{31} & A_{32} & A_{33} \end{pmatrix}^{-1} \begin{pmatrix} -\tilde{V}_{zz}(1-\eta)/2 & 0 & 0 \\ 0 & -\tilde{V}_{zz}(1+\eta)/2 & 0 \\ 0 & 0 & \tilde{V}_{zz} \end{pmatrix} \begin{pmatrix} A_{11} & A_{12} & A_{13} \\ A_{21} & A_{22} & A_{23} \\ A_{31} & A_{32} & A_{33} \end{pmatrix} \tag{7.11}$$

The quadrupolar interaction or the spin-echo modulation frequency can now be calculated using the formula given by Eq. 7.1, for magnetic field directions written in the natural base.
Once we calculate the EFG tensor for one of the three ^{51}V sites of the regular base triangle, the EFG tensor of the other sites can be obtained via the rotation of the tensor by $\pm 120°$. Equivalently, the magnetic field can be rotated by 120° as the orientation of the field rotation axis $\vec{A}_{rot}$ defines the A, B and C sites to begin with.

$$\vec{H}_{rot,B/C} = \begin{pmatrix} \cos(120°) & -\sin(120°) & 0 \\ \sin(120°) & \cos(120°) & 0 \\ 0 & 0 & 1 \end{pmatrix} \vec{H}_{rot,A} \tag{7.12}$$

After adjusting the initial parameters, an optimal EFG best reproducing the measurement data is obtained. Before the experiments, carried out in the previous section, a calculation of the local EFG has been performed by Pavel Marton [90] using density functional theory (DFT). The local EFGs for the base vanadium sites according to DFT are (in crystallographic base):

$$V_{ij} = \begin{pmatrix} 17.6 & 12.25 & 12.25 \\ 12.25 & -8.8 & -7.2 \\ 12.25 & -7.2 & -8.8 \end{pmatrix} \frac{V}{\text{Å}^2} \tag{7.13}$$

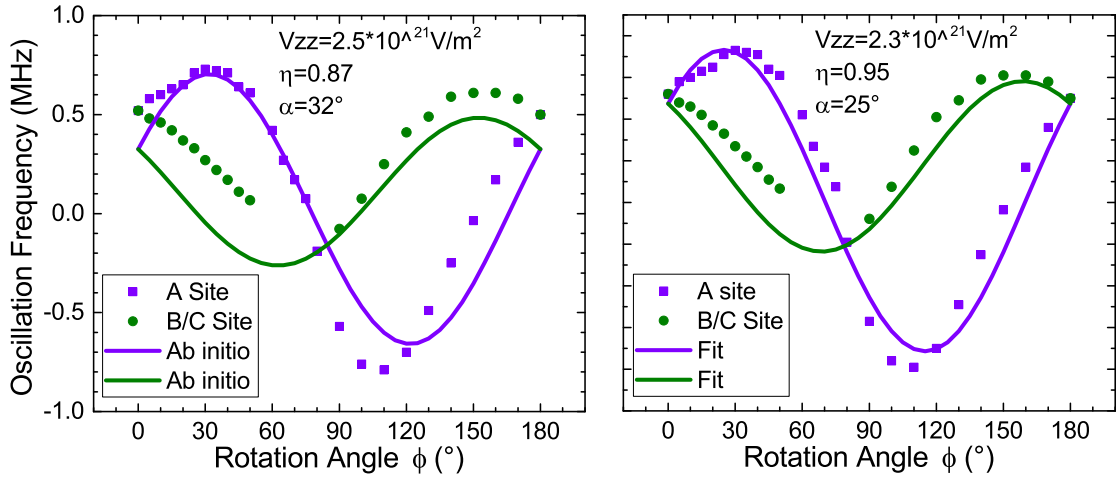

Figure 7.10: Angular dependence of the measured (symbols) and calculated (line) spin-echo modulation frequencies for an EFG obtained by DFT (left) and a fit (right). The EFG parameters V_{zz}, *eta* and the angle α between the y and z axes and the eigenvectors of the EFG tensor are each displayed in the top of the panel.

And in the natural base:

$$V_{ij} = \begin{pmatrix} -1.62 & 0 & 0 \\ 0 & -9.94 & 21.67 \\ 0 & 21.67 & 11.56 \end{pmatrix} \frac{V}{\text{Å}^2} \tag{7.14}$$

The EFG which has been obtained by fitting the calculated curve onto the experimental data using the free parameters, is given by (natural base):

$$V_{ij} = \begin{pmatrix} -0.65 & 0 & 0 \\ 0 & -16.18 & 19.67 \\ 0 & 19.67 & 16.83 \end{pmatrix} \frac{V}{\text{Å}^2} \tag{7.15}$$

The corresponding calculated spin-echo modulations for the ab initio and the fit are compared with the experimental values in Fig. 7.10.

In conclusion, the EFG tensor for the A, B and C site was determined based on fitting the previous measurements of the spin echo modulations in ^{51}V NMR via parameters corresponding to the matrix elements of the EFG. The ab initio DFT calculation and the experimentally determined EFG are in good agreement.

7.2 Hyperfine Coupling in GaV_4S_8

The NMR lineshift is a very useful tool for measuring the internal fields, produced by the magnetism of *d* electrons. Depending on the investigated sites and the location of the magnetic ions, the observed hyperfine fields can either be positive or negative. For a positive hyperfine coupling, the internal and the applied magnetic fields are co-aligned, and the necessary resonance field is reduced. A negative hyperfine coupling has these fields oriented antiparallel, which increases the resonance field with respect to its diamagnetic position. The sign and the strength of the hyperfine field depends on the magnetic moment of the magnetic ions, the location of the investigated nuclear site and the direction of the magnetic field. In the following, a series of NMR experiments will be shown, where a rotation of the applied magnetic field induces a rotation of the (electronic) magnetization, creating anisotropic hyperfine fields at the nucleus, which will be used to reconstruct the electronic distribution within the V_4S_4 cluster in GaV_4S_8.

7.2.1 ^{51}V NMR Spectra under Different Field Rotation Planes

In section 6.3, ^{51}V spectra recorded under a magnetic field rotation about the $[1\bar{1}0]$ axis have already been analysed to quantify domain populations in GaV_4Se_8. The anisotropy of the hyperfine field in GaV_4S_8 shows nearly identical behaviour, which means that the electronic distribution within the V_4Se_4/S_4 clusters are very similar. With the additional site specific EFG measurement for GaV_4S_8 described in section 7.1, we gain information about the differences in internal fields for each of the V sites, that become inequivalent upon field rotation. Similarly to the EFG tensor, the hyperfine coupling tensor is also related by a 120° rotation between the A, B and C sites. Therefore, under arbitrary field orientations, the hyperfine fields for the three sites would be different, although these differences are small compared with the overall amplitude of the anisotropy of the hyperfine field. In Fig. 7.11, the ^{51}V spectra are shown under a field rotation about the $[1\bar{1}0]$ axis, together with their respective resonance fields. Only the lines corresponding to the domain D1 are shown here, as the crystal was poled to prefer this domain in order to suppress possible overlaps with the lines originating from other domains. Despite the poling, the sample was not turned to the perfect mono-domain state and lines corresponding to other domains appear at $\phi \approx 60°$. The spectrum at $\phi = 55°$ was inconclusive regarding the observed line due to overlaps and is not included in the resonance field graph, since no resonance field (or quadrupolar oscillation frequency) could be uniquely extracted. Note that the shape of the spectra does not stay constant under rotation due to the change in quadrupolar interaction as well as the inequivalence of the anisotropy of the hyperfine coupling for the A and B/C sites. The different resonance field curves

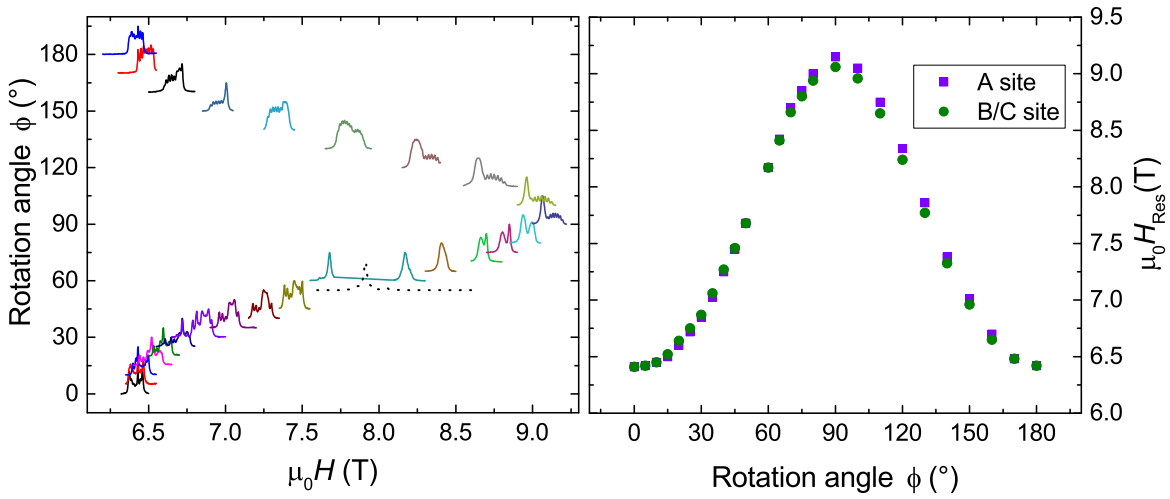

Figure 7.11: Left: ^{51}V spectra under $[1\bar{1}0]$ field rotation. The normalized spectra are stacked on top of each other in a way, to have the y position of the spectra be equal to field rotation angle it was measured under.
Right: Resonance fields of the corner and axis sites versus rotation angle. The position $\phi = 0°$ corresponds to the [111] field orientation.

for the A and the B/C sites intersect at around 60-70°, which is an important feature, as it yields information about the hyperfine coupling in the base triangle of the V_4S_4 cluster(see chapter 7.2.5). Due to the three-fold symmetry of the V_4S_4 cluster, a field rotation about the $[1\bar{1}0]$ axis will yield the same resonance field curve as the $[01\bar{1}]$ and $[10\bar{1}]$ rotations. In order to determine the detailed angular dependence of the hyperfine coupling, different field rotation planes need to be measured as well. Therefore the spectra for a field rotation about the $[11\bar{2}]$ axis are shown in Fig. 7.14. Since all three ^{51}V sites contribute to the NMR spectrum observed upon rotation of the magnetic field in the $(11\bar{2})$ plane, the nomenclature, which extends the former A, B and C sites, will be established first by analysing the spectra recorded in the (111) plane.
In Fig. 7.12 ^{51}V spectra are shown, measured in 30° steps. The spectra repeat with a period of 60° upon field rotation, as expected from the threefold symmetry of the cluster. The out-of-plane anisotropy of the hyperfine coupling is very strong, having an amplitude of around 2.7 T. In contrast, the amplitude of the in-plane anisotropy is found rather small, 0.04 T, when rotating the magnetic field in the (111) plane. It is determined by the difference between the spectra with $\vec{H} \parallel [1\bar{1}0]$ and $\vec{H} \parallel [11\bar{2}]$. Spectra recorded at ϕ angles, different by $n60°$, should be identical in the case of no misalignment. Due to the large out-of-plane anisotropy, even small misalignments would show up in a large shift of these spectra relative to each another. This effect seems to be very small in this case, as the lines seen in Fig. 7.12 do not deviate very

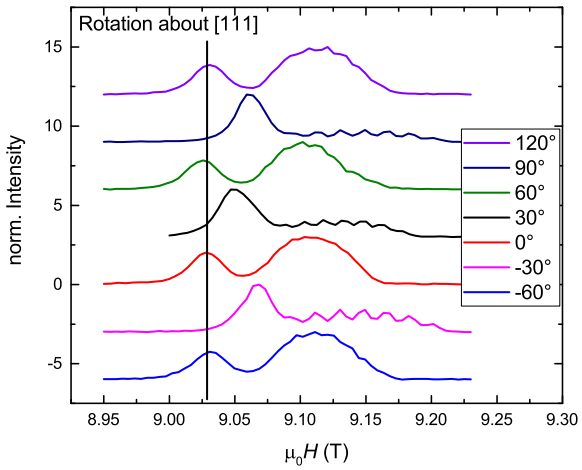

Figure 7.12: ^{51}V spectra under [111] field rotation. The negligible shift of the spectra upon rotation by each 60° with respect to the vertical black line indicates the absence of misalignments.

much from the vertical guide line. This confirms that the crystal is well oriented. Since the spectra repeat after a 60° rotation, it is enough to measure a 30° patch in more detail, starting from a [11$\bar{2}$] field direction and rotating to a [1$\bar{1}$0] direction. On the left panel of Fig. 7.13 this 30° patch is shown as individual spectra recorded in $\Delta\phi = 2°$ steps. Lines from a less populated domain can be seen moving inwards from lower fields, and eventually overlapping with the investigated domain (D1) when the field is parallel to the [1$\bar{1}$0] direction. Note that a [1$\bar{1}$0] type direction was used previously to measure the domain fraction of the overlapping D3 and D4 domains. In this case though, the overlapping lines correspond to the domains D1 and one of the other three, as continuous rotation would go through the remaining domains one by one, each overlapping with the line corresponding to D1. Also with this setup, one can measure the domain population by switching through the different [1$\bar{1}$0] type positions and compare the intensities of the overlapped and undisturbed D1 line.
More importantly, the three ^{51}V sites are inequivalent in between the two high symmetry directions [11$\bar{2}$] and [1$\bar{1}$0]. Starting from the [11$\bar{2}$] direction, where there are two equivalent ^{51}V lines (prev. B/C site) corresponding to the left peak, the line splits and one of the two lines gradually moves towards the A site. This site is referred to as the B site, with the remaining site being called C site. Due to the increasing quadrupolar interaction, the B site line increases its width and eventually starts showing satellites when reaching the [1$\bar{1}$0] direction. It then becomes equivalent with the A site as they overlap. For an illustration showing the different sites, see the right panel of Fig. 7.13.

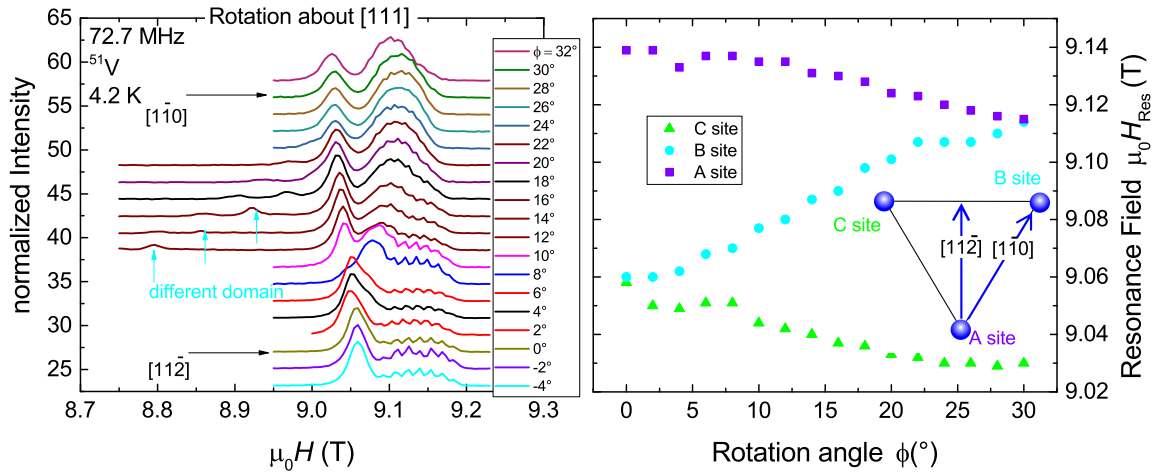

Figure 7.13: Left: ^{51}V spectra under [111] field rotation. Starting from the [11$\bar{2}$] orientation ($\phi = 0°$), one of lines corresponding to the previously equivalent B/C sites moves towards the A-site line, and becomes equivalent with it at the [1$\bar{1}$0] direction.
Right: Resonance fields of the three bottom ^{51}V sites, and a sketch of the 30° field rotation.

When tracking the resonance fields for each site through the 30° field rotation, one obtains a Z-shaped curve, where the two high symmetry positions are the only ones with two sites being equivalent, hence three lines are visible the intermediate angular range. For rotation planes containing the [111] direction, this inequivalence of the sites gradually gets weaker when approaching the [111] direction during rotation, since the projection of the field direction onto the base plane approaches zero. For the field rotation about the [11$\bar{2}$] axis, the anisotropy of the hyperfine coupling is again dominated by the out-of-plane anisotropy, while the in-plane anisotropy plays a minor role. The line identification is not as straightforward as in the [1$\bar{1}$0] rotation, since a measurement of the quadrupolar oscillations on each rotation angle has not been performed due to large time investments involved. Additionally, due to another domain interfering close to the ϕ =90° position, the quadrupolar oscillations may not be uniquely assignable. However, for the ϕ =90° position, the sites are identified from the [111] rotation experiment, and for some angles around it, the lines can be traced.

Based on the resonances followed upon field rotation in seven planes, the three ⟨1$\bar{1}$0⟩-type planes, the three ⟨11$\bar{2}$⟩ -type planes and the (111) plane, one can obtain a 3D resonance field surface plot, which gives a vivid overview of the shape of the hyperfine coupling tensor. The resulting spherical colourplot represents the resonance field as a function of the orientation of the external field at 72.7 MHz. Each site would have its own sphere, which is rotated by 120° with respect to the others. When linearly

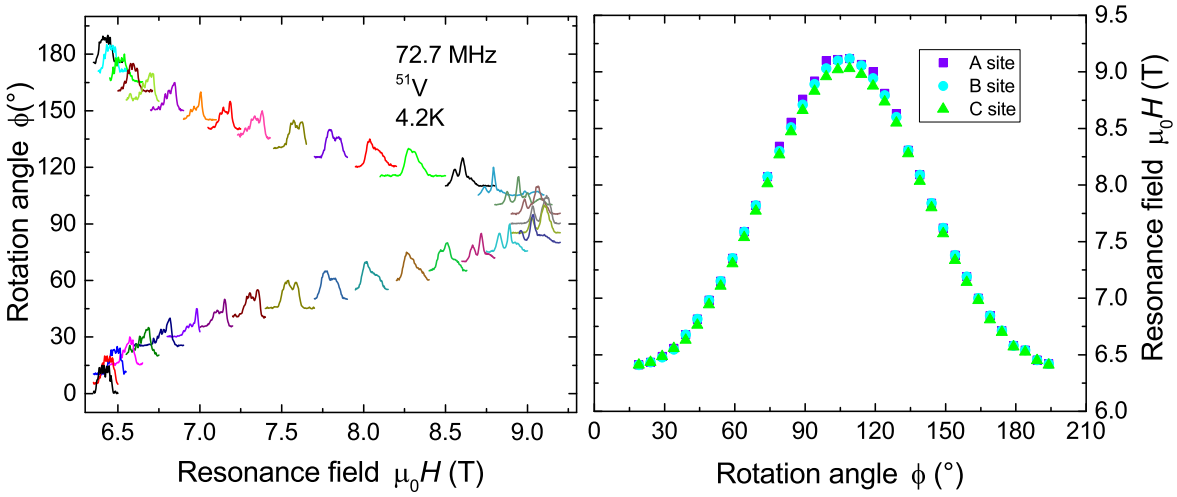

Figure 7.14: Left: ^{51}V spectra under $[11\bar{2}]$ field rotation. The normalized spectra are stacked on top of each other in a way, to have the y position of the spectra be equal to field rotation angle it was measured under.
Right: Resonance fields of the A, B and C sites versus rotation angle. The position $\phi = 0°$ corresponds to the [111] field orientation.

extrapolating between the different field rotation planes 30° apart from another, one gets the resonance field map seen in Fig. 7.15a. The sharp or non-smooth transitions between the slices come from different offset values between the $[1\bar{1}0]$ and the $[11\bar{2}]$ rotation experiments. The anisotropy of the hyperfine tensor has its largest derivative at a polar angle around $\theta = 45°$, which means that small deviations in angle between the two types of field rotation planes would be best visible in this regime, causing a $\phi = 60°$ periodic waving in the colourplot. The in-plane anisotropy is non-zero, so even though exaggerated by an offset originating from incorrectly assigned [111] field directions, such a modulation of the hyperfine field is expected. The version using the corrected 0° positions is shown in Fig. 7.15b. It was corrected for by using a dataset produced by the fitted hyperfine coupling tensor, shown in the following.

This plotted 3D sphere is a representation of the hyperfine coupling matrix $\mathcal{A}_{\mathrm{Hf}}$. When fitting the measured resonance field curves via the internal fields described by the hyperfine coupling tensor, the matrix elements can be extracted:

$$H_{\mathrm{int}} = \mathcal{A}_{\mathrm{Hf}} \frac{\vec{H}}{|\vec{H}|} \tag{7.16}$$

For each field direction in the rotation experiments, the internal field can be calculated for a set of matrix elements, which are then optimized to fit the data, as described in section 7.2.3. The resulting hyperfine coupling matrix is then given

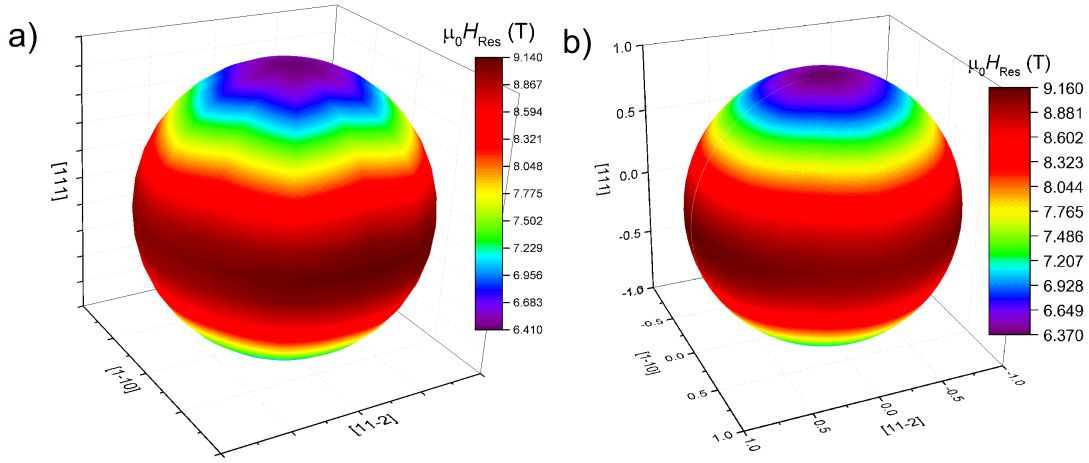

Figure 7.15: a) 3D representation of the resonance fields for the A site (or B or C site, when rotated by 120°). The spike like features are due to offsets between the $[1\bar{1}0]$ and the $[11\bar{2}]$ rotation experiments. b) Correcting for the offsets by plotting the resonance fields produced by the hyperfine coupling tensor smooths out the picture, and yields a representation of the hyperfine coupling tensor.

by:

$$\mathcal{A}_{\mathrm{Hf}} = \begin{pmatrix} -2.55 & 0 & 0 \\ 0 & -2.66 & -0.03 \\ 0 & -0.03 & 0.09 \end{pmatrix} \mathrm{T} \tag{7.17}$$

Similarly to the EFG, the hyperfine coupling matrix obeys the local site symmetry, showing an invariance by mirror plane reflection of the yz plane.

The comparison with the quadrupolar interaction also provides an additional possibility for checking the validity of the hyperfine coupling tensor. With the previously established EFGs, either via ab initio [90] or fitting of the quadrupolar oscillation measurements, the interaction with the quadrupolar moment of the nucleus contains a magnetic field direction. Previously, the direction of the external magnetic field was used in the analysis of the quadrupolar interaction, however the sum of the external and internal field is in fact the relevant field for the quadrupolar interaction, as described in Eq. 7.1. Therefore, the hyperfine coupling can be used to improve the previous analysis, now involving the hyperfine fields:

$$\vec{H}_{\mathrm{tot}} = \vec{H}_{\mathrm{ext}} + \mathcal{A}_{\mathrm{Hf}} \frac{\vec{H}_{\mathrm{ext}}}{|\vec{H}_{\mathrm{ext}}|} \tag{7.18}$$

In Fig. 7.16 a) and b), the previous and the internal field corrected simulations of

the quadrupolar oscillation curves are shown, using the EFG obtained by DFT. A substantial improvement is observed, indicating that the the strong internal fields are indeed influencing the quadrupolar interaction. In Fig. 7.16 c) and d), the quadrupolar oscillation curves using the fitted EFG are shown, without and with internal field correction, which reveals a almost perfect accordance with the experiment. This is strong evidence for the correctness of the determined hyperfine coupling tensor, as well as the EFG.

In conclusion, the ^{51}V spectra were recorded for different field rotation axes, namely the $[1\bar{1}0]$, $[11\bar{2}]$ and [111]. From these spectra, the angular dependences of the hyperfine shifts are determined, which are displayed as the hyperfine coupling matrix. For each field direction, the internal field can therefore be determined, which further improved the previous fit of the angular dependence of the quadrupolar interaction.

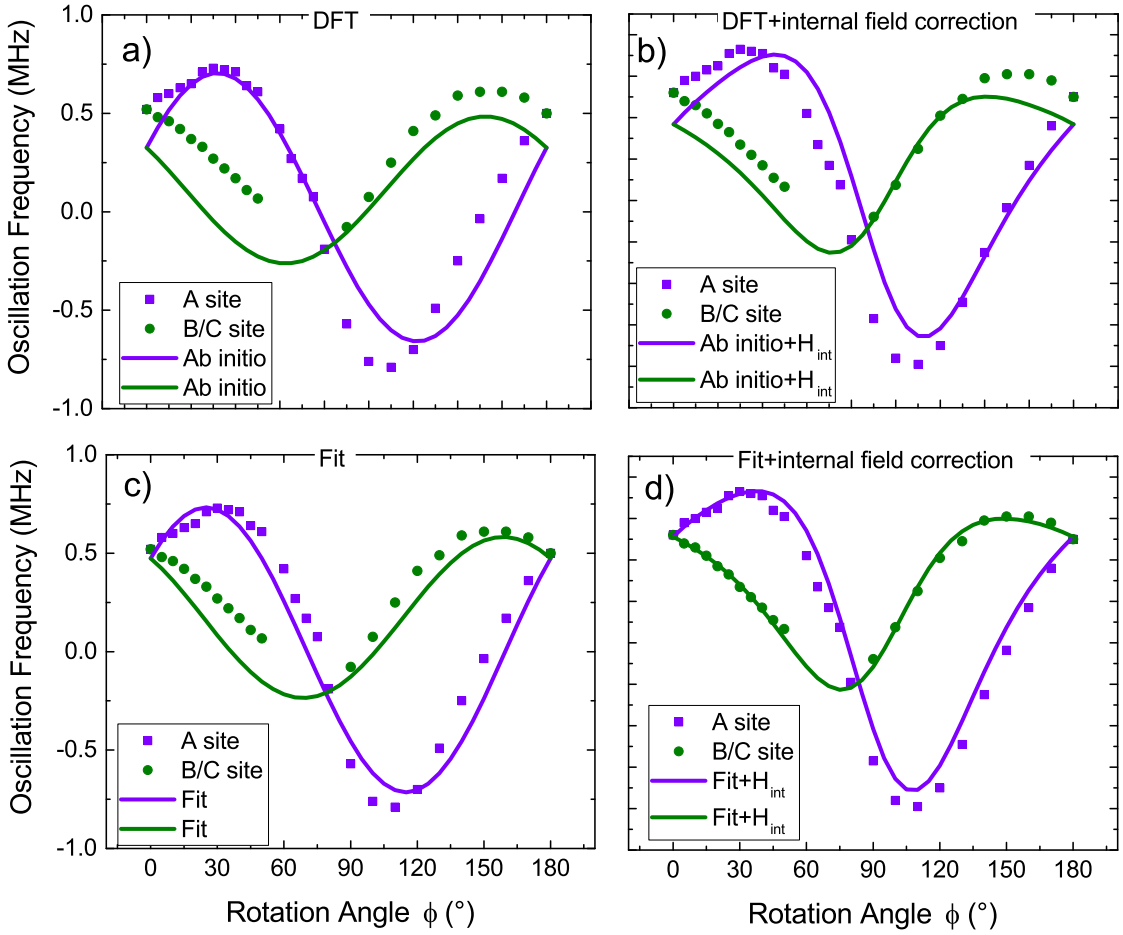

Figure 7.16: a) and c): Measured (scatter) and simulated(solid) spin-echo modulation frequencies for the EFGs obtained by DFT (a) and fitting (b). The chosen direction of the magnetic field in the simulations was the applied external field direction. b) and d) Simulations for EFGs obtained by DFT (b) and fitting (d), where the direction of the magnetic field was modified to $\vec{H}_{\mathrm{tot}} = \vec{H}_{\mathrm{Res}} + \vec{H}_{\mathrm{int}}$

7.2.2 Origins of Hyperfine Fields in GaV_4S_8

The possible contributions to the hyperfine fields are given by the dipole field induced by the spin and orbital angular momenta of the d electrons and the Fermi contact term, originating from polarized s orbitals, as discussed in section 2.2.1. The Fermi contact part of the hyperfine field is isotropic and is a measure of the spin density at the nucleus [99]. The dipole contribution of the hyperfine field is anisotropic, and responsible for the observed anisotropy of the hyperfine coupling. The spin contribution dominates over the orbital one, and the latter can be neglected due to several

reasons. First, the magnetic properties of $GaV_4S(e)_8$ can be well approximated by a spin $\frac{1}{2}$ only model [70], though orbital contributions are manifested e.g. via the anisotropies of the susceptibility and the g tensor [100].
Second, due to the Jahn-Teller instability, the uppermost partially filled t_2 cluster orbital state is split into a low-lying singlet, hosting the single unpaired d electron of the V_4S_4 unit and an unoccupied doublet. This occupation of an orbital singlet causes a quenching of orbital momentum, and hence no contribution from the orbital term. Therefore, only the dipole fields due to spin distribution over the V_4S_4 cluster and contact interactions are considered in the following, while dipole fields from neighbouring V_4 units are neglected due to large inter-cluster distances [101, 102].

7.2.3 Simulating Hyperfine Fields in GaV_4S_8

In GaV_4S_8, the main contribution to the internal fields can be attributed to the spin density on a given V_4S_4 cluster and the contact interaction, while dipole fields originating from neighbouring clusters only play a minor role [101]. As described in section 2.2.1, the internal field H_e is given by:

$$\vec{H}_\mathrm{e} = -\frac{2\mu_\mathrm{B}\mu_0}{4\pi}\left(-\frac{\vec{s}}{|\vec{r}-\vec{r}_0|^3} + \frac{\vec{r}(\vec{r}\cdot\vec{s})}{|\vec{r}-\vec{r}_0|^5} + \frac{8}{3}\pi\vec{s}\delta(r-r_0)\right) \tag{7.19}$$

The nucleus is at the position $\vec{r}_0$, and the electron, producing a magnetic dipole field, resides at $\vec{r}$. For an arbitrary spin distribution over the cluster, the nucleus will be exposed to a magnetic field originating from the dipole field of the distribution, obtained by integrating the dipole fields in Eq. 7.19, weighted by the spatial spin distribution over the cluster.

$$H_{\mathrm{e,i}}(\vec{r}_0) = -\frac{2\mu_\mathrm{B}\mu_0}{4\pi}\int p(\vec{r})\cdot\left(-\frac{s_\mathrm{i}}{|\vec{r}-\vec{r}_0|^3} + \frac{r_\mathrm{i}s_\alpha r_\alpha}{|\vec{r}-\vec{r}_0|^5}\right)dr^3 \tag{7.20}$$

Instead of performing the integral analytically, the internal field is being calculated numerically, using finite volume elements ΔV.

$$\vec{H}_\mathrm{e} = -\frac{2\mu_\mathrm{B}\mu_0}{4\pi}\sum\frac{P_i}{V}\left(-\frac{\vec{s_i}}{|\vec{r}-\vec{r}_0|^3} + \frac{\vec{r_i}|\vec{r_i}\cdot\vec{s_i}|}{|\vec{r}-\vec{r}_0|^5}\right)\Delta V \tag{7.21}$$

The sum is performed for all cubic volumes ΔV around all $\vec{r_i}$ with nonzero probabilities P_i of the electron residing in the volume ΔV. The volumes around $\vec{r_i}$ and $\vec{r_j}$ do not overlap for $i \neq j$, instead the whole 3D space is tiled seamlessly in a cubic grid. For a single point-like electron, this will just yield the point dipole field of an electron at the position $\vec{r_i}$. While a continuous distribution of electron locations instead gives a weighted sum of dipole field contributions.

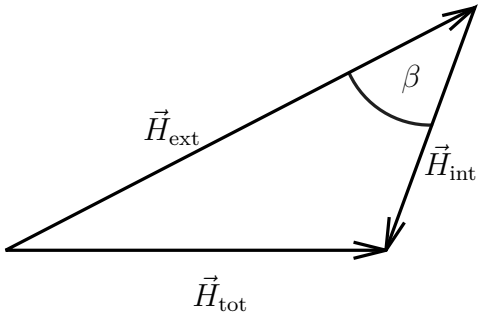

Figure 7.17: Resonance condition with the resonance field $\vec{H}_{\text{ext}}$ and the internal field $\vec{H}_{\text{int}}$ adding up to the total field $|\vec{H}_{\text{tot}}| = \omega_{\text{L}}/^{51}\gamma$. The law of cosines yields: $|\vec{H}_{\text{tot}}|^2 = |\vec{H}_{\text{ext}}|^2 + |\vec{H}_{\text{int}}|^2 - 2\cos(\beta)|\vec{H}_{\text{ext}}||\vec{H}_{\text{int}}|$

In the limit of $dV \to 0$, the continuous distribution is mapped out perfectly, when computing the hyperfine fields, however, a finite resolution is chosen for computation. Given an electronic distribution via the wavefunction Ψ_e, one could calculate the internal field produced by the electronic dipole moment by performing the sum with the probability density $P(\vec{r}) = |\Psi_e|^2$.Depending on the resulting internal field at the nucleus, an external field must be applied to reach the resonance condition $\omega_{\text{L}} = \gamma H$. This can be done via the law of cosines depicted in Fig. 7.17.

$$|\vec{H}_{\text{ext}}|^2 - 2|\vec{H}_{\text{ext}}||\vec{H}_{\text{int}}|\cos(\beta) + |\vec{H}_{\text{int}}|^2 - \frac{\omega_{\text{L}}^2}{\gamma^2} = 0 \tag{7.22}$$

Solving the quadratic equation for $|\vec{H}_{\text{ext}}|$ yields the magnitude of the applied magnetic field given that we know the internal field, that is the sum of the dipolar field and the contact term, and the direction of the external field. Similarly to the evaluation of the electric field gradient, a Python program has been written, which sums up all the dipole fields of a given discrete distribution and calculates the hyperfine coupling tensor via selecting specific field directions in order to calculate the matrix elements of the hyperfine coupling tensor. Then it performs a field rotation and calculates the resulting resonance field curves, while the magnetization (the direction of the spin in Eq. 7.19) is kept co-aligned with the external magnetic field.

For higher external fields (>5T), the electron magnetization aligns with the magnetic field, as demonstrated by the small anisotropy of the saturation magnetization shown in Fig. 3.7. However a small deviation between the magnetizations for different field orientations remains, appearing to have a bias towards the [111] direction. This is modeled in the following by introducing a tilting angle α between the magnetic field and the electron magnetization, as pictured in Fig. 7.18. In order to correctly simulate the field rotation experiments, a small correction needs to be implemented within the code regarding this angle. Before implementing this into to simulation, a quantification of this tilting angle α is needed.

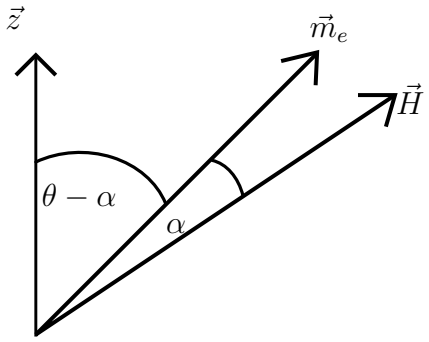

Figure 7.18: Tilting of the electron spin towards the magnetic easy axis. The spins therefore do not exactly align with the magnetic field.

The energy of the electron spin is the sum of its anisotropy energy and the Zeeman energy. The magnetocrystalline anisotropy, studied in GaV_4S_8 via ESR [100], is independent of the magnitude of the applied magnetic field H. Therefore, for high magnetic fields, magnetocrystalline anisotropy can be neglected with respect to the Zeeman energy. The g-tensor anisotropy is therefore the most relevant anisotropy, due to the g-tensor anisotropy energy being proportional to H. In Fig. 3.7, the deviation of the saturation magnetizations for different field directions is constant over H, which shows that g-tensor anisotropy must be dominant for large fields, and is therefore responsible for the observed tilting of the electron magnetization. The energy of the electron with respect to the tilting angle α is given by

$$E = -\vec{M}\hat{g}\vec{H} = MH \begin{pmatrix} \sin(\theta-\alpha) \\ 0 \\ \cos(\theta-\alpha) \end{pmatrix} \begin{pmatrix} g_\perp & 0 & 0 \\ 0 & g_\perp & 0 \\ 0 & 0 & g_\parallel \end{pmatrix} \begin{pmatrix} \sin(\theta) \\ 0 \\ \cos(\theta) \end{pmatrix} =$$

$$= MH[g_\perp \sin(\theta-\alpha)\sin(\theta) + g_\parallel \cos(\theta-\alpha)\cos\theta] \tag{7.23}$$

The spin will orient itself in order to minimize its energy, therefore $\frac{d}{d\alpha}E = 0$.

$$\frac{d}{d\alpha}E = MH\left[-g_\perp \cos(\theta-\alpha)\sin\theta + g_\parallel \sin(\theta-\alpha)\cos\theta\right] =$$

$$= MH\left[-g_\perp \sin\theta(\cos\theta\cos\alpha + \sin\theta\sin\alpha) + g_\parallel \cos\theta(\sin\theta\cos\alpha - \cos\theta\sin\alpha)\right]$$

Since α can be assumed to be small due to the small difference in saturation magnetizations, $\sin\alpha \approx \alpha$ and $\cos(\alpha) = 1$.

$$\frac{d}{d\alpha}E = MH\left[\sin\theta\cos\theta(g_\parallel - g_\perp) - \alpha(g_\parallel \cos^2\theta + g_\perp \sin^2\theta)\right] \stackrel{!}{=} 0 \tag{7.24}$$

From this condition, α can be determined.

$$\alpha = \frac{\sin\theta\cos\theta(g_\parallel - g_\perp)}{g_\parallel \cos^2\theta + g_\perp \sin^2\theta} \tag{7.25}$$

The tilting angle α therefore vanishes for $\theta = 0°$ and $\theta = 90°$, however the intermediate angle $\theta = 45°$ has a maximum tilting angle. This accelerates the rotation of the electron spin with respect to the magnetic field, as the magnetization is always closer to the [111] direction than the magnetic field due to the tilting. Including this into the simulations will therefore reduce the angular width of the simulated curves. For a given α and θ value from the experiment, the ratio of $g_\parallel$ to $g_\perp$ can also be calculated.

$$\frac{g_\parallel}{g_\perp} = \frac{\alpha \sin^2\theta + \sin\theta\cos\theta}{-\alpha\cos^2\theta + \sin\theta\cos\theta} \tag{7.26}$$

In the simulations discussed in the following sections, a tilting angle α corresponding to the following g factor ratio was best fitting the NMR data.

$$\frac{g_\parallel}{g_\perp} = 1.055 \tag{7.27}$$

In the following, the method shown in this section will be applied for different electron distributions, in order to calculate the hyperfine fields corresponding to these distributions and to reconstruct the spin distribution over the cluster.

7.2.4 Hyperfine Coupling Described by a Distribution of Point Dipoles

In order to simulate the anisotropy of the hyperfine coupling using dipole and contact interactions, a simplistic point-dipole model is used to have a rough estimate for the relative position of the electron with respect to the nucleus. In the case of having the electron fully localized to a point, the hyperfine field reads as

$$\vec{H}_n = \vec{H}_{ext} - \frac{\mu_0\mu_\mathrm{B}}{4\pi}\left(\frac{\vec{H}_{ext}/H_{ext}}{r^3} - \frac{3\vec{r}(\vec{H}_{ext}/H_{ext})\vec{r}}{r^5}\right). \tag{7.28}$$

Here, the magnetic moment of an electron is placed at a position $\vec{r}$ where the vanadium nucleus is at the origin. The magnetic moment co-aligned with the external magnetic field, hence the moment's direction $\vec{H}_\mathrm{ext}/H_\mathrm{ext}$. When placing the electron on the z axis above the nucleus and starting a field rotation in an arbitrary plane containing the z axis, the resulting field is:

$$\begin{aligned}\vec{H}_n &= H_{ext}\begin{pmatrix}\sin(\phi)\\ \cos(\phi)\end{pmatrix} - \frac{\mu_0\mu_\mathrm{B}}{4\pi r^3}\left[\begin{pmatrix}\sin(\phi)\\ \cos(\phi)\end{pmatrix} - 3\begin{pmatrix}0\\1\end{pmatrix}\left[\begin{pmatrix}\sin(\phi)\\ \cos(\phi)\end{pmatrix}\begin{pmatrix}0\\1\end{pmatrix}\right]\right] = \\ &= H_{ext}\begin{pmatrix}\sin(\phi)\\ \cos(\phi)\end{pmatrix} - \frac{\mu_0\mu_\mathrm{B}}{4\pi r^3}\begin{pmatrix}\sin(\phi)\\ -2\cos(\phi)\end{pmatrix}\end{aligned} \tag{7.29}$$

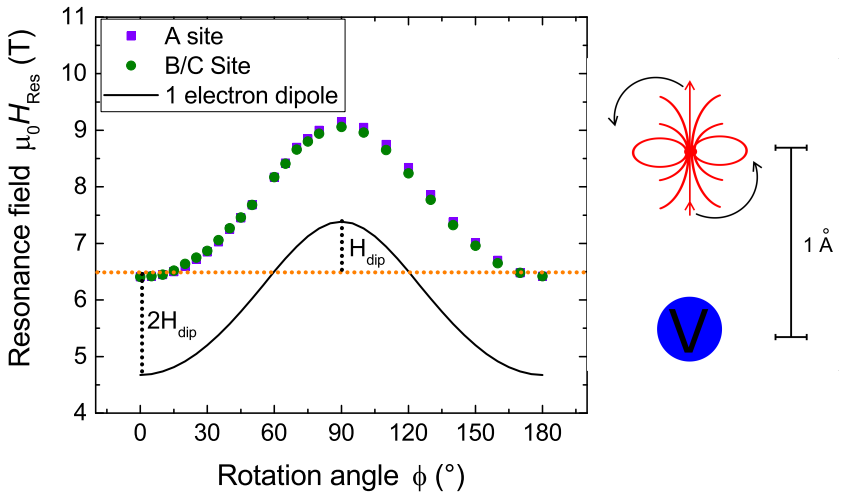

Figure 7.19: Simulated hyperfine dipole fields from a single electron in a 1Å distance to a ^{51}V nucleus. The anisotropy of dipole fields is visible via the difference in the $\phi = 0°$ and $\phi = 90°$ fields.

For a distance $r = 1$ Å, the dipole fields match the experimental values well as seen in Fig. 7.19, except for an angular independent offset, which needs to be introduced via the contact interaction. This simplistic model only considers one of the three vanadium nuclei in the base of the V_4 tetrahedron. Therefore this procedure is expanded to consider all of the three base sites. Additionally, a symmetric distribution above and below the nucleus is chosen. This distribution yields a similar result, now including dipole fields from the other sites, as seen in Fig. 7.20. The dipole fields from the other sites are responsible for the inequivalence of the three sites, visible via the Z-pattern in the (111) field-rotation plane in Fig. 7.20 d). This does not reproduce the experiment correctly, although similar. The in-plane anisotropy of the hyperfine fields need to be altered by changing the distribution in order to match the experiment. Additionally, an isotropic shift of 1.7 T needs to be implemented, which can be accounted for by the Fermi contact interaction and a core polarization originating from the electron in a $3d$ orbital. The distribution of 6 point dipoles can already reconstruct the anisotropy of the hyperfine coupling in GaV_4S_8 rather well, considering its simplicity. It also points towards the rough distribution of charges around the nuclei, as maxima and minima need to be present at $\phi = 90°$ and $\phi = 0°$. Due to the shape of dipole fields, spin densities in the basal plane are also possible, as long as the overall dipole contribution produces a net amplitude of 2.7 T, since in-plane contributions compete with the vertical contributions.

An additional application for the point dipole model would be to check whether a spin distribution completely located at the U site is able to explain the hyperfine fields measured by NMR. A strong occupancy of the U site is suggested by previous

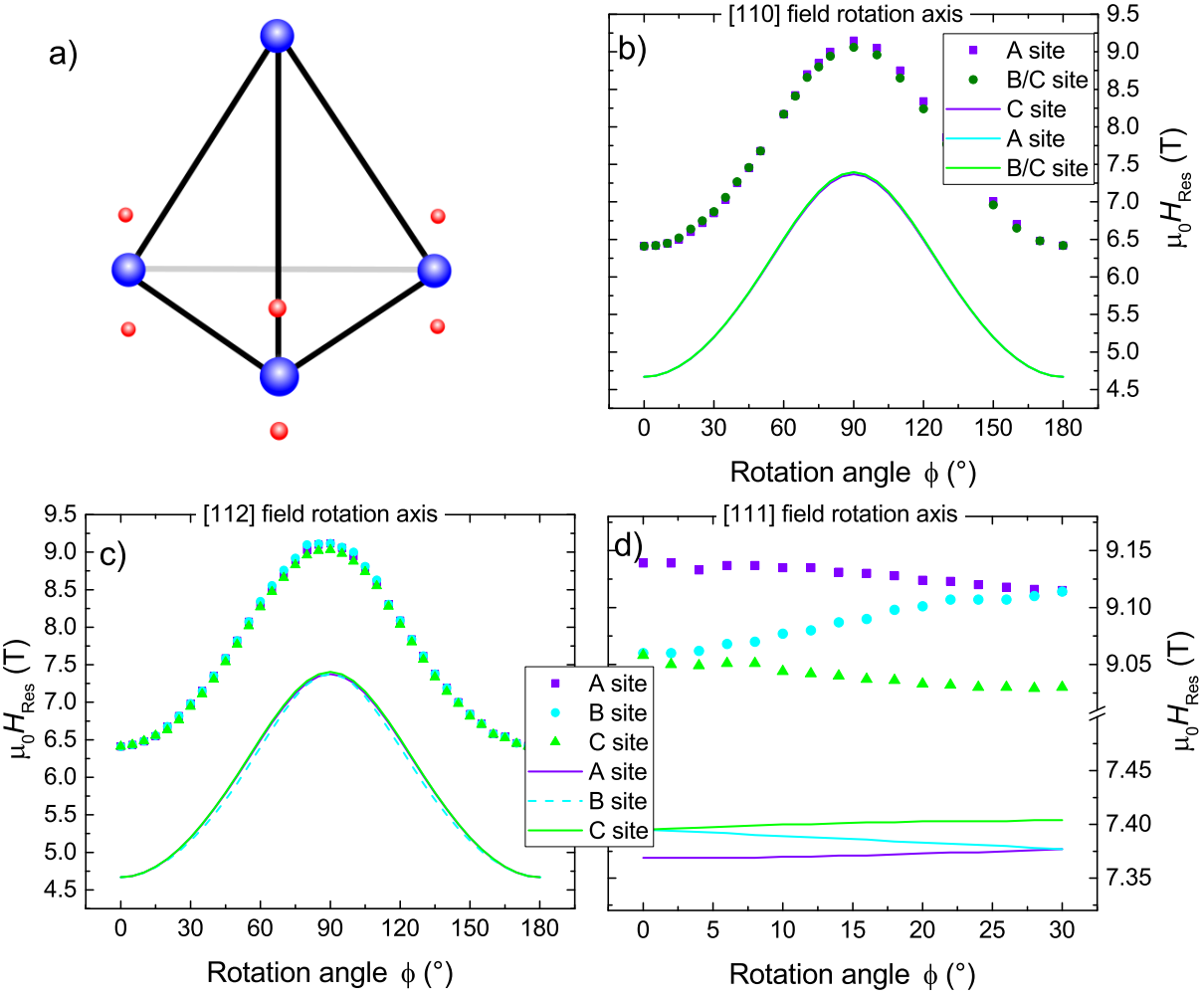

Figure 7.20: a) Schematic threefold symmetric spin distribution, utilizing two point charges above and below each V site on the bottom of the V_4 tetrahedron. b)-d) Comparison between the simulations of the resulting resonance fields for different field rotation planes and the experimental NMR values. There is good agreement even with this simple distribution, except for a missing isotropic negative shift and a needed correction of the in plane anisotropy in panel d).

theoretical work [103] using a LDA+U approach. To establish a vivid picture for the eventual spin distribution that is being constructed, a point dipole is gradually shifted from the U site ($h = 1h_{\text{tetra}}$) towards the basal plane ($h = 0$), eventually being in the center of the base triangle. The simulated resonance field curves are shown in Fig. 7.21, where the observed maxima and minima are gradually moving towards the $\phi = 0°$ and $\phi = 90°$ positions, respectively, when moving the dipole towards the

basal plane. The amplitude of the dipole fields is also small, in comparison with the measured values, hence an occupancy of the U site is only partially possible. The main contribution to the hyperfine fields must therefore come from spin density located in the basal plane, in the form of *d*-orbitals around the V ions, distributing the electron above and below the nucleus and in the basal plane. Additionally, the placement of the dipole reveals a simple rule of hand: The minimum of the resonance field is reached when the external field points from the nucleus towards the maximum of the weighted spin density. The weight accounts for the dipole fields decaying with $1/r^3$.

Based on this simple point dipole model shown above, it was already possible to localize a significant part of the electron distribution to the three A, B and C sites at the base of the V_4 tetrahedron, as dipole fields from the unique U site do not explain the observed anisotropy of the hyperfine coupling. Additionally, the distributions should have significant densities within the base plane around the nuclei as well as above/below the nuclei, due to the minima and maxima of the resonance fields being at $\phi = 0°$ and $\phi = 90°$. A more detailed description of the spin distribution is approached in the following section, using atomic *d* orbitals.

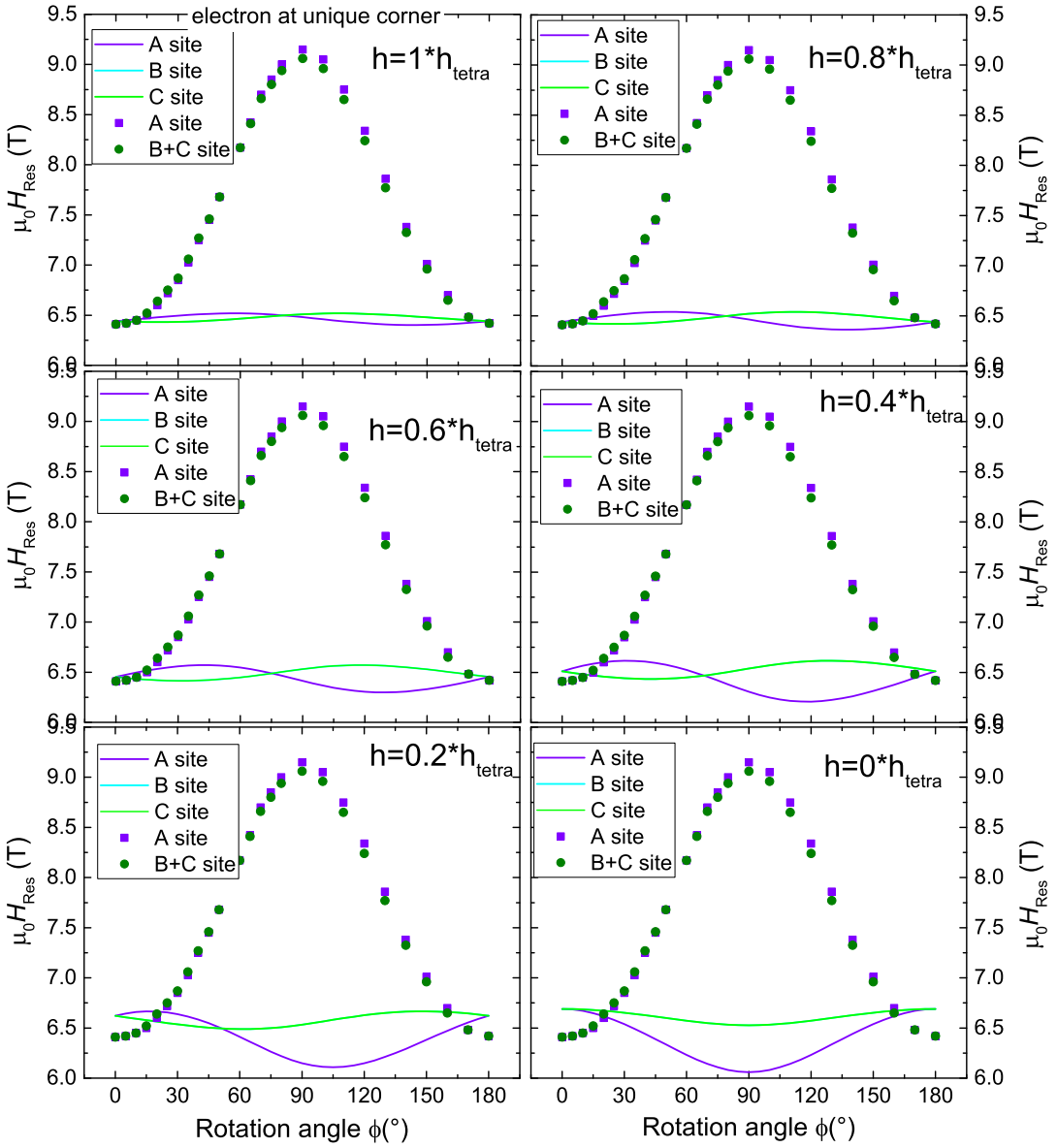

Figure 7.21: Resonance fields under continuous movement of a point dipole from the U site to the center of the base triangle. The minima and maxima approach the $\phi = 90°$ and $\phi = 0°$ positions, respectively.

7.2.5 Reconstructing the Spin Distribution via Superposition of Atomic d Orbitals

In order to model the overall spin distribution within the cluster, we utilize the near octahedral crystal field splitting of the d orbitals, shown in section 2.2.3. The five atomic d orbitals are split up into two degenerate subgroups, the eg and the T_{2g}, containing two and three orbitals, respectively. The wavefunctions of the real atomic d orbitals are given by [33]:

$$\Psi_{z^2}(r,\theta) = \frac{1}{81\sqrt{6\pi}}\left(\frac{Z}{a_0}\right)^{3/2}\frac{Z^2(r-r_0)^2}{a_0^2}e^{-\frac{Z(r-r_0)}{3a_0}}(3\cos^2\theta - 1) \tag{7.30}$$

$$\Psi_{xz}(r,\theta,\phi) = \frac{\sqrt{2}}{81\sqrt{\pi}}\left(\frac{Z}{a_0}\right)^{3/2}\frac{Z^2(r-r_0)^2}{a_0^2}e^{-\frac{Z(r-r_0)}{3a_0}}\sin\theta\cos\theta\cos(\phi) \tag{7.31}$$

$$\Psi_{yz}(r,\theta,\phi) = \frac{\sqrt{2}}{81\sqrt{\pi}}\left(\frac{Z}{a_0}\right)^{3/2}\frac{Z^2(r-r_0)^2}{a_0^2}e^{-\frac{Z(r-r_0)}{3a_0}}\sin\theta\cos\theta\sin(\phi) \tag{7.32}$$

$$\Psi_{xy}(r,\theta,\phi) = \frac{\sqrt{2}}{162\sqrt{\pi}}\left(\frac{Z}{a_0}\right)^{3/2}\frac{Z^2(r-r_0)^2}{a_0^2}e^{-\frac{Z(r-r_0)}{3a_0}}\sin^2\theta\sin(2\phi) \tag{7.33}$$

$$\Psi_{x^2-y^2}(r,\theta,\phi) = \frac{\sqrt{2}}{162\sqrt{\pi}}\left(\frac{Z}{a_0}\right)^{3/2}\frac{Z^2(r-r_0)^2}{a_0^2}e^{-\frac{Z(r-r_0)}{3a_0}}\sin^2\theta\cos(2\phi) \tag{7.34}$$

Using the rough criteria for the spin distribution discussed in section 7.2.4, the orbitals with large electron densities along the z axis and within the xy plane are considered as possible contributions, namely the d_{z^2} and $d_{x^2-y^2}$ orbitals. They are also lowest in energy, due to the smallest repulsion due to the ligands, as schematically shown in Fig. 7.22. The higher energy orbitals d_{xz} and d_{yz} are expected to be unoccupied, while the intermediate d_{xy} may contribute. The z direction is chosen to be the polar axis, as the orbital structure depends on the rhombohedral distortion, as seen via the domain specific internal fields. With the spin distribution being dominated by dipolar fields originating from spin densities above and below of the base nuclei as well as from spin densities in the basal plane, a superposition of d_{z^2} and $d_{x^2-y^2}$ orbitals may generate a plausible spin distribution for the V_4S_4 cluster.

At first, only d_{z^2} orbitals are considered as building blocks for the V_4S_4 cluster wavefunction, as suggested by Pocha et al. [72]. The cluster wavefunction is then simply the superposition of the individual d_{z^2} orbitals, centered on each ^{51}V site (A, B, C and U).

$$\Psi_{tot} = c^U_{z^2}\Psi_{z^2} + \sum_{\alpha=A,B,C} c^\alpha_{z^2}\Psi_{z^2} \tag{7.35}$$

The d_{z^2} orbitals for each site are identical except for a spatial translation.

$$\Psi^A_{z^2}(r,\theta) = \Psi^B_{z^2}(r-r_B,\theta) = \Psi^C_{z^2}(r-r_C,\theta) = \Psi^U_{z^2}(r-r_U,\theta) \tag{7.36}$$

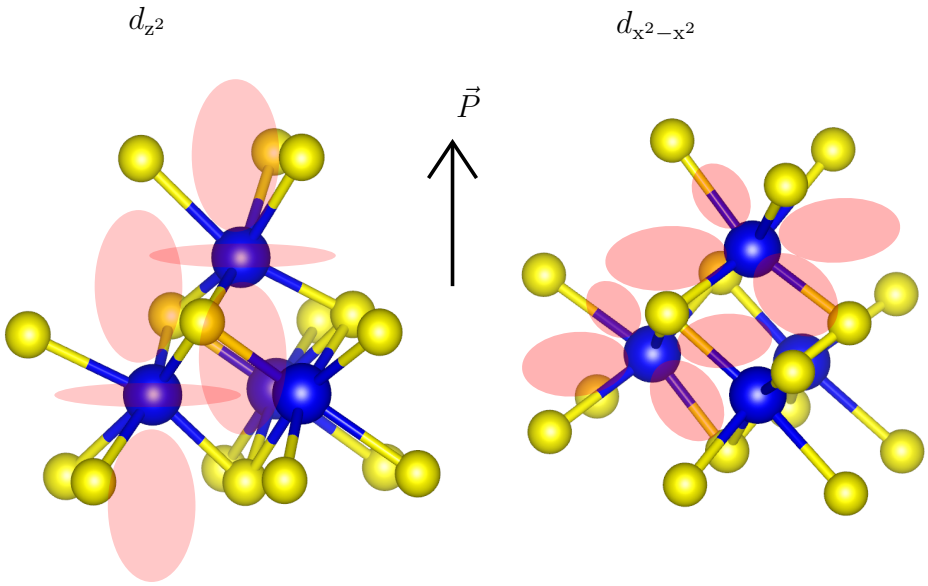

Figure 7.22: Schematic depiction of d orbitals used for the reconstruction of the spin distribution. It is assumed that the d_{z^2} and $d_{x^2-y^2}$ orbitals have the least energy in this near octahedral crystal field environment.

In order to obtain an optimal cluster wavefunction based on d orbitals, the superposition of the individual wavefunctions is calculated. With the resulting electron density $\Psi^*_{\mathrm{tot}}\Psi_{\mathrm{tot}}$, the internal field originating from the dipole field of the distribution can be calculated, and then compared with the experiment, as discussed in subsection 7.2.3. By minimizing the fit deviation parameter χ^2 with respect to the experimental resonance fields, an optimal cluster orbital is generated for a given set of parameters and assumptions. For a cluster orbital constructed from d_{z^2} orbitals, the only parameters that determine the NMR hyperfine fields are the prefactors of the wavefunctions, the effective nuclear charge Z, and the Fermi contact field as a pseudo parameter. In principle, when optimizing the cluster orbital, the contact field can be implemented as a free parameter, however due to the anisotropic part of the hyperfine field, it is determined to have the same value for all valid cluster orbital solutions. This is due to the isotropic contact field shifting the resonance towards higher fields, while leaving the anisotropic part of the hyperfine coupling unchanged. In the experiment, at the minimum of the resonance fields, the nucleus is experiencing a dipole field of $\frac{2}{3}\Delta H_{\mathrm{res}} \approx 1.8\,\mathrm{T}$ parallel to the external field. The contact term, providing a negative isotropic hyperfine shift, competes with this dipole field in a way, to shift the resonance close to the diamagnetic ^{51}V position. A small positive shift of 0.1 T at $\vec{H} \parallel [111]$ remains, which means that the contact term must account for $H_{\mathrm{contact}} = -1.8\,\mathrm{T} + 0.1\,\mathrm{T} = -1.7\,\mathrm{T}$. The optimal value for all simulations turned out to be $H_{\mathrm{contact}} = -1.693\,\mathrm{T}$, which is in close agreement with the just derived value of $H_{\mathrm{contact}} = -1.7\,\mathrm{T}$. This agreement further strengthens the assumption, that the

electron dipole fields are the sole source of the anisotropic fields. The isotropic shift is rather large and negative, which can be explained by the core polarization effect, caused by d electrons. Electrons of the $3d$ shell polarize the closed s shells negatively, so the s electron spin polarization points in the opposite direction as for the d electron [104, 105]. This effect can be strong, accounting for up to 12.5 T [104–106] via the contact interaction. A smaller occupancy (due to sharing the electron with the other V sites) and therefore a reduced spin density at the nucleus can reduce the isotropic shift down to the observed value of −1.693 T. From Pocha et al. [72], it is suggested that the molecular orbital structure is an even distribution of d_{z^2} orbitals on each vanadium site. The wavefunction prefactors are therefore equal for all sites with $c^U_{z^2} = c^\alpha_{z^2} = \frac{1}{2}$, which means that the only parameter that needs to be optimized in this simple case is the effective nuclear charge Z, which expands or contracts the $3d$ orbital upon decreasing or increasing, respectively. In order to determine the optimal Z value, an optimization algorithm is applied to the program simulating the curves, described in section 7.2.3. The optimal Z values are then returned and the cluster wavefunction can be determined. The best fit was reached for an effective nuclear charge of $Z = 9.42$, which is a plausible value, considering the negatively charged ligands and non-perfect shielding of the nucleus [107, 108]. For the first row of transition metals, the effective nuclear charge can be estimated as follows [108]:

$$Z_{\text{eff}}(A) = Z(A)(0.385 + 0.025(m - 2)) \tag{7.37}$$

For Vanadium, $Z(A = V) = 23$ and $m = 2$, and therefore $Z_{\text{eff}}(V) = 10.58$. The isosurface representation of the spin distribution and the resulting resonance field curves are shown in Fig. 7.23. The out-of-plane anisotropy of the hyperfine coupling is reproduced very well, however, the in-plane anisotropy is reversed in comparison with the experiment. This is the result of the axial symmetry of the d_{z^2} orbital. For an isolated ion, when only the d_{z^2} orbital is occupied, the field rotation around the z axis would lead to a constant resonance field, independent of the rotation angle. Therefore, the simulated in-plane anisotropy originates from the transferred fields from the other V sites. For correctly reproducing the NMR measurement, a superposition of d_{z^2} orbitals alone is insufficient. Therefore, the cluster wavefunction is expanded via additional d_{xy} or $d_{x^2-y^2}$ orbitals, effectively removing the axial symmetry of the electron distribution at each site. Due to the shape of these additional orbitals, when superposing them with the d_{z^2} orbital, the d_{z^2} electron density in the xy plane (ring shape in the base plane with the wavefunction having a negative sign) will be stretched towards a symmetry axis of the superposed orbitals. This is illustrated in Fig. 7.24, where a sketch of d_{z^2} orbitals are shown, superposed with d_{xy} or $d_{x^2-y^2}$ orbitals with either positive or negative signs. The red area depicts the in-plane electron distribution, which is stretched along the symmetry axis of the lobes with negative sign. The shown superpositions of the wavefunctions must suffice the mirror-plane symmetry that is dictated by the site symmetry of the A, B and C sites. This condition discards the d_{xy} orbitals, as they violate the mirror plane symmetry

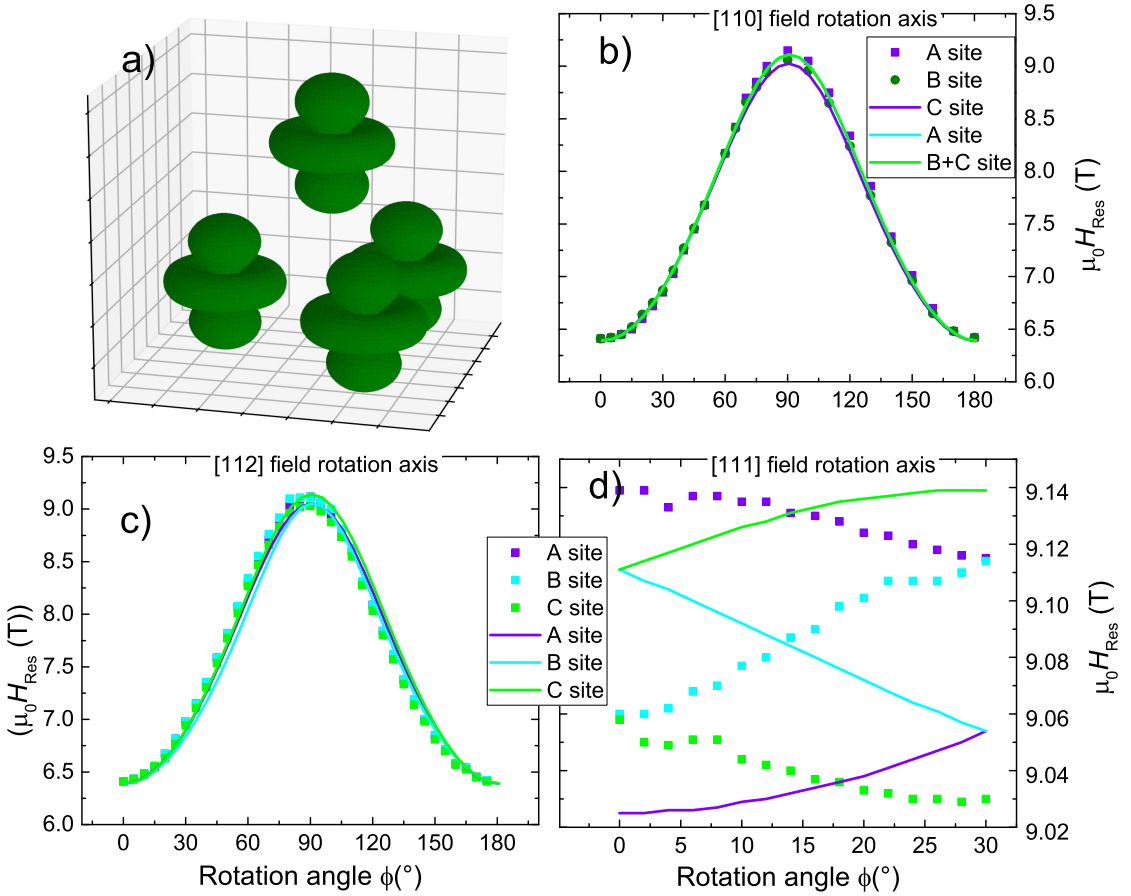

Figure 7.23: a) Isosurface representation of the spin density distribution, encasing 90% of the probability distribution. d_{z^2} orbitals were placed with equal weight on each V site. b)-d) Measured (scatter) and simulated (solid lines) resonance fields for a [110], [112] and [111] field rotation axis. The spin distribution is based on the best fit solution ($Z = 9.42$) with d_{z^2} orbitals.

indicated by the vertical mirror plane in Fig. 7.24. Nevertheless, whether one of these configuration would be able to reconstruct the NMR measurements will be checked as well. To construct the cluster orbital, each wavefunction centered around the A, B or C site is rotated by 120° about the z axis with respect to the neighbouring wavefunction, which preserves the threefold symmetry of the cluster orbital. At first, orbitals are only placed at the basal ^{51}V sites, leaving the U site unoccupied. The d orbitals are transformed from one site to next in the following way:

$$c_{z^2}\Psi^{A}_{z^2}(r,\theta) = c_{z^2}\Psi^{B}_{z^2}(r - r_B, \theta) = c_{z^2}\Psi^{C}_{z^2}(r - r_C, \theta) \tag{7.38}$$

$$c_{xy}\Psi^{A}_{xy}(r,\theta,\phi) = c_{xy}\Psi^{B}_{xy}(r - r_B, \theta, \phi + 2\pi/3) = c_{xy}\Psi^{C}_{xy}(r - r_C, \theta, \phi - 2\pi/3) \tag{7.39}$$

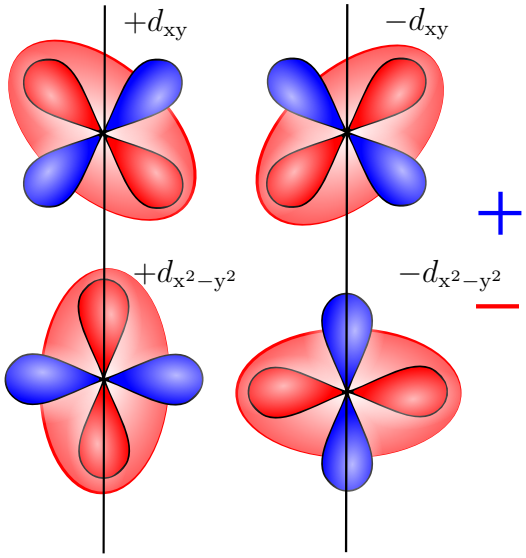

Figure 7.24: Schematic depiction of the in-plane spin density of the d_{z^2} orbital after superposition with different orbitals. The negative sign of the d_{z^2} wavefunction and the orientation of the lobes of the other orbitals determine the axis of elongation.

Analogously, $d_{x^2-y^2}$ orbitals transform identically to d_{xy} orbitals. The cluster wavefunction is then given by one of the following,

$$\Psi_{\text{tot}} = \sum_{\alpha=A,B,C} c_{z^2}\Psi^{\alpha}_{z^2}(r,\theta) + c_{xy}\Psi^{\alpha}_{xy}(r,\theta,\phi) \tag{7.40}$$

$$\Psi_{\text{tot}} = \sum_{\alpha=A,B,C} c_{z^2}\Psi^{\alpha}_{z^2}(r,\theta) + c_{x^2-y^2}\Psi^{\alpha}_{x^2-y^2}(r,\theta,\phi), \tag{7.41}$$

depending on whether d_{xy} or $d_{x^2-y^2}$ orbitals contribute in addition to d_{z^2}. In Fig. 7.24, real prefactors were used, but in general these can be complex. Since only relative signs/phases of the superposed wavefunctions are relevant and the absolute phase has no influence on the electron distribution, the unnormalized prefactor of the d_{z^2} orbital is set to 1. The prefactors $c_{x^2-y^2}$ and c_{xy} can have any phase, which can influence the actual charge and spin distribution. Real prefactors (no phase difference with c_{z^2}) allow a cancellation of certain regions of the d_{z^2} orbital, which stretches the in-plane charge distribution in certain directions, as depicted in Fig. 7.24. Pure imaginary prefactors (phase difference of $\phi = 90°$ with c_{z^2}) cannot lead to cancellations, as the magnitude of the resulting complex number is always finite when determining the spin density $|\Psi|^2$. Imaginary prefactors therefore prohibit a stretching of the in-plane charge distribution, which is not optimal, as a such a distribution is needed to compete with the transferred dipole fields from the other ^{51}V sites. This effect is shown in Fig. 7.25, where $c_{z^2} = 0.516$ and $|c_{x^2-y^2}| = 0.258$.

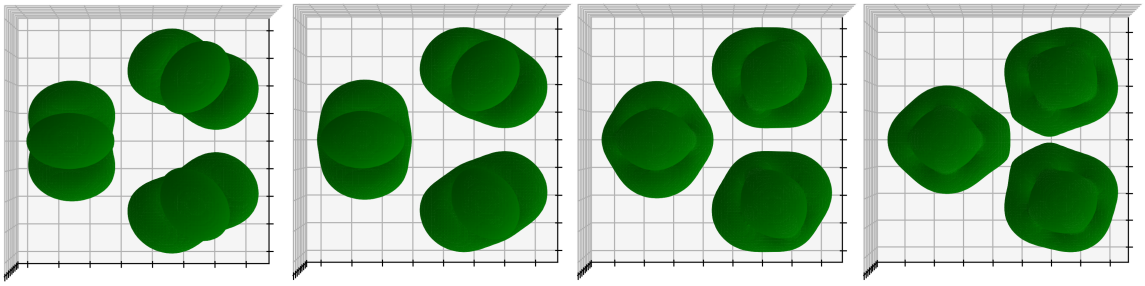

$\phi = 0°$ $\phi = 30°$ $\phi = 60°$ $\phi = 90°$

Figure 7.25: Influence of the phase of $c_{x^2-y^2}$ on the charge distribution. Due to the d_{z^2} being real, imaginary prefactors of the superposed $d_{x^2-y^2}$ change the in-plane charge distribution from lobe-like to circle-like. The prefactors are $c_{z^2} = 0.516$ and $c_{x^2-y^2} = 0.258\exp(i\phi)$.

Table 7.1: Phase dependence of the orbital prefactors

ϕ (°)	c_{z^2}	$c_{x^2-y^2}\exp(-i\phi)$	Z
0	0.575	-0.0493	8.597
30	0.574	-0.0570	8.602
60	0.569	-0.0984	8.640
90	0.577	0	8.587

Similarly to the simulations in Fig. 7.23, an optimization process is performed, which finds the best fitting configuration of Z and $|c_{x^2-y^2}|$ for different phases of $c_{x^2-y^2}$. Properly reproducing the NMR data was not possible with a purely imaginary prefactor, as the minimal χ^2 was reached for $|c_{x^2-y^2}| = 0$. For prefactors with finite real parts, an agreement with the NMR data was possible, as seen for the example of a purely real prefactor in Fig. 7.26. Larger imaginary parts require a higher magnitude of $c_{x^2-y^2}$, due to the real part of the superposed wavefunction staying constant in order to keep the stretching of the in-plane electron distribution unchanged. In table 7.1, the phase dependent prefactors are shown, which were obtained via the aforementioned optimization process.

In the following, only real prefactors are considered, which provides a lower limit for the magnitude of the prefactor of the secondary orbital $d_{x^2-y^2}$. For d_{xy} orbitals, the best agreement is reached for a vanishing prefactor $c_{xy} = 0$, hence the contributions originating from d_{xy} orbitals are neglected. The configuration, able to reproduce the NMR data, is the superposition of d_{z^2} and $d_{x^2-y^2}$ orbitals with real prefactors (as shown in one example in Fig. 7.26).

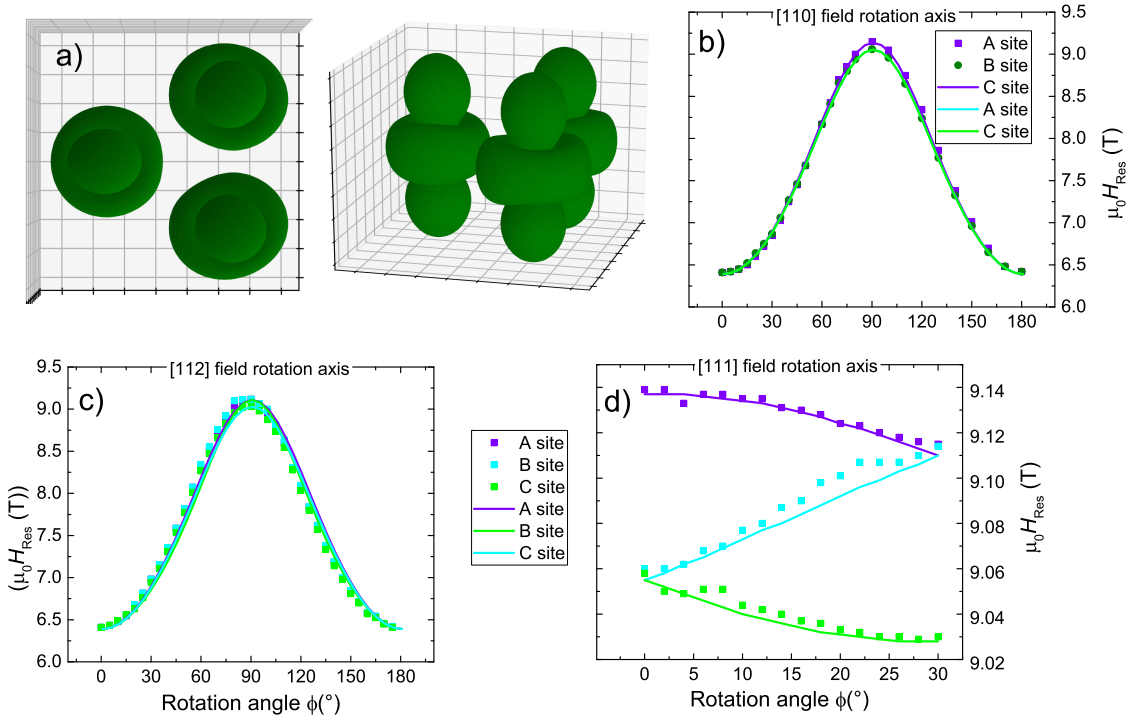

Figure 7.26: a) Isosurface representation of the spin density distribution, utilizing a superposition of d_{z^2} and $d_{x^2-y^2}$ orbitals on the A,B and C site. It encases 95% of the probability distribution. b)-d) Measured (scatter) and simulated (solid lines) resonance fields based on the best fit solution ($c_{z^2} = 0.5752$, $c_{x^2-y^2} = -0.0439$, $Z = 8.597$).

The population of the U site has been neglected so far, because the local spin distribution around the base A,B and C sites is the most important for reproducing the NMR data. Dipole fields from the U site would only have minor influences, as shown in the first panel of Fig. 7.21 due to the large distance between the NMR nuclei at the base from the U site. However, an increasing occupancy of the U site influences the spin distribution at the base, due to the fact that in total one electron is shared among the four sites. When populating the U site, the threefold symmetry of the electron distribution needs to be preserved, thus only the d_{z^2} orbital can be occupied at the U site, hence the cluster wavefunction is then given by:

$$\Psi_{\text{tot}} = c^{\text{U}}_{z^2}\Psi^{\text{U}}_{z^2}(r,\theta) + \sum_{\alpha=A,B,C} c_{z^2}\Psi^{\alpha}_{z^2}(r,\theta) + c_{x^2-y^2}\Psi^{\alpha}_{x^2-y^2}(r,\theta,\phi) \tag{7.42}$$

The occupancy Ω of the U site is then calculated as follows:

$$\Omega = \frac{(c^{\text{U}}_{z^2})^2}{(c^{\text{U}}_{z^2})^2 + \sum_{\alpha=A,B,C}(c_{z^2})^2 + (c_{x^2-y^2})^2} \tag{7.43}$$

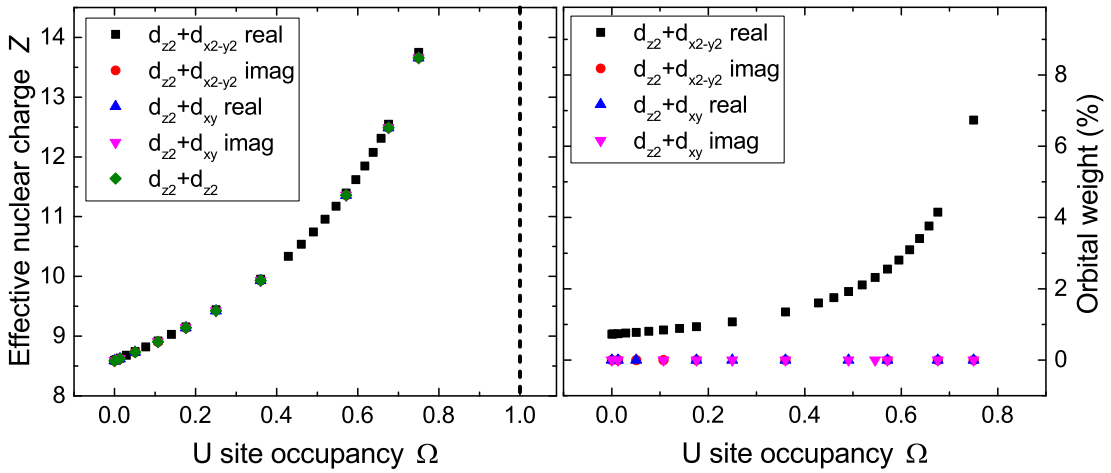

Figure 7.27: Dependence of the effective nuclear charge Z (left) and the orbital weight $|c_{x^2-y^2}|^2/(|c_{z^2}|^2 + |c_{x^2-y^2}|^2)$ (right) on the occupancy Ω of the U site. Each configuration containing nonzero orbital weights for the secondary orbital correctly reproduces the NMR data similar to Fig. 7.26.

For different U site occupancies Ω, the orbital parameters are determined via fitting the NMR data, which is shown in Fig. 7.27. There is a clear correlation between the Z value and $c_{x^2-y^2}$ on the U site occupancy. As the U site is more populated, the base sites lose electron density, which needs to be compensated via an increase in the effective nuclear charge Z. The same is true for the weight of the $d_{x^2-y^2}$ orbitals, which need to compensate a change in the transferred dipole field coming from the U site. In the limit of a 100% occupation of the U site, the Z value approaches infinity, as an electron at the U site does not reproduce the NMR data.

In this section, the cluster orbital was constructed using atomic d_{z^2} and $d_{x^2-y^2}$ orbitals. Calculating the hyperfine fields based on orbital configurations and optimizing the occupancies and orbital parameters yields a set of possible cluster orbitals which are consistent with the NMR data.
Using the NMR data alone does not provide a unique solution for the spin distribution, but rather a one dimensional solution space, where the occupancy of the U site, or equivalently, the effective nuclear charge determines the spin distribution over the cluster. In order to find a unique solution, additional insights other than the NMR data need to be included, which can discriminate between the different solutions provided by the NMR analysis.

7.2.6 Occupation of the Unique U Site

Since any partial occupation of the U site is compatible with the NMR data, simulating the hyperfine fields and optimizing the cluster orbitals does not provide a unique solution for the distribution of the single d electron over the V_4S_4 cluster. A direct measurement of the U site occupancy has not been provided yet, however Dally et al. [109] suggested an even distribution over the cluster based on SANS measurements. From the NMR measurements, the only evidence on the U site occupancy could be the signal from the U site itself, which is not observed. However, the signal not being observed hints towards either larger hyperfine fields or faster T_2 relaxation rates at the U site ^{51}V nucleus. A higher relaxation rate can originate from a stronger coupling between the electron and the nucleus due to the fluctuations of electron spins opening a relaxation channel for the nucleus. Both scenarios, a higher internal field or relaxation rate, require a higher occupancy than those of the base sites since they are observed, which indicates values of $\Omega > 25\%$. With an effective nuclear charge $Z = 10.58$ from Eq. 7.37 [108], an occupancy of $\Omega \approx 46\%$ of the U site would be most plausible, but since the used formula does not necessarily apply for clusters, neither does it consider ligand fields, it should rather be considered as a rough estimate. From Müller et al. [103], a larger occupancy of $\Omega = 69.6\%$ is proposed, based on spin-polarized LDA+U calculations.
Importantly, the observed hyperfine field caused by the contact interaction can be used as a discriminator for the different Ω values. From Carter et al. [104], the hyperfine fields due to the core polarization from a single electron in different orbitals is listed in table 7.2. The observed contact field of 1.7 T in GaV_4S_8 can therefore be attributed to a fraction of a single electron. The electron fraction per base atom is determined by the ratio of the observed and tabulated contact interaction, resulting in $1.7\,\mathrm{T}/12.5\,\mathrm{T} = 13.6\% = (1-\Omega)/3$ and an U site occupancy $\Omega = 59.2\%$.

The negative sign for the hyperfine fields of $3d$ electrons implies that the s shell polarization is opposite to the $3d$ spin polarization. Therefore, using the two obtained values $\Omega = 69,9\%$ and $\Omega = 59,2\%$, the conclusion is hereby made, that the U site is populated by about $\Omega = (64 \pm 6)\%$ of the single d electron in the V_4S_4 cluster. The spin distribution associated with this U site population, which reproduces the NMR hyperfine fields is depicted in top panels of Fig. 7.28. With additional quantum chemical calculations using an embedded $[V_4S_{16}]^{-19}$ cluster model, performed by Thorben Petersen [110], the distribution of the single electron was calculated as well, which is in good agreement with the shown approach of superposing d orbitals to agree with the NMR results. The depiction of this distribution is shown in the bottom panels of Fig. 7.28. The orbital parameters for the solution corresponding to $\Omega = 64\%$ are given by:

$$Z = 12.06 \quad c^{\alpha}_{x^2-y^2} = -0.064 \quad c^{\alpha}_{z^2} = 0.341 \quad c^{U}_{z^2} = 0.799 \tag{7.44}$$

Table 7.2: Contact Hyperfine fields due to core polarization for a single unpaired electron in different orbitals, adopted from [104]

Orbital	Core polarization hyperfine field (T)
2p	+3
3p	+1.5
4p	-5
5p	-15
6p	-30
3d	-12.5
4d	-35

In conclusion, the spin density of the single d electron is found to be largest at the U site, with a about $\Omega = (64 \pm 6)\%$, while the rest of the spin density is localized at the three bottom sites of the V_4 sites. This conclusion was drawn due to the NMR analysis as well as the determination of the isotropic NMR shift induced by the spin polarization of s electrons via the Fermi contact interaction.

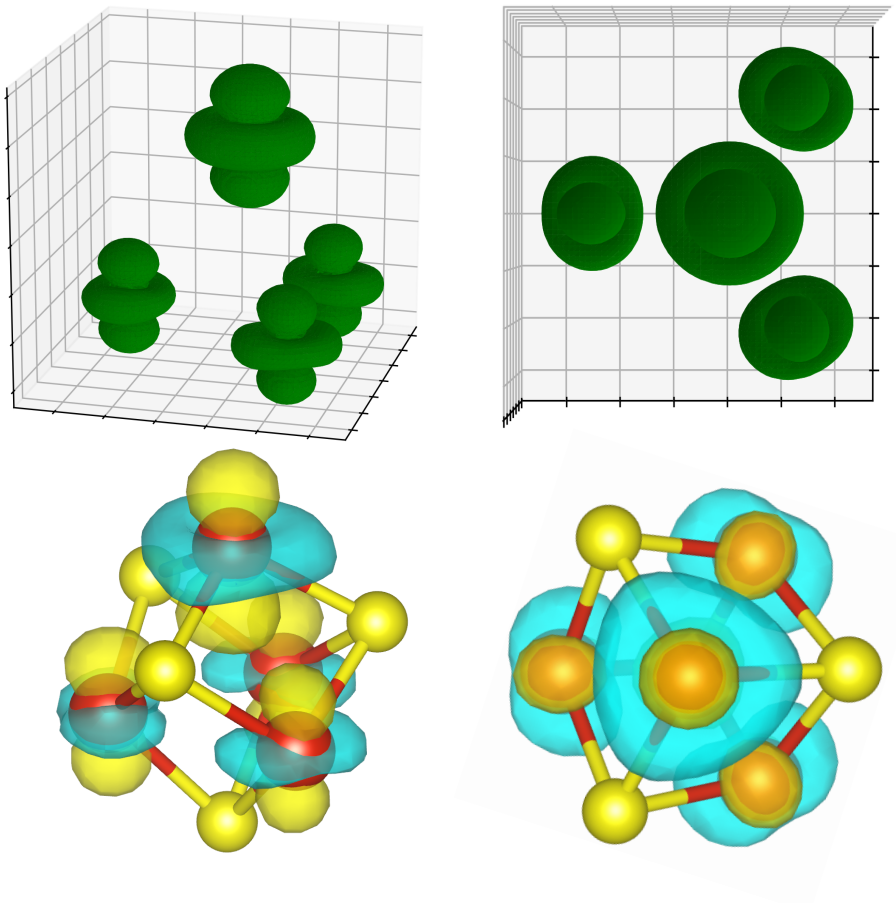

Figure 7.28: Top: Isosurface representations of the spin distribution over the cluster for $\Omega = 64\%$ using superpositions d_{z^2} and $d_{x^2-y^2}$ orbitals. The orbital parameters are chosen to match the NMR hyperfine shifts. 90% of the electronic distribution is contained within the surfaces.
Bottom: Isosurface representation of the spin distribution obtained by quantum chemical calculations by Thorben Petersen [110].

Chapter 8

Conclusion

In conclusion, the electronic properties of the lacunar spinels GaV_4Se_8 and GaV_4S_8 are investigated via a deep and extensive NMR study presented in this work. The ^{71}Ga nuclei in both compounds are local probes for the structural distortion, or equivalently the ferroelectric polarization, driven by the Jahn-Teller transition. Interaction between the electric field gradient (EFG) and the ^{71}Ga nucleus and its nuclear quadrupoole moment Q leads to a splitting of the ^{71}Ga NMR lines. This allowed us to determine the quadrupolar frequency ν_Q whose temperature dependence closely follows the ferroelectric polarization. By this, we demonstrated that the quadrupolar frequency ν_Q is a local measure of the ferroelectric order parameter and accurately reproduces the polarizations on a local scale.

The quadrupole splitting in ^{71}Ga spectra in finite magnetic fields depends on the orientation of the magnetic field with respect to the principle axis of the EFG tensor. Since Ga occupies a unique site in the unit cell, its site symmetry is identical with the point group symmetry of the crystal. Therefore, in the polar rhombohedral state, the EFG tensor at the ^{71}Ga nuclei has an axial symmetry, which offers a simple approach to determine the volume fraction of the four types of polar domains. Different methods for measuring domain populations using ^{71}Ga spectra were developed and proved to be consistent with each other, as well as with methods utilizing ^{51}V spectra. The magnetic Vanadium ion sites embedded in a $V_4S(e)_4$ cluster show strong magnetic anisotropy in their NMR spectra. Similarly to the domain dependent ^{71}Ga spectra, rotation experiments show the different domains as distinct NMR lines in the ^{51}V spectra, which can also be used for domain quantification. There, spectra are recorded for each domain under the same conditions within a field rotation, in order to provide a consistent result. This technique was then used to investigate the domain population under electric and magnetic poling, showing the validity of the developed method. NMR can be used to quantify domain population in a large variety of systems, however the exact technique may differ greatly [111–114].

The V_4S_4 cluster is distorted below T_{JT}, which gives rise to two inequivalent V sites, located on the apical site of the elongated V_4 tetrahedron (U site) and its base

triangle (A, B and C site). In order to analyse the complex structure of the ^{51}V spectra, the quadrupolar interaction was investigated via a 180° magnetic field rotation around the [110]. We found, that the NMR signal originates from the three base sites, while the unique U site was not observed. Two different branches emerged, since the base sites become inequivalent upon a [110] field rotation axis, with respect to their quadrupolar interaction. The local EFG was reconstructed from measurements of the quadrupolar interaction causing oscillations in the T_2 decay measurements, and showed good agreement with ab initio DFT calculations [90] with small deviations to be corrected for via hyperfine fields.
In order to investigate the hyperfine coupling in more detail, additional rotation experiments were performed, rotating the magnetic field around the [112] and [111] axes. The basal plane, which is a $\langle 111 \rangle$-type plane, shows very small anisotropy of the hyperfine field, whereas the rotation planes containing the polar [111] axis demonstrate a strong anisotropy of ΔH_{Res} =2.7 T. With the experimentally determined hyperfine fields, the hyperfine coupling matrix was deduced, which corrected the previous deviations between the ab inito calculated and measured EFG, as the total field $\vec{H}_{\mathrm{int}} + \vec{H}_{\mathrm{ext}}$ is relevant for the quadrupolar interaction.
Going even further, the spin distribution over the cluster was reconstructed based on the anisotropy of the hyperfine coupling. The hyperfine coupling originates from the dipole field of the spin density distribution over the V_4S_4 cluster and the contact interaction, while the orbital magnetization was neglected. The spin distribution is modeled via superposition of atomic d orbitals, consisting of d_{z^2} and $d_{x^2-y^2}$ orbitals. The overall cluster orbital obeys a threefold symmetry, implemented via a 120° rotation about the polar z axis from one base site to the next. The U site is populated by a pure d_{z^2} orbital since other orbitals would not fulfill the threefold symmetry. Regarding the calculation of the hyperfine fields based on a given spin distribution, any U site occupancy is able to reproduce the NMR data, however the spin distribution at the base needs to compensate for the smaller weights by a closer distance to the nucleus, increasing the effective nuclear charge Z. This one dimensional solution space was further narrowed down by theoretical work [103, 110] as well as the strength of the Fermi contact interaction [104], which hints towards a population of (64 ± 6) % of the U site.
This thesis therefore provides experimental evidence for the orbital structure in the V_4S_4 cluster, which was not available in this detail before. Based on NMR data it was possible to refine the spin distribution and the orbital occupancy of the V_4S_4 cluster ions, which is an original and new result. The result itself is specific to GaV_4S_8, however the used approach can be applied to other anisotropic cluster magnets with one or few d electrons. Therefore, this work presents a pathway for better understanding and modeling multiferroic materials, and subsequent emergent phenomena with potential for future applications.

Bibliography

[1] James Clerk Maxwell. *A treatise on electricity and magnetism*, volume 1. Clarendon press, 1873.

[2] K. Takahashi, N. Kida, and M. Tonouchi. Terahertz radiation by an ultrafast spontaneous polarization modulation of multiferroic $BiFeO_3$ thin films. *Physical Review Letters*, 96(11):117402, 2006.

[3] T. Kubacka, J. A. Johnson, M. C. Hoffmann, C. Vicario, S. De Jong, P. Beaud, S. Grübel, S.-W. Huang, L. Huber, L. Patthey, et al. Large-amplitude spin dynamics driven by a THz pulse in resonance with an electromagnon. *Science*, 343(6177):1333–1336, 2014.

[4] A. Pimenov, A. A. Mukhin, V. Y. Ivanov, V. D. Travkin, A. M. Balbashov, and A. Loidl. Possible evidence for electromagnons in multiferroic manganites. *Nature Physics*, 2(2):97–100, 2006.

[5] R. Palai, R. S. Katiyar, H. Schmid, P. Tissot, S. J. Clark, J. Robertson, S. Redfern, G. A. Catalan, and J. F. Scott. β phase and γ- β metal-insulator transition in multiferroic $BiFeO_3$. *Physical Review B*, 77(1):014110, 2008.

[6] K. Singh, H. M. Jang, S. Ryu, and M. H. Jo. Polarized Raman Scattering of Multiferroic Epitaxial Films with Rhombohedral R3c Symmetry. *Appl. Phys. Lett*, 88(4):042907.

[7] J. Wang, J. B. Neaton, H. Zheng, V. Nagarajan, S. B. Ogale, B. Liu, D. Viehland, V. Vaithyanathan, D. G. Schlom, U. V. Waghmare, et al. Epitaxial $BiFeO_3$ multiferroic thin film heterostructures. *science*, 299(5613):1719–1722, 2003.

[8] Jan Seidel, Lane W Martin, Q He, Q Zhan, Y-H Chu, A Rother, ME Hawkridge, P Maksymovych, P Yu, M Gajek, et al. Conduction at domain walls in oxide multiferroics. *Nat. Mater.*, 8(3):229–234, 2009.

[9] Nicola A Spaldin and Rammamoorthy Ramesh. Advances in magnetoelectric multiferroics. *Nature materials*, 18(3):203–212, 2019.

[10] L. C. Chapon, G. R. Blake, M. J. Gutmann, S. Park, N. Hur, P. G. Radaelli, and S. W. Cheong. Structural Anomalies and Multiferroic Behavior in Magnetically Frustrated $TbMn_2O_5$. *Physical Review Letters*, 93(17):177402, 2004.

[11] A. Singh, V. Pandey, R. K. Kotnala, and D. Pandey. Direct evidence for multiferroic magnetoelectric coupling in $0.9BiFeO_3$–$0.1\ BaTiO_3$. *Physical Review Letters*, 101(24):247602, 2008.

[12] E. M. Purcell, H. C. Torrey, and R. V. Pound. Resonance absorption by nuclear magnetic moments in a solid. *Physical Review*, 69(1-2):37, 1946.

[13] Felix Bloch. Nuclear induction. *Physical Review*, 70(7-8):460–474, 1946.

[14] Milan Wayne Garrett. Thick cylindrical coil systems for strong magnetic fields with field or gradient homogeneities of the 6th to 20th order. *Journal of Applied Physics*, 38(6):2563–2586, 1967.

[15] Paul C Lauterbur. Image formation by induced local interactions: examples employing nuclear magnetic resonance. *Nature*, 242(5394):190–191, 1973.

[16] C. P. Slichter. *Principles of magnetic resonance*. Springer-Verlag New York Heidelberg Berlin, 1978.

[17] A. Abragam. *Principles of nuclear magnetism*. Oxford University Press, 1982.

[18] V. I. Chizhik and Y. S. Chernyshev. *Magnetic resonance and its applications*. Springer International Publishing Switzerland, 2014.

[19] Erwin L Hahn. Spin echoes. *Physical Review*, 80(4):580, 1950.

[20] T. Dey, M. Majumder, J. C. Orain, A. Senyshyn, M. Prinz-Zwick, S. Bachus, Y. Tokiwa, F. Bert, P. Khuntia, N. Büttgen, et al. Persistent low-temperature spin dynamics in the mixed-valence iridate $Ba_3InIr_2O_9$. *Physical Review B*, 96(17):174411, 2017.

[21] M. Majumder, M. Prinz-Zwick, S. Reschke, A. Zubtsovskii, T. Dey, F. Freund, N. Büttgen, A. Jesche, I. Kézsmárki, A. A. Tsirlin, et al. Field evolution of low-energy excitations in the hyperhoneycomb magnet β-Li_2IrO_3. *Physical Review B*, 101(21):214417, 2020.

[22] D. Halliday, R. Resnick, J. Walker, and S. M. Koch. *Halliday Physik–Bachelor Edition*. Weinheim: Wiley, 2007.

[23] G.H. Stauss. Nuclear Magnetic Resonance of Cd in $CdCr_2Se_4$ and $CdCr_2S_4$, and Transferred Spin Polarization in Chromium Chalcogenide Spinels. *Physical Review*, 181(2):636, 1969.

[24] P. Heller and G. B. Benedek. Nuclear Magnetic Resonance in MnF_2 near Critical Point. *Physical Review Letters*, 8(11):428, 1962.

[25] Y. A. Sakhratov, M. Prinz-Zwick, D. Wilson, N. Büttgen, A. Y. Shapiro, L. E. Svistov, and A. P. Reyes. Magnetic structure of the triangular antiferromagnet $RbFe(MoO_4)_2$ weakly doped with nonmagnetic K+ ions studied by NMR. *Physical Review B*, 99(2):024419, 2019.

[26] N. Büttgen, W. Krätschmer, L. E. Svistov, L. A. Prozorova, and A. Prokofiev. NMR study of the high-field magnetic phase of $LiCuVO_4$. *Physical Review B*, 81(5):052403, 2010.

[27] A. A. Gippius, A. V. Tkachev, S. V. Zhurenko, A. V. Mahajan, N. Büttgen, M. Schädler, I. O. Chernyavskii, I. V. Morozov, S. Aswartham, B. Büchner, et al. NMR study of magnetic structure and hyperfine interactions in the binary helimagnet FeP. *Physical Review B*, 102(21):214416, 2020.

[28] J. M. Baker, E. R. Davies, and J. P. Hurrell. Electron nuclear double resonance in calcium fluoride containing Yb^{3+} and Ce^{3+} in tetragonal sites. *Proceedings of the Royal Society of London. Series A. Mathematical and Physical Sciences*, 308(1494):403–431, 1969.

[29] Rafael Calvo. A general spin hamiltonian to describe ligand hyperfine structure. its application to heme-proteins. i. nuclear zeeman and hyperfine interactions. *Journal of Magnetic Resonance (1969)*, 26(3):445–459, 1977.

[30] L. C. Stubbs. Hyperfine interaction tensor calculations in molecular systems. *PhD Thesis*, 1978.

[31] W. C. Lin and C. A. McDowell. Electron spin resonance of an x-ray irradiated single crystal of α-glycylglycine. *Molecular Physics*, 4(4):333–342, 1961.

[32] W. Demtröder. *Experimentalphysik 3 Atome, Moleküle und Festkörper 4. Auflage*. Springer-Verlag Berlin Heidelberg New York, 2010.

[33] D. H. Martin. *Magnetism in Solids*. The MIT Press, 1967.

[34] E. Pavarini, E. Koch, F. Anders, and M. Jarrell. Correlated electrons: from models to materials. *Reihe Modeling and Simulation*, 2, 2012.

[35] G. M. Volkoff, H. E. Petch, and D. W. L. Smellie. Nuclear electric quadrupole interaction in single crystals. *Canadian Journal of Physics*, 30(3):270–289, 1952.

[36] R. V. Pound. Nuclear electric quadrupole interactions in crystals. *Physical Review*, 79(4):685, 1950.

[37] H. Abe, H. Yasuoka, and A. Hirai. Spin echo modulation caused by the quadrupole interaction and multiple spin echoes. *Journal of the Physical Society of Japan*, 21(1):77–89, 1966.

[38] R. Brener and E. Ehrenfreund. Quadrupole interaction measurements in some $CsBX_3$ (B= Ni, Mg; X= Cl, Br) crystals by spin-echo modulation. *Journal of Magnetic Resonance*, 26(3):539–541, 1977.

[39] B. B. Van Aken, J.-P. Rivera, H. Schmid, and M. Fiebig. Observation of ferrotoroidic domains. *Nature*, 449(7163):702–705, 2007.

[40] Nicola A. Hill. Why are there so few magnetic ferroelectrics? *The journal of Physical Chemistry B*, 104(29):6694–6709, 2000.

[41] Daniel Khomskii. Classifying multiferroics: Mechanisms and effects. *Physics*, 2:20, 2009.

[42] T. Lottermoser and D. Meier. A short history of multiferroics. *Physical Sciences Reviews*, 6(2), 2021.

[43] R. Seshadri and N. A. Hill. Visualizing the role of Bi 6s "lone pairs" in the off-center distortion in ferromagnetic $BiMnO_3$. *Chemistry of Materials*, 13(9):2892–2899, 2001.

[44] T. Atou, H. Chiba, K. Ohoyama, Y. Yamaguchi, and Y. Syono. Structure determination of ferromagnetic perovskite $BiMnO_3$. *Journal of Solid State Chemistry*, 145(2):639–642, 1999.

[45] B. B. Van Aken, T. Palstra, A. Filippetti, and N. A. Spaldin. The origin of ferroelectricity in magnetoelectric $YMnO_3$. *Nature Materials*, 3(3):164–170, 2004.

[46] J. Van Den Brink and D. I. Khomskii. Multiferroicity due to charge ordering. *Journal of Physics: Condensed Matter*, 20(43):434217, 2008.

[47] M. Alexe, M. Ziese, D. Hesse, P. Esquinazi, K. Yamauchi, T. Fukushima, S. Picozzi, and U. Gösele. Ferroelectric switching in multiferroic magnetite (Fe_3O_4) thin films. *Advanced Materials*, 21(44):4452–4455, 2009.

[48] M. S. Senn, J. P. Wright, and J. P. Attfield. Charge order and three-site distortions in the verwey structure of magnetite. *Nature*, 481(7380):173–176, 2012.

[49] J. de Groot, T. Mueller, R. A. Rosenberg, D. J. Keavney, Z. Islam, J.-W. Kim, and M. Angst. Charge order in $LuFe_2O_4$: an unlikely route to ferroelectricity. *Physical Review Letters*, 108(18):187601, 2012.

[50] Y. Tokura, S. Seki, and N. Nagaosa. Multiferroics of spin origin. *Reports on Progress in Physics*, 77(7):076501, 2014.

[51] L. C. Chapon, P. G. Radaelli, A. G. R. Blake, S. Park, and S.-W. Cheong. Ferroelectricity induced by acentric spin-density waves in YMn_2O_5. *Physical Review Letters*, 96(9):097601, 2006.

[52] Y. Tokunaga, S. Iguchi, T.-H. Arima, and Y. Tokura. Magnetic-field-induced ferroelectric state in $DyFeO_3$. *Physical Review Letters*, 101(9):097205, 2008.

[53] Yusuke Tokunaga, Nobuo Furukawa, Hideaki Sakai, Yasujiro Taguchi, Takahisa Arima, and Yoshinori Tokura. Composite domain walls in a multiferroic perovskite ferrite. *Nature Materials*, 8(7):558–562, July 2009.

[54] I. E. Dzyaloshinskii. Theory of helicoidal structures in antiferromagnets .1. nonmetals. *Soviet Physics Jetp-ussr*, 19(4):960–971, 1964.

[55] Tôru Moriya. Anisotropic superexchange interaction and weak ferromagnetism. *Physical Review*, 120(1):91, 1960.

[56] F. Schrettle, S. Krohns, P. Lunkenheimer, J. Hemberger, N. Büttgen, H.-A. Krug Von Nidda, A. V. Prokofiev, and A. Loidl. Switching the ferroelectric polarization in the S= 1/ 2 chain cuprate $LiCuVO_4$ by external magnetic fields. *Physical Review B*, 77(14):144101, 2008.

[57] G. Lawes, M. Kenzelmann, N. Rogado, K. H. Kim, G. A. Jorge, R. J. Cava, A. Aharony, O. Entin-Wohlman, A. B. Harris, T. Yildirim, et al. Competing magnetic phases on a kagomé staircase. *Physical Review Letters*, 93(24):247201, 2004.

[58] Y. Yamasaki, S. Miyasaka, Y. Kaneko, J.-P. He, T. Arima, and Y. Tokura. Magnetic reversal of the ferroelectric polarization in a multiferroic spinel oxide. *Physical Review Letters*, 96(20):207204, 2006.

[59] T Kimura, T Goto, H Shintani, K Ishizaka, T-h Arima, and Y Tokura. Magnetic control of ferroelectric polarization. *nature*, 426(6962):55–58, 2003.

[60] H. T. Yi, Y. J. Choi, S. Lee, and S.-W. Cheong. Multiferroicity in the square-lattice antiferromagnet of $Ba_2CoGe_2O_7$. *Applied Physics Letters*, 92(21):212904, 2008.

[61] H. Murakawa, Y. Onose, S. Miyahara, N. Furukawa, and Y. Tokura. Comprehensive study of the ferroelectricity induced by the spin-dependent d-p hybridization mechanism in $Ba_2XGe_2O_7$ (X= Mn, Co, and Cu). *Physical Review B*, 85(17):174106, 2012.

[62] S. Seki, Y. Onose, and Y. Tokura. Spin-driven ferroelectricity in triangular lattice antiferromagnets $ACrO_2$ (A=Cu,Ag,Li,or Na). *Physical Review Letters*, 101(6):067204, 2008.

[63] M. Kenzelmann, G. Lawes, A. B. Harris, G. Gasparovic, C. Broholm, A. P. Ramirez, G. A. Jorge, M. Jaime, S. Park, Q. Huang, et al. Direct transition from a disordered to a multiferroic phase on a triangular lattice. *Physical Review Letters*, 98(26):267205, 2007.

[64] Vinod Wadhawan. *Introduction to ferroic materials*. CRC press, 2000.

[65] Pierre Weiss. La variation du ferromagnétisme avec la température. *Comptes Rendus*, 143:1136–1139, 1906.

[66] C. Kittel. *Einführung in die Festkörperphysik*. Oxford University Press, 1982.

[67] Wilma Eerenstein, ND Mathur, and James F Scott. Multiferroic and magnetoelectric materials. *nature*, 442(7104):759–765, 2006.

[68] KF Wang, J-M Liu, and ZF Ren. Multiferroicity: the coupling between magnetic and polarization orders. *Advances in Physics*, 58(4):321–448, 2009.

[69] A. Butykai, S. Bordacs, I. Kezsmarki, V. Tsurkan, A. Loidl, J. Doring, E. Neuber, P. Milde, S. C. Kehr, and L. M. Eng. Characteristics of ferroelectric-ferroelastic domains in Neel-type skyrmion host GaV_4S_8. *Scientific Reports*, 7:44663, March 2017.

[70] S. Widmann, E. Ruff, A. Günther, H.-A. Krug von Nidda, P. Lunkenheimer, V. Tsurkan, S. Bordács, I. Kézsmárki, and A. Loidl. On the multiferroic skyrmion-host GaV_4S_8. *Philosophical Magazine*, 97(36):3428–3445, 2017.

[71] I. Kezsmarki, S. Bordacs, P. Milde, E. Neuber, L. M. Eng, J. S. White, H. M. Ronnow, C. D. Dewhurst, M. Mochizuki, K. Yanai, H. Nakamura, D. Ehlers, V. Tsurkan, and A. Loidl. Neel-type skyrmion lattice with confined orientation in the polar magnetic semiconductor GaV_4S_8. *Nature Materials*, 14(11):1116–+, November 2015.

[72] R. Pocha, D. Johrendt, and R. Pottgen. Electronic and structural instabilities in GaV_4S_8 and $GaMo_4S_8$. *Chemistry of Materials*, 12(10):2882–2887, October 2000.

[73] H.-M. Zhang, J. Chen, P. Barone, K. Yamauchi, S. Dong, and S. Picozzi. Possible emergence of a skyrmion phase in ferroelectric $GaMo_4S_8$. *Physical Review B*, 99(21):214427, 2019.

[74] K. Geirhos, S. Krohns, H. Nakamura, T. Waki, Y. Tabata, I. Kézsmárki, and P. Lunkenheimer. Orbital-order driven ferroelectricity and dipolar relaxation dynamics in multiferroic gam o 4 s 8. *Physical Review B*, 98(22):224306, 2018.

[75] S. Jakob, H. Müller, D. Johrendt, S. Altmannshofer, W. Scherer, S. Rayaprol, and R. Pöttgen. Structural and magnetic transitions in the mott insulator ganb 4 s 8. *Journal of Materials Chemistry*, 17(36):3833–3838, 2007.

[76] T Waki, Y Kajinami, Y Tabata, H Nakamura, M Yoshida, M Takigawa, and I Watanabe. Spin-singlet state formation in the cluster Mott insulator $GaNb_4S_8$ studied by μ SR and NMR spectroscopy. *Physical Review B*, 81(2):020401, 2010.

[77] K. Geirhos, J. Langmann, L. Prodan, A. A. Tsirlin, A. Missiul, G. Eickerling, A. Jesche, V. Tsurkan, P. Lunkenheimer, W. Scherer, et al. Cooperative cluster jahn-teller effect as a possible route to antiferroelectricity. *Physical Review Letters*, 126(18):187601, 2021.

[78] R. Pocha, D. Johrendt, B. Ni, and M. M. Abd-Elmeguid. Crystal structures, electronic properties, and pressure-induced superconductivity of the tetrahedral cluster compounds $GaNb_4S_8$, $GaNb_4Se_8$, and $GaTa_4Se_8$. *Journal of the American Chemical Society*, 127(24):8732–8740, 2005.

[79] M. M. Abd-Elmeguid, B. Ni, D. I. Khomskii, R. Pocha, D. Johrendt, X. Wang, and K. Syassen. Transition from Mott Insulator to Superconductor in $GaNb_4Se_8$ and $GaTa_4Se8$ under High Pressure. *Physical Review Letters*, 93(12):126403, 2004.

[80] Lilian Prodan[1], Vladimir Tsurkan[1,2], Korbinian Geirhos[1], Maximilian Winkler[1], and Somnath Ghara[1]. Private communication. [1] *Experimental Physics V, Center for Electronic Correlations and Magnetism, University of Augsburg,* [2]*Institute of Applied Physics, Chisinau, Republic of Moldova*, 2021.

[81] K. Geirhos, S. Reschke, S. Ghara, S. Krohns, P. Lunkenheimer, and I. Kézsmárki. Optical, dielectric, and magnetoelectric properties of ferroelectric and antiferroelectric lacunar spinels. *Physica Status Solidi (B)*, page 2100160, 2021.

[82] S. Mühlbauer, B. Binz, F. Jonietz, C. Pfleiderer, A. Rosch, A. Neubauer, R. Georgii, and P. Böni. Skyrmion lattice in a chiral magnet. *Science*, 323(5916):915–919, 2009.

[83] Y. Fujima, N. Abe, Y. Tokunaga, and T. Arima. Thermodynamically stable skyrmion lattice at low temperatures in a bulk crystal of lacunar spinel GaV_4Se_8. *Physical Review B*, 95(18):180410(R), May 2017.

[84] S. Bordacs, A. Butykai, B. G. Szigeti, J. S. White, R. Cubitt, A. O. Leonov, S. Widmann, D. Ehlers, H. A. K. von Nidda, V. Tsurkan, A. Loidl, and I. Kezsmarki. Equilibrium skyrmion lattice ground state in a polar easy-plane magnet. *Scientific Reports*, 7:7584, August 2017.

[85] N. Nagaosa and Y. Tokura. Topological properties and dynamics of magnetic skyrmions. *Nature nanotechnology*, 8(12):899–911, 2013.

[86] E. Ruff, S. Widmann, P. Lunkenheimer, V. Tsurkan, S. Bordács, I. Kézsmárki, and A. Loidl. Multiferroicity and skyrmions carrying electric polarization in gav4s8. *Science advances*, 1(10):e1500916, 2015.

[87] Lilian Prodan[1], Dana Vieweg[1], Franz Mayr[1], and Vladimir Tsurkan[1,2]. Private communication. [1] *Experimental Physics V, Center for Electronic Correlations and Magnetism, University of Augsburg,* [2]*Institute of Applied Physics, Chisinau, Republic of Moldova*, 2021.

[88] E. Ruff, A. Butykai, K. Geirhos, S. Widmann, V. Tsurkan, E. Stefanet, I. Kezsmarki, A. Loidl, and P. Lunkenheimer. Polar and magnetic order in GaV_4Se_8. *Physical Review B*, 96(16):165119, October 2017.

[89] M. Prinz-Zwick, B. G. Szigeti, T. Gimpel, D. Ehlers, V. Tsurkan, A. O. Leonov, B. Miksch, M. Scheffler, I. Stasinopoulos, D. Grundler, et al. Nuclear and electron spin resonance studies on skyrmion-hosting lacunar spinels. *Physica Status Solidi (B)*, page 2100170, 2021.

[90] Pavel Marton[1,2] and Jirka Hlinka[1]. Private communication. [1]*Institute of Physics, Czech Academy of Sciences, Prague, Czech Republic,* [2]*Institute of Mechatronics and Computer Engineering, Technical University of Liberec, Czech Republic.*

[91] Pascal P Man. Quadrupole couplings in nuclear magnetic resonance, general. *Encyclopedia of analytical chemistry*, 10:9780470027318, 2000.

[92] J. Liu, X. Feng, and D. Wang. Determination of water content in crude oil emulsion by LF-NMR CPMG sequence. *Petroleum Science and Technology*, 37(10):1123–1135, 2019.

[93] R. Zhang, J. Huo, Z. Peng, Q. Feng, J. Wang, and J. Zhang. Research on oil-based drilling fluids emulsion droplet by low-field nmr. *Applied Magnetic Resonance*, 47(12):1339–1352, 2016.

[94] M. Prinz-Zwick, T. Gimpel, K. Geirhos, S. Ghara, C. Steinbrecht, V. Tsurkan, N. Büttgen, and I. Kézsmárki. Probing multiferroic order parameters and domain population via nuclear spins. *Physical Review B*, 105(1):014301, 2022.

[95] S. Ghara, K. Geirhos, L. Kuerten, P. Lunkenheimer, V. Tsurkan, M. Fiebig, and I. Kézsmárki. Giant conductivity of mobile non-oxide domain walls. *Nature Communications*, 12(1):1–8, 2021.

[96] K. Geirhos. Polar and magnetoelectric properties of lacunar spinels. *PhD Thesis*, 2021.

[97] B. G. Szigeti, M. Hemmida, H.-A. Krug von Nidda, D. Ehlers, L. Prodan, V. Tsurkan, H. Nakamura, F. Simon, L. Forró, and I. Kézsmárki. On the competition of magnetocrystalline and g-tensor anisotropy in lacunar spinels GaV_4Se_8 and $GaMo_4S_8$. *in preparation*, 2022.

[98] M. Prinz-Zwick, T. Gimpel, P. Marton, T. Petersen, V. Tsurkan, N. Büttgen, L. Hozoi, J. Hlinka, and I. Kézsmárki. Locating a d-electron in a magnetic cluster via nuclear probes. *in preparation*, 2022.

[99] R. M. Achey, P. L. Kuhns, A. P. Reyes, W. G. Moulton, and N. S. Dalal. ^{13}C NMR evidence for Fermi-contact interaction and spin delocalization on the ligands in the nanomagnet $Mn_{12}O_{12}$-acetate. *Solid State Communications*, 121(2-3):107–109, 2002.

[100] D. Ehlers, I. Stasinopoulos, I. Kézsmárki, T. Fehér, V. Tsurkan, H.-A. Krug von Nidda, D. Grundler, and A. Loidl. Exchange anisotropy in the skyrmion host GaV_4S_8. *Journal of Physics: Condensed Matter*, 29(6):065803, December 2016.

[101] H. Nakamura, H. Chudo, and M. Shiga. Structural transition of the tetrahedral metal cluster: nuclear magnetic resonance study of GaV_4S_8. *Journal of Physics-condensed Matter*, 17(38):6015–6024, September 2005.

[102] H. Nakamura, H. Chudo, M. Shiga, and T. Kohara. Split and compensated hyperfine fields in magnetic metal clusters. *Hyperfine Interactions*, 159(1-4):71–74, 2004.

[103] H. Müller, W. Kockelmann, and D. Johrendt. The magnetic structure and electronic ground states of Mott insulators GeV_4S_8 and GaV_4S_8. *Chemistry of Materials*, 18(8):2174–2180, 2006.

[104] G. C. Carter, L. H. Bennett, and D. J. Kahan. Metallic shifts in nmr. a review of the theory and comprehensive critical data compilation of metallic materials. part iv. 1977.

[105] L. H. Bennett, R. E. Watson, and G. C. Carter. Relevance of knight shift measurements to the electronic density of states. *Journal of Research of the National Bureau of Standards. Section A, Physics and Chemistry*, 74(4):569, 1970.

[106] R. E. Watson and A. J. Freeman. Hyperfine interactions. *Academic Press, New York, 1967) p*, 53, 1967.

[107] R. Y. Babkin, K. V. Lamonova, S. M. Orel, and Y. G. Pashkevich. Determination of the effective nuclear charge for free ions of transition metals from experimental spectra. *Optics and Spectroscopy*, 107(1):9–15, 2009.

[108] S. Koseki, M. W. Schmidt, and M. S. Gordon. Effective nuclear charges for the first-through third-row transition metal elements in spin- orbit calculations. *The Journal of Physical Chemistry A*, 102(50):10430–10435, 1998.

[109] R. L. Dally, W. D. Ratcliff, L. Zhang, H.-S. Kim, M. Bleuel, J. W. Kim, K. Haule, D. Vanderbilt, S.-W. Cheong, J. W. Lynn, et al. Magnetic phase transitions and spin density distribution in the molecular multiferroic system GaV_4S_8. *Physical Review B*, 102(1):014410, 2020.

[110] Thorben Petersen and Liviu Hozoi. Private communication. *IFW Institute for theoretical solid state physics, Dresden, Germany.*

[111] A. V. Zalessky, A. A. Frolov, T. A. Khimich, A. A. Bush, V. S. Pokatilov, and A. K. Zvezdin. ^{57}Fe NMR study of spin-modulated magnetic structure in $BiFeO_3$. *Europhysics Letters (EPL)*, 50(4):547–551, May 2000.

[112] A. V. Zalessky, A. K. Zvezdin, I. S. Zheludev, A. M. Savvinov, and A. F. Lebedev. A New Type of Domain Wall NMR Spectrum in Canted Antiferromagnets: $YFeO_3$ and $LuFeO_3$ Crystals. *Physica Status Solidi (B)*, 73(1):317–325, 1976.

[113] D. F. Khozeev, A. V. Zalessky, A. A. Gippius, E. N. Morozova, and A. A. Bush. Spin modulation of ^{57}Fe NMR frequency and relaxation in $BiFeO_3$. *Physica B: Condensed Matter*, 329-333:848–849, May 2003.

[114] Y. A. Sakhratov, L. E. Svistov, P. L. Kuhns, H. D. Zhou, and A. P. Reyes. Magnetic structure and domain conversion of the quasi-2D frustrated antiferromagnet $CuCrO_2$ probed by NMR. *Journal of Experimental and Theoretical Physics*, 119(5):880–890, November 2014.

List of Publications

Publications related to this thesis:

1. M. Prinz-Zwick, T. Gimpel, K. Geirhos, S. Ghara, C. Steinbrecht, V. Tsurkan, N. Büttgen and I. Kézsmárki, Probing multiferroic order parameter and domain population via nuclear spins. *Physical Review B*, 105(1):014301, 2022

2. M. Prinz-Zwick, B.G. Szigeti, T. Gimpel, D. Ehlers, V. Tsurkan, A.O. Leonov, B. Miksch, M. Scheffler, I. Stasinopoulus, D. Grundler, I. Kézsmárki, N. Büttgen and H.-A. Krug von Nidda, Nuclear and electron spin resonance studies on skyrmion-hosting lacunar spinels, *Physical Status Solidi* (*B*), page 2100170, 2021

3. M. Prinz-Zwick, T. Gimpel, P. Marton, T. Petersen, V. Tsurkan, N. Büttgen, L. Hozoi, J. Hlinka and I. Kézsmárki, Locating a d-electron in a magnetic cluster via nuclear probes, *in preparation*

Other publications:

1. K. Somesh, Y. Furukawa, G. Simutis, F. Bert, M. Prinz-Zwick, N. Büttgen, A. Zorko, A.A. Tsirlin, P. Mendels and R. Nath, Universal fluctuating regime in triangular chromate antiferromagnets, *Physical Review B*, 104(10):104422, 2021

2. M.Majumder, M. Prinz-Zwick, S. Reschke, A. Zubtsovskii, T. Dey, F. Freund, N. Büttgen, A. Jesche, I. Kézsmárki, A.A. Tsirlin and P. Gegenwart, Field evolution of low-energy excitations in the hyperhoneycomb magnet beta-Li_2IrO_3, *Physical Review B*, 101(21):214417, 2020

3. M. Majumder, F. Freund, T. Dey, M. Prinz-Zwick, N. Büttgen, Y. Skourski, A. Jesche, A.A. Tsirlin and P. Gegenwart, Anisotropic temperature-field phase diagram of single crystalline beta-Li_2IrO_3: Magnetization, specific heat, and Li-7 NMR study, *Physical Review Materials* 3(7): 074408, 2019

4. S. Kundu, T. Dey, M. Prinz-Zwick, N. Büttgen and A.V. Mahajan, Structural and magnetic properties of a new cubic spinel $LiRhMnO_4$, *Journal of Magnetism and Magnetic Materials*, 481(77-84), 2019

5. R. Kumar, T. Dey, P.M. Ette, K. Ramesha, A. Chakraborty, I. Dasgupa, R. Eremina, S. Toth, A. Shahee, S. Kundu, M. Prinz-Zwick, A.A. Gippius, H.-A. Kurg von Nidda, N. Büttgen, P. Gegenwart and A.V. Mahajan, Structural, thermodynamic, and local probe investigations of the honeycomb material $Ag_3LiMn_2O_6$, *Physical Review B*, 99(14):144429, 2019

6. R. Kumar, T. Dey, P.M. Ette, K. Ramesha, A. Chakraborty, I. Dasgupa, J.C. Orain, C. Baines, S. Toth, A. Shahee, I.S. Kundu, M. Prinz-Zwick, A.A. Gippius, N. Büttgen, P. Gegenwart and A.V. Mahajan, Unconventional magnetism in the 4d(4)-based S=1 honeycomb system $Ag_3LiRu_2O_6$, *Physical Review B*, 99(5):054417, 2019

7. Y. A. Sakhratov, M. Prinz-Zwick, D. Wilson, N. Büttgen, Y. A. Shapiro, L. E. Svistov and A. P. Reyes, Magnetic structure of the triangular antiferromagnet $RbFe(MoO_4)(2)$ weakly doped with nonmagnetic K+ ions studied by NMR, *Physical Review B*, 99(2):024419, 2019

8. T. Dey, M. Majumder, J.C. Orain, A. Senyshyn, M. Prinz-Zwick, S. Bachus, Y. Tokiwa, F. Bert, P. Khuntia, N. Büttgen, A.A. Tsirlin and P. Gegenwart, Persistent low-temperature spin dynamics in the mixed-valence iridate $Ba_3InIr_2O_9$, *Physical Review B*, 96(17):174411, 2019

Acknowledgements

Here, I would like to thank all the people who were of great help for the completion of this thesis and the research and effort accompanied with it. Especially, my gratitude goes to

Prof. Dr. István Kézsmárki for welcoming me as his PhD student at Experimental Physics V, for being my supervisor and for all the fruitful discussions that accompanied my stay,

Prof. Dr. Sándor Bordács for agreeing to be my second assessor, even with the long travel accompanied with it,

Priv. Doz. Dr. Norbert Büttgen for supervising the NMR laboratory and my work in it and for the continous help on technical and scientific problems,

the Deutsche Forschungsgemeinschaft (DFG) and the Transregio TRR80 for funding the Project F4 and my PhD position,

all collaborators I had the honour of working with, such as Prof. Dr. Avinash Mahajan, Prof. Dr. Andrei Gippius, Dr. Mayukh Majumder, Dr. Tusharkanti Dey and Dr. Ramesh Nath,

Martina Schädler for introducing me into the NMR setup and laboratory, and for the friendship that evolved from working together,

Thomas Gimpel for the nice work environment in the laboratory during our joint effort on the GaV_4Se_8 NMR measurements,

the magnetic resonance group for fruitful discussions about nuclear or electron magnetic resonance and magnetism, and all other aspects of life. Special thanks goes to Bertalan Szigeti, Thomas Gimpel and Markus Preißinger for the frequent activities together,

All my colleagues at Experimental physics V for the amazing work environment. In particular, the frequent discussions on a variety of topics and the kindness of helping each other out in all sorts of problems, be it in the laboratory ot elsewhere. And special thanks to the colleagues in my office,

Dr. Korbinian Geirhos and Dr. Somnath Ghara for the help with the pyroelectric current measurements and poling experiments,

Birgitta Eisenschmid, Cheng Dung Lai and Anny Skroblies for always being a nice person to talk to and helpful with all sorts of formal and organizational issues,

and my friends and family for all the support, especially during hard times, when distraction was very helpful and needed. Especially i thank my brother Andreas for fruitful scientific discussions, as well as my parents Heinrich and Katharina for the tremendous support over the years